NTNU

Norwegian University of
Science and Technology

Exploring lithium ion batteries for wind powered water injection

Lars-Henrik Nysteen

Nanotechnology
Submission date: June 2016
Supervisor: Fride Vullum, IMTE
Co-supervisor: Are Kaspersen, DNV GL

Norwegian University of Science and Technology
Department of Materials Science and Engineering

Preface

All the experiments and analyses described in this work were carried out by the author at the Department of Materials Science and Engineering at NTNU, in collaboration with DNV GL during the spring of 2016.

The work is a continuation of the project thesis "Nanostructured Silica as an Anode for Li-ion Batteries" completed by the author in the fall of 2015, but with an emphasis full cell testing, and the possible application of the full cells in a practical application, namely a wind powered water injection system. The theory sections of Chapters 2.2, 2.3 and 2.4 are therefore similar, but include some modifications and additions.

First, I would like to thank my supervisor, Associate Professor Fride Vullum-Bruer for informative discussions, guidance and helpful input during the course of this work. In addition, I want to thank Postdoctoral Fellow Nils Wagner, for valuable suggestions on cathode fabrication and interpretation of the results. Further, I would like to thank my co-supervisor Are Kaspersen and the Win Win project team from DNV GL for sharing their ideas and specifications with a humble student. Hopefully, the results will be a contribution towards a safer, smarter and greener future.

Abstract

In this work, lithium ion batteries consisting of carbon-coated silica (SiO_2) anodes and various commercial cathodes were prepared, tested, and analysed for use in a novel wind-powered water injection system, designed by DNV GL. The carbon-coated anodes were fabricated using abundant, sea-hauled diatoms, a type of unicellular algae, as the SiO_2-containing precursor. The as-recieved diatoms were cleaned, wet-mixed with a carbon-containing precursor, before heat treatment in a flowing Ar atmosphere. The obtained carbon-coated SiO_2 active material was characterized using field-emission scanning electron microscopy, x-ray diffraction, thermogravimetric analysis, and nitrogen adsorption measurements.

Anode electrode sheets were fabricated by mixing the carbon-coated SiO_2 active material with an aqueous sodium alginate binder and carbon black conductive filler to form a homogeneous, viscous slurry, which was tape casted onto copper foil. The cathode electrode sheets were prepared in a similar fashion, but using commercial $LiMn_2O_4$, $Li(Ni_{1/3}Mn_{1/3}Co_{1/3})O_2$ and carbon-coated $LiFePO_4$ cathode active material, polyvinylidene fluoride binder and carbon black to form the slurry, and casted on aluminium foil.

The prepared anode and cathode electrodes were then assembled into coin cells with lithium counter electrodes and subjected to galvanostatic charge-discharge testing to evaluate the cycling stability and rate capability of the individual materials. High reversible specific capacities, above 460mA h g^{-1} at a current density of 50mA g^{-1}, and excellent rate capability was achieved for the carbon-coated SiO_2 anodes, attributed to improved electrical conductivity of the carbon coating, the high surface area and porosity of the diatom precursor and the formation of a stabilizing inert matrix of Li_2O and Li_4SiO_4. The commercial cathodes, with the exception of $LiFePO_4$, showed acceptable reversible capacities, and fair rate performance.

Next, the optimized anode material was used as an anode in a full lithium ion battery cell, investigated here for the first time. Poor initial Coulombic efficiency was identified as the largest performance-limiting factor of the assembled full cells. Several approaches to improve the reversible capacity were explored, including formation cycling, prelithiation of the SiO_2 anode, and decreasing the lower cell voltage cut-off potential. The full cells containing a prelithiated anode and discharged to low cell voltages showed the highest reversible capacity, but significant capacity fading due to possible anode material degradation following the deep discharge was observed. The rate performance of the full cells was found to be better or similar to that of the half cells, but the same capacity fading was noted.

The energy density of the cells fabricated in this work was found to be comparable to commercial cells containing lithium titanate ($Li_4Ti_5O_{12}$) anodes, even with the sub-optimal cathodes used. Based on the energy and power density achieved in the full cell testing for the SiO_2 anode, and the assumption that the anode shows stable cycling over thousands of cycles in combination with an optimized commercial $LiFePO_4$ cathode, the SiO_2-based batteries was found to be a potential candidate for use as an energy storage system in a wind-powered water injection system, showing a higher energy density than $Li_4Ti_5O_{12}$-based chemistries, as well as lower cost per cell.

Sammendrag

I dette arbeidet har litium-ion batterier bestående av en karbonkledd silica (SiO_2) anode og forskjellige kommersielle katoder blitt konstruert, testet og analysert for potensiell bruk i et vindkraftdrevet vanninjeksjonssystem, designet av DNV GL. Miljøvennlige kiselalger ble brukt som SiO_2-kilde til den karbonkledde anoden. Kiselalger er en type encellet alge som kan produseres ved havbruk. De mottatte kiselalgene ble vasket og våtblandet med et karbonholdig utgangsstoff, før de ble varmebehandlet i sirkulerende Ar-atmosfære. Det resulterende, karbonkledde, SiO_2-baserte aktive materialet ble karakterisert ved hjelp av feltemisjon-skanning-elektron-mikroskopi, røntgendiffraksjon, termogravimetrisk analyse og nitrogen-adsorpsjons-målinger.

Elektroder med anodemateriale ble konstruert ved å blande det SiO_2-baserte aktive materialet med et vannholdig natriumalginat-bindemiddel og elektrisk ledende karbon, hvilket resulterte i en homogen, viskøs slurry som ble deponert på kobberfolie. Katode-elektroder ble fabrikert på liknende vis, men det SiO_2-baserte aktive materialet og natriumalginat-bindemiddelet ble erstattet av henholdsvis $LiMn_2O_4$, $Li(Ni_{1/3}Mn_{1/3}Co_{1/3})O_2$, karbonkledd $LiFePO_4$, og et polyvinyliden-fluoridbindemiddel.

Halv-celle batterier med ren litium motelektrode og $SiO-2$-anode eller kommersiell katode ble konstruert, og utsatt for galvanostatisk opp- og utladning for å evaluere opp- og utladningsstabilitet og rate-egenskapene til de ulike materialene. Høy reversibel kapasitet, over 460mA h g^{-1} ved en strømtetthet på 50mA g^{-1}, samt gode rate-egenskaper ble observert for det karbonkledde SiO_2 aktive materialet. Den høye kapasiteten og gode rate-genskapene ble tilskrevet den økte elektriske ledningsevnen som resultat av karbonkledningen, det høye overflate-arealet og porositeten til kiselalge-utgangsstoffet, og utviklingen av en stabiliserende, inert matrix bestående av Li_2O og Li_4SiO_4. De kommersielle katodene, med unntak av $LiFePO_4$, viste akseptabel reversibel kapasitet og rate-egenskaper.

Det optimaliserte anodematerialet ble så brukt som anode i fullcelle litium-ion batterier, undersøkt for første gang i dette arbeidet. Lav Coulombisk effektivitet i først opp- og utladningssyklus ble raskt identifisert som den største begrensende faktoren i fullcellene. Ulike måter å forbedre den reversible kapasiteten ble undersøkt; én langsom formasjonssyklus, prelitiering av anoden og senking av cellespenningens nedre potensialgrense. Fullcellene med prelitiert anode, utladet til lave cellespenninger viste høyest kapasitet, men også gradvis synkende reversibel kapasitet, muligens grunnet degradering av anodematerialet ved lave cellespenninger. Rate-egenskapene til fullcellene var enten bedre eller omtrent lik som for halvcellene, og samme synkende kapasitetsutvikling ble observert.

Energitettheten til de fabrikerte fullcellene var sammenlignbar med kommersielle batterier basert på litium titanat-anoder ($Li_4Ti_5O_{12}$), selv med bruk av suboptimale katoder. Basert på energi- og effekt-tettheten oppnådd under fullcelletestingen og antagelsen at SiO_2/C-st80-8h-anodene kan gjennomgå flere tusen opp- og utladninger i kombinasjon med en optimalisert, kommersiell $LiFePO_4$ katode, kan SiO_2-baserte batterier være en kandidat til et energilagringssystem i det vindkraftdrevne vanninjeksjonssystemet. Dette ble begrunnet ut fra den høyere energitettheten til SiO_2/C-st80-8h sammenlignet med $Li_4Ti_5O_{12}$-baserte batterier, samt lavere kostnad per celle.

Contents

1 Introduction

Lithium ion batteries are currently the state of the art rechargeable battery system. The superior volumetric and gravimetric energy density, excellent cycling properties compared to competing technologies, and the ability to tailor performance characteristics has made the lithium ion battery system suitable for wide range of applications [1].

The market for Li-ion batteries is experiencing a rapid growth, driven by two important sectors. First, electric and plug-in hybrid electric vehicles rely heavily on lithium ion batteries, and are constituting a steadily increasing share of the automobile market. Consequently, the demand for high-performance batteries with improved performance will grow with their increasing market penetration. Second, it is widely recognized that renewable energy is the answer to mitigating the global climate changes, while simultaneously covering the electricity demand of a growing global population. As a consequence, wind and solar power are being deployed at unprecedented rates, with total installed capacity now above 178GW and 370GW, respectively [2]. However, since the energy output will fluctuate according to the availability of the resource, the need for intermediate energy storage is becoming increasingly pressing. The lithium ion battery system is a promising candidate to efficiently store excess energy, to be released in periods of high demand, both on small, medium and possibly large scales [3] [4].

In order to keep up with these future applications, new demands and restrictions must be met by the batteries. Electrodes and electrolytes that can fulfill criteria such as high power, minimal capacity loss and high safety, while maintaining good energy density and using environmentally benign materials, are highly sough-after [5]. It is widely recognized that the industry-standard graphite anodes will not be able to keep up with future demands, and that high-capacity anodes based on alloying, rather than intercalation with lithium will be the material of choice for the next generation of high-energy Li-ion batteries [6].

Silica (SiO_2) has recently emerged as a promising candidate to replace the industry-standard graphite anode. The material is classified as an alloy anode, and offers the advantage of high theoretical capacity, low cost and excellent cycling stability. Also, compared to other alloy materials, the volume expansion during lithiation and delithiation is comparatively small. Further, silica can be obtained from the outer shell of abundant sea-hauled diatoms, a type of eukaryotic, unicellular algae. In addition to being environmentally benign, the outer shell has a porous nanostructure, ideal for battery electrode applications [7]. The material is also compatible with water-based fabrication procedures, using high-performance sodium alginate binders. Water-based fabrication can significantly

reduce the cost of the produced batteries [8]. However, since the electronic conductivity of silica is low, it is usually nescessary to make use of a carbon coating to ensure sufficient electronic conductivity. This approach also have the added benefit of relieving the volume changes during cycling [9].

Aim of this work

The aim of this work was to fabricate high-capacity lithium ion batteries consisting of carbon-coated silica anodes and commercially available cathode materials, and evaluate the feasibility of their use as an energy store system in a novel wind powered water injection system. Abundant sea-hauled diatoms were used as the precursor for the anode. The diatoms were cleaned and coated with carbon by a heat treatment procedure with a carbon-containing precursor in an inert atmosphere. The surface structure and morphology, crystallinity, surface area and carbon content of the active material was characterized before half cells with lithium counter electrodes were constructed to investigate the electrochemical properties of the anode material.

The optimized anode material was used to construct full cells with several commercially available cathode materials. The full cells were then tested to evaluate the capacity, cycling stability and rate capability of the batteries. Different strategies for increasing the reversible capacity of the full cells was also explored.

2 Theory

The following chapter aims to give a brief introduction to the WIN WIN concept and the motivation for including a large-scale energy storage system, before the theory of lithium ion batteries is introduced. Silica based anodes will be discussed in detail in Chapter 2.4.

2.1 The WIN WIN concept

The oil industry is undergoing a time of transition, where low oil prices, aging assets and need to enhance oil revovery are driving the need for new, cost-effective energy solutions with a small carbon footprint to help mitigate the global climate crisis. Water injection is an important tool for enhanced oil recovery, often used to improve utilization of already developed fields and infrastructure. By matching the recent advances in floating wind turbine technology with the oil industry's need for water injection, DNV GL proposed a concept called WIN WIN, wind-powered water-injection. The concept consists of a floating wind turbine, which supplies power to a water injection process in fully standalone system, including pumps and basic water treatment. Led by DNV GL, the technical and economical feasibility of the WIN WIN concept was assessed in a joint industry project, in collaboration with ENI Norge, ExxonMobil, Nexen Petroleum, Statoil, VNG, ORE Catapult and PG Flow Solutions [10].

The WIN WIN concept was deemed technologically feasible. The key challenges adressed were reservoir and well tolerance to intermittent water injection, off-grid operation of the wind turbine and electrical system, and inclusion of basic water treatment. Based on input from the operators, a relevant use case was developed, and the WIN WIN was found to meet the required performance targets for injection rates and volumes over time, number of start-stop cycles and downtime duration. The system was designed to have a maximal injection rate capacity of 81 000 barrels (bbl) per day, and can deliver an average injection rate of 50 000bbl d^{-1}, surpassing the target rate of 44 000bbl d^{-1}. Further, avoided CO_2 emission per year has been estimated at 9000 tonnes [10].

2.1.1 Concept overview and operation

The WIN WIN concept consists of the following subsystems:

1. Wind turbine

2. Floating structure and mooring

3. Process system, located either topside or subsea

   Water inlet and pumps

   Water treatment system

   Injection pump

4. Electrical system

5. Control systems

6. Riser/umbilical and pipelines

All the process, electrical and control equipment is placed topside on a 17 x 17m^2 platform.

The main subsystem to consider when evaluating the feasibility of using lithium ion batteries as an intermediate energy storage system is the electrical subsystem. The main role of the electrical subsystem is to distribute the power generated by the wind turbine to the injection pumps and water treatment system, and handle the intermittency of the wind resource. This includes variations in injection rate, black starts, periods of no wind or strong wind, in addition to maintaining communication and safety systems when wind power is unavailable, and performing controlled start-ups and shut-downs of the total system.

Two different designs were suggested for the electrical system, a conventional micro-grid solution and a DC-link solution. The latter offers the advantage of a simpler electrical system, at the cost of modifying the wind turbine, as opposed to using a standard wind turbine. The voltage in both systems is stabilized by using a synchronous generator and a flywheel. In addition, both systems have included a battery-powered uninterruptable power supply (UPS) to keep critical systems in operation when wind power is unavailble. Further, a dump load is responsible for mitigating power fluctuations due to the wind speed variations, stabilizing the power input to the injection pumps. The layout of the electrical subsystem is shown in Figure 2.1, and Table 2.1 summarizes the most important parameters [10].

The WIN WIN concept has three operational phases:

1. Start-up: the system changes from shutdown to operative phase when wind speed reaches the operating range of the wind turbine.

2. Operative: the wind turbine generates power and the the system is injecting water. The voltage and frequency is continuously regulated.

3. Shutdown: the wind speed is above or below the operating range of the wind turbine. Power to the system is provided by the UPS.

Table 2.1: The parameters for the electrical subsystem shown in Figure 2.1 [10].

Component name	Options	Comments
Wind turbine	6MW direct drive	Standard option.
UPS	Battery bank of 1MW nominal power and 500kWh nominal capacity	The UPS cover the power demand in all operational phases for all main and auxiliary loads, including the motor to drive the flywheel, pitch and yaw drives, HVAC for the wind turbine nacelle and equipment room, as well as control, communication and instrumentation systems. System survives for 500 hours without wind.
Synchronous generator with flywheel	20MW	Regulates the voltage in the 6.6kV bus.
Dump load	3MW	Regulates power input fluctuations due to wind speed variations. The size of the dump load is limited by it's dimensions and weight.
Water injection pump capacity	2 x 2MW installed, max pump power required 2.4MW.	Installed pump capacity, the actual load requirement depends on required water injection pressure, which varies between reservoirs and may change over time. The target injection rate at a load of 2.4MW is 44 000bbl d^{-1}.
Chemical injection pump load	0.2kW	
Auxiliary system load	100kW	HVAC, lighting etc. under standard operating conditions

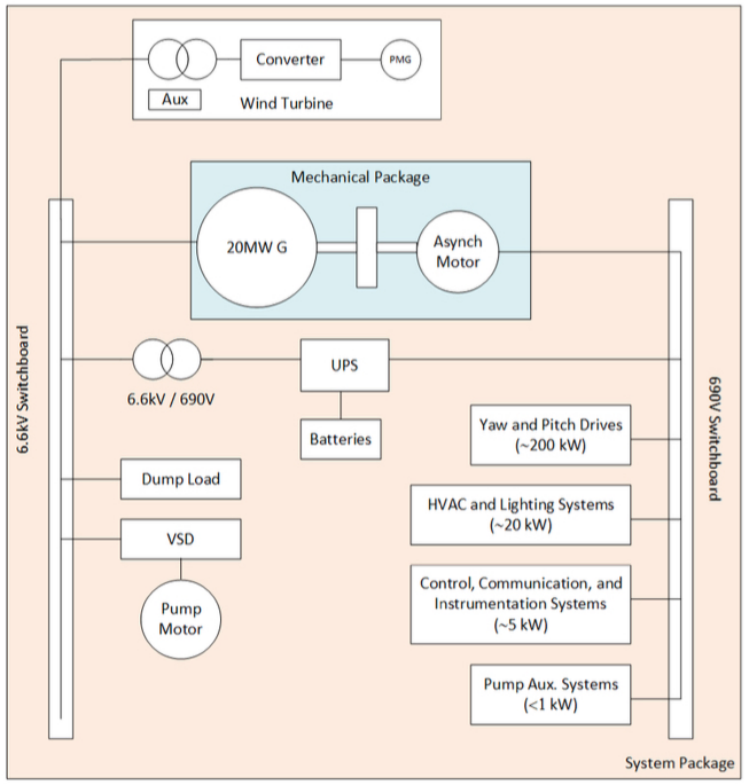

Figure 2.1: The electrical subsystem of the WIN WIN concept [10].

The wind resource is the largest influencing factor on the performance of the WIN WIN concept. By analysing a 13-year power series of wind data at the location of Utsira, 30km off the coast of south-western Norway, it was found that there are on average 180 production stops per annum, with an average duration of 8 hours. Water injection losses due to wind speeds outside of the working range of the wind turbine was found to be the largest loss term, making up more than 60% of the total injection losses.

2.1.2 Motivation for including large-scale energy storage

Although the proposed electrical system is expected to work robustly for the application, several improvements can be made if the synchronous generator and flywheel is replaced with a larger battery system, while keeping the overall electrical subsystem layout the same, as shown in Figure 2.2.

Compared to a synchronous generator and energizing flywheel, a battery system offers several advantages. First, a voltage and frequency reduction at the 6.6kV bus can be effectively countered using energy from batteries, rather than kinetic energy from the rotating mass of the flywheel. Second, the overall architecture of the electrical system is simplified, and the bulky and heavy mechanical package can be replaced with a more compact battery solution. Finally, reliability may be improved by substituting mechanical equipment with moving parts for an all solid-state system, and thereby avoiding the associated maintenance and downtime.

In addition, it is possible to increase the size of the battery system further to store excess energy to be used for water injection when wind power is unavailable. This approach is likely to result in improved system efficiency, as the injection losses due to wind variations will be comparatively smaller. Further, although the intermittent nature of wind energy was believed to have no negative effect on the water injection process and reservoir integrity, a system including large scale storage can potentially provide a steadier injection rate to the reservoir. This can offer the opportunity to deploy the system at less-than-ideal fields and wells. Additionally, a larger battery bank may be able to fully or partially replace the dump load used to regulate power input to the water injection pumps when the wind turbine is active, and during turbine cut-in and cut-out. In this way, energy that would otherwise be dissipated as heat could be harnessed and used productively, thus increasing overall system efficiency.

2.1.3 Requirements for the energy storage system

In this work, two use cases will be considered. The first use case involves replacing the synchronous generator and flywheel with a battery bank of equal nominal power, with enough capacity to operate critical equipment (Case 1), while the second will consider an expansion of battery capacity to store excess energy to be used for water injection during periods of wind power unavailability (Case 2).

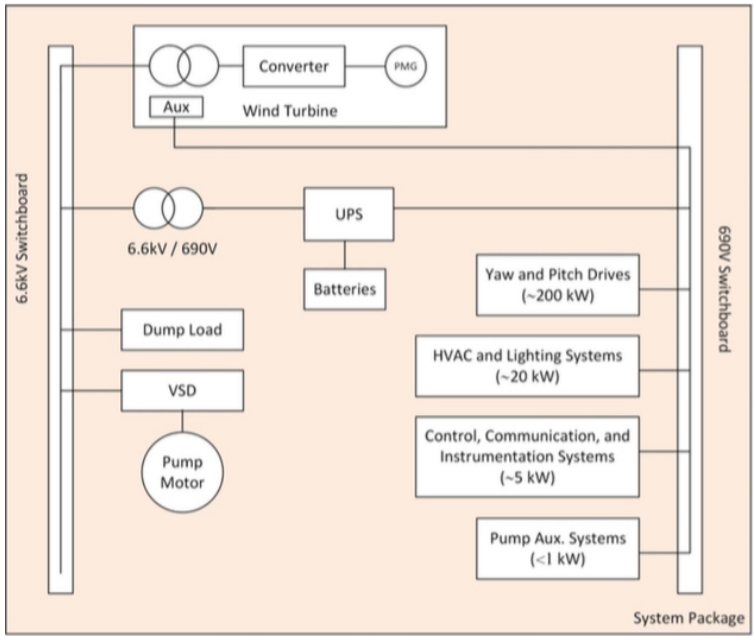

Figure 2.2: The electrical subsystem with the synchronous generator substituted for a larger battery system [10].

The requirements for both use cases are summarized in Table 2.2. First, both systems need a nominal power of 20MW to replace the synchronous generator and flywheel. Second, both systems should be possess a long cycle life, an estimated 3600 cycles for both use cases, before being considered unusable, so that replacement during the lifespan of the total system can avoided if possible. However, if the cost of the batteries is sufficiently low, this criterion may be relaxed. The nominal capacity in Case 1 is determined by the demand of the critical systems as described in Table 2.1. For Case 2, the nominal capacity should be high enough to power the same critical systems after providing a power of 2.4MW to the injection pumps for a minimum of 8 hours.

Table 2.2: Requirements for a potential energy storage system for the WIN WIN system. Case 1 - synchronous generator replaced by batteries. Case 2 - a larger energy storage system [10].

Condition	Case 1	Case 2
Operational lifetime	20 years	20 years
Production stops per annum	180	180
Average duration of stops	-	8 hours
Cycle life	3600 cycles	3600 cycles
Nominal power	20MW	20MW
Nominal capacity	0.5MWh	20MWh

2.2 The lithium ion battery

2.2.1 Working principle

The working principle of rechargeable, or secondary, lithium ion batteries is identical to other secondary battery systems. When the battery is discharged, the chemical energy stored in the active materials of the electrodes is converted through a reduction-oxidation (redox) reaction into electrical energy, resulting in a flow of electrons from the negative to the positive electrode through an external circuit. The battery can be recharged by applying external electric energy, which is stored as chemical energy in the active materials of the electrodes.

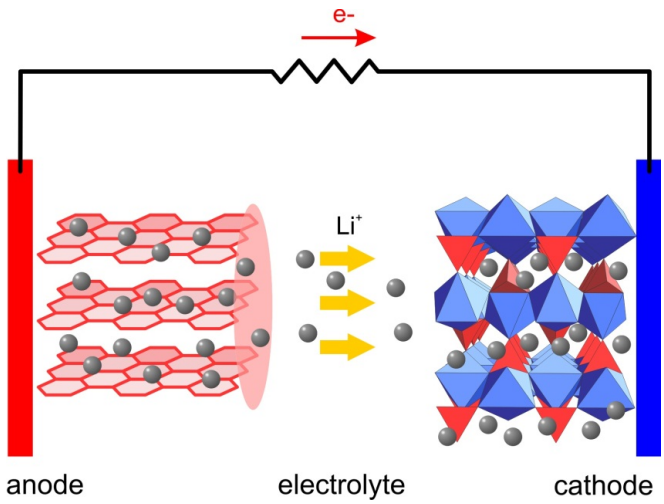

Figure 2.3: Schematic of a lithium ion battery during discharge. Electrons from the oxidation reaction at the graphite anode travel through an external circuit and are consumed by a reduction reaction at the transition metal oxide cathode [11].

The electrochemical cell consists of two electrodes, separated by an electrolyte, as shown in Figure 2.3. According to the standard definition, the electrode where the oxidation reaction takes place is defined as the anode, and the electrode hosting the reduction reaction is defined as the cathode. When the cell is discharged, the oxidation reaction on the anode (negative electrode) supplies electrons, which are transferred via an external circuit and consumed by the reduction reaction on the cathode (positive electrode). Consequently, the electrodes act as anode or cathode depending on whether the cell is being charged or discharged. A more useful designation is to take the cathode as the electrode with the highest potential with respect to the other, as shown in Figure 2.4. This potential difference between the two electrodes causes lithium ions to move spontaneously from the

anode to the cathode through the electrolyte when the battery is discharged.

The electrolyte enables internal charge transfer between the electrodes through high ionic and low electric conductivity, which prevents direct electron exchange and short circuiting of the cell. The charge balance is maintained by the flow of cations and anions in the electrolyte towards the oppositely charged electrodes during charge and discharge. Further, as an additional safety measure, most cells employ a polymeric separator, acting as a physical barrier to keep the electrodes from coming into direct contact.

The battery is charged by applying a voltage higher than the electrochemical potential between the electrodes. This results in a reversal of the electron, cation and anion flow.

For practical applications several individual cells are combined in series and parallel to achieve a desired voltage and capacity, respectively.

2.2.2 Electrode reactions

Today's lithium ion battery electrodes are based on intercalation compounds. These compounds are characterized by the ability to reversibly insert and deinsert Li^+-ions in a host structure. Intercalation compounds are usually layered structures, the most common materials being graphite on the anode side and lithium transition metal oxides on the cathode side. In most cases, the intercalation and deintercalation does not change the structure of the material significantly, but a slight volume change is usually involved.

The charge reaction for the anode and cathode proceeds according to Equation 2.1 and 2.2, respectively:

$$\mathrm{xLi^+ + yC + xe^- \longrightarrow Li_xC_y} \tag{2.1}$$

$$\mathrm{LiMO_2 \longrightarrow Li_{1-x}MO_2 + xLi + xe^-} \tag{2.2}$$

The total reaction is then:

$$\mathrm{LiMO_2 + yC \longrightarrow Li_{1-x}MO_2 + Li_xC_y} \tag{2.3}$$

where M denotes a transition metal, commonly Co, Mn or Ni [1]. The factor x varies from material to material, but due to structural restrictions it is usually limited to a number between 0.5 and 1. For every x Li^+-ions intercalated, y carbon atoms are needed. y has the smallest value of six for $x = 1$, i.e. LiC_6. By reversing the direction of Equations 2.1-2.3, the discharge reaction is obtained.

2.3 Lithium ion battery materials

2.3.1 Cathode materials

The cathode is the lithium source in lithium ion battery, and are commonly based on transition metal oxides. This is due to the fact that transition metal ions are

stable at multiple oxidation states, and through reduction of the transition metal ion valence, the extra charge from lithium intercalation can be accomodated and charge neutrality of the compound maintained. Further, to avoid severe structural changes or energetically disadvantageous effects, a crystal structure that is stable over large compositional ranges is paramount. This is a difficult criteria to fulfill, as irreversible phase transitions are likely to occur before all the lithium can be extracted [12]. Additionally, the discharge current of the cathode is determined by three processes: access to lithium ion in the electrolyte, lithium insertion into the compound, and the reduction of the transition metal ions by electrons from the anode. These processes are in turn dependent on the microstructure and morphology of the material, in addition to it's fundamental electrochemical properties [12].

Hence, the number of compounds suitable for use as a cathode in lithium ion batteries is limited, and the development of new cathode materials is major challenge. Only four main categories of materials have been succesfully used as commercial lithium ion battery cathodes: layered transition metal oxides, spinels, polyanionic compounds and composites thereof. A comparison of capacity and voltage for multiple cathode and anode materials are shown in Figure 2.4, and a comparison of cathode capacities is shown in Table 2.3.

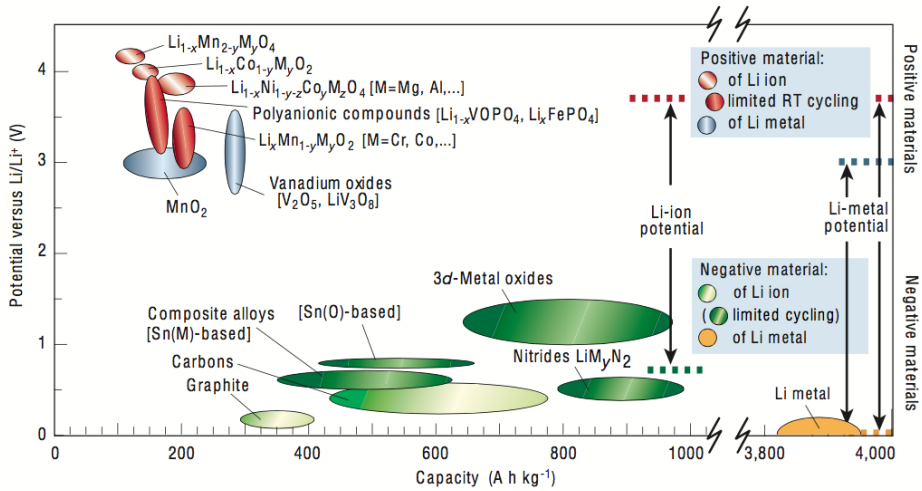

Figure 2.4: Voltage and capacity for various anode and cathode materials, both commercial and under research [1].

2.3.1.1 Layered transition metal oxides

The layered transition metal oxide $LiCoO_2$ (LCO), is one of the most commonly used cathode materials, especially for portable applications. $LiCoO_2$ has an α-

Table 2.3: Common commercial cathode materials and their practical specific capacities. Adapted from [12].

Material	Structure	Practical specific discharge capacity [mA h g^{-1}]
$LiCoO_2$	Layered transition metal oxide	100-160
$LiMn_2O_4$	Spinel	70-140
$LiFePO_4$	Polyanionic compound	80-155
$Li(Ni_{1/3}Mn_{1/3}Co_{1/3})O_2$	Composite	80-160

$NaFeO_2$ structure, which can be described as a cubic closed packed oxygen lattice with transition metal ions occupying the space between every other layer of anion sheets, which leaves Li^+-ions free to intercalate two-dimensionally into the essentially empty remaining layer [13][14]. This allows the use of high current densities, while giving negligible volume changes during cycling. In addition, the amount of lithium removed from the crystal can be voltage controlled due to the sloping potential profile. This is important as continuous lithium removal results in oxygen release and structural collapse, posing a safety concern [15]. The charge potential is usually limited to 4.2V vs. Li/Li^+, corresponding to a half-delithiated state ($1 \geq x \geq \sim 0.5$) during charging, and 3V vs. Li/Li^+ during discharge, yielding a usable capacity under 150mA h g^{-1} [16].

However, due to the high reactivity of the LCO towards electrolytes in the de-lithiated state, cost and toxicity, alternative transition metal oxides are being sought [4][12]. $LiNiO_2$ is isostructural with $LiCoO_2$ and has higher gravimetric and volumetric energy density, at the cost of stability and order as compared to $LiCoO_2$. Further, during synthesis there is a tendency towards loss of lithium, which reduces some Ni to the 2+ oxidation states. The Ni^{2+}-ions can migrate to Li^+ sites, since the size of the two ions is similar. This effect is detrimental to cathode performance, but can can be mitigated by substituting some of the nickel with cobolt, yielding compounds with the stoichiometry $LiNi_{1-x}Co_xO_2$. These compounds have increased ordering and energy density compared to pure $LiNiO_2$ and $LiCoO_2$ respectively [12] [17]. Further, the limited thermal stability of $LiNiO_2$ at high states-of-charge has posed significant safety concerns, but the thermal properties as well as capacity can be improved by doping with manganese [17].

2.3.1.2 Spinels

The spinel structures, the most common being $LiMn_2O_4$ (LMO), offer several advantages compared to the layered transition metal oxides, including low cost, environmental friendliness and non-toxicity, in addition to increased thermal and

structural stability [4]. $LiMn_2O_4$ has a structure that can be considered a special case of the layered transition metal oxides, where the transition metal and lithium ions are ordered in all layers. The manganese and lithium ions occupy octahedral and tetrahedral sites respectively, which results in a three-dimensinal network of channels for lithiation and delithiation [12]. This gives the material inherently high rate capability and electronic conductivity, ideal for high-power applications [4].

Lithium insertion and de-insertion in cubic $LiMn_2O_4$ is usually limited to potentials between 4.2 and 3V vs. Li/Li^+ to a theoretical specific capacity of $148\,mA\,h\,g^{-1}$. Although further discharge yields a higher specific capacity, the increase is associated with the formation of the tetragonally distorted $Li_2Mn_2O_4$-phase. This phase transition results in a 16% increase in the c/a ratio, leading to large volume changes and rapid particle disintegration. Cycling the cathode above 4V vs. Li/Li^+ maintains the cubic structure and thus active material integrity [17].

The major drawback with $LiMn_2O_4$-based cathodes is the gradual capacity fading upon cycling, and the effect is particularly prominent at elevated temperatures. This loss is attributed to several factors, including irreversible side reactions with the electrolyte due to the high potential, loss of oxygen from the de-lithiated spinel, dissolution of manganese ions, and the formation of the tetragonal $Li_2Mn_2O_4$-phase on particle surfaces at high discharge rates [4][17][18]. Partial substitution of Mn can improve capacity retention, as does substitution of Li, at the cost of decreased lattice parameter and theoretical specific capacity. Commercial lithium-substited LMO cathodes have theoretical specific capacities between 100-120 mAh g^{-1} [17].

2.3.1.3 Polyanionic compounds

A promising new class of cathode materials are the polyanionic compounds based on phosphates ($LiMPO_4$) with the ordered olivine structure. The most common is $LiFePO_4$ (LFP), in which the oxygen ions form a somewhat distorted hexagonal-close-packed lattice with phosforous ions at tetrahedral sites, lithium and iron ions in octahedral 4a and 4c sites respectively. This yields a structure where lithium ions form 1-dimensional chains along the [0 1 0]-direction [19][4]. These channels are usually perpendicular to the long axis in small LFP particles, which are usually platelet-shaped. The delithiated $FePO_4$-phase has essentially the same structure, but with a slight orthorombic deformation and a 7% reduction in volume [20]. Lithium is inserted and de-inserted in a two-phase reaction between $LiFePO_4$ and $FePO_4$ upon cycling. Although the exact mechanism of the phase transition is under debate, the lithium ions are thought to move in a co-operative fashion through the [0 1 0] channels [20].

LFP is regarded as one of the most promising cathode materials for high-power applications and large scale energy storage. LFP offers a theoretical capacity of $170\,mA\,h\,g^{-1}$ and a flat voltage plateau at 3.45V vs. Li/Li^+, which is well

within the stability window of carbonate-based electrolytes. This makes LFP, in combination with the material's inherently high structural and thermal stability, an intrinsically safe cathode material. Further, LFP is composed of abundant, environmentally benign and biocompatible elements, and has an energy density comparable to LMO, despite being less dense [4] [14][17]. The power capabilities of LFP cathodes is also excellent, attributed to the one-dimensional lithium diffusion pathways [20].

However, two important processing steps must be included in order to overcome the poor kinetics of lithium insertion and de-insertion in LFP. Lithiation and de-lithiation is limited by a combination of slow lithium-ion phase-boundary diffusion and low electronic conductivity in both end phases [20]. Fortunately, the electronic conductivity can be increased by coating the particles with carbon, and reducing the size of the LFP particles to the nanoscale efficiently shortens lithium ion diffusion pathways. A carbon coating can be realized either by *in situ* during synthesis or *ex situ* during post-treatment. The increased electrical conductivity manifests as increased achievable specific capacity as well as improved lithiation and de-lithiation kinetics. Including a carbon source during synthesis also has the additional benefit of retarding particle growth, resulting in small particles that allow rapid lithium diffusion [4][17]. The performance of the LFP/C composites is highly dependent on the amount of carbon, degree of graphitization, morphology and distribution, which in turn is dependent on carbon precursor, synthesis conditions and sintering temperature. Carbon coatings formed at low sintering temperatures (600-700 °C) are disordered, and therefore less conductive than graphite, but the use of iron-containing graphitization catalysts can efficiently increase conductivity through formation of carbon fibers and nanotubes which wire particles together, so that small amounts of carbon (<2wt.%) is usually enough. This is important as a high carbon content has a negative effect on energy density [17] [20].

2.3.1.4 Composite cathodes

Combining several electrode materials to form a composite electrode can be used to improve performance. The addition of $LiFePO_4$ to other electrodes, including $LiCoO_2$, improves capacity retention and high-current performance. Also, spinel electrodes can be combined with layered cathode materials in order to expand the operating voltage range; Li^+ is removed from the spinel at high voltages and from the layered cathode material at lower voltages [12]. When Ni and Co is added to $LiMnO_2$, which is unstable at higher temperatures and thus hard to synthesize, the layered oxide structure is stabilized to yield compounds such as $LiNi_xMn_{1-x}O_2$, $LiMn_{1-x}Co_xO_2$ and $LiNi_xMn_{1-x-y}Co_yO_2$ [14].

Among the most common composite cathodes is $Li(Ni_{1/3}Mn_{1/3}Co_{1/3})O_2$ (NMC), which is isostructural with LCO. Compared to LCO, NMC shows enhanced structural stability at high voltages, with lower cost and toxicity. Batteries based on NMC provide a similar energy density to those based on LCO, as the operat-

ing voltage of NMC is slightly lower and capacity somewhat higher. Still, NMC cathodes suffer from similar reacitvity issues towards the electrolyte, overcharge sensitivity and low thermal stability [4].

2.3.2 Electrolytes

The choice of electrolyte is an important decision when designing lithium ion batteries. Electrolyte solutions vary in composition, but always contain a combination of a lithium salt dissolved in one or more solvents, both of which can be changed to meet the demands of a specific application.

An ideal electrolyte has the following combination of properties: the electrolyte must be electrically insulating to prevent direct charge transfer between the anode and cathode, which promotes a steady current of electrons through the external circuit. Second, to maintain the internal charge balance of the cell, high ionic conductivity is essential. Finally, the electrolyte has to remain inert during operation, and be stable towards oxidative and reductive decomposition at the positively and negatively charged electrode, respectively. Electrochemical stability can be accomplished either by passivation of the catalytically active sites on the electrode surfaces, or by thermodynamic stability of the individual electrolyte components under the operating conditions of the battery. Usually, the former is the case for lithium ion batteries. Other important factors to take into account are safety, toxicity and a wide liquid range, which is essential for low-temperature performance [21].

The majority of electrolyte compositions are based on a single lithium salt dissolved in a mixture of solvents. This can be explained from the consideration of ionic conductivity:

$$\sigma = \sum_i n_i \mu_i Z_i e \tag{2.4}$$

where n_i is the number of moles, μ_i is the mobility, Z_i is the valence of component i and e is the elementary charge. A high concentration of lithium ions, n_i, requires a solvent with high dielectric constant, which is usually connected with high viscosity and a low dissociation energy of the lithium salt. But in order to achieve high mobility of the solvated lithium ions, a solvent with low viscosity and small solvation volume is needed for rapid charge transport. A single solvent cannot fulfill these opposing requirements, and a combination of cosolvents is therefore used. The first cosolvent has a high dieletric constant responsible for dissolving the salt, and the second has low viscosity to provide little resistance for solvated Li^+-ions [21].

The most common solvents in lithium ion battery electrolytes are combinations of linear and cyclic diesters of carbonic acids (carbonates). Carbonates are stable towards oxidation, have high dielectric constants, low viscosity and the ability form a stable passivating layer on the negative electrode surface. Ethylene carbonate (EC) and propylene carbonate (PC) are common cyclic carbonates, and

especially EC is a key component in commercial electrolytes due to the superior surface chemistry created upon decomposition. Typical linear carbonates include diethyl carbonate (DEC), dimethyl carbonate (DMC) and ethylmethyl carbonate (EMC). Cyclic carbonates have a high dielectric constant and are quite viscous, while linear carbonates on the other hand have lower dielectric constants, and are less viscous due to the free movement of the alkyl substituents. However, linear carbonates tend to form unstable surface films or no film at all. The carbonate solvents have one important drawback, namely poor ionic conductivity at low temperatures, which have led to the research on ternary mixtures of carbonates to improve electrolyte performance [21].

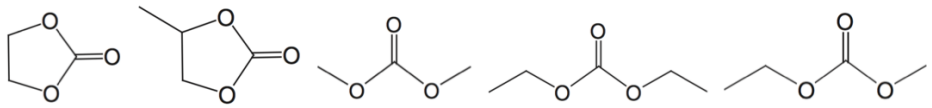

Figure 2.5: From left to right EC, PC (cyclic carbonates), DMC, DEC, EMC (linear carbonates). Modified from [21].

The most common lithium salt is $LiPF_6$, as the $PF_6{}^-$-anion is stable against oxidation, the salt has good solubility in non-aqueous solvents, and aids in the formation of passivating layers on the positive electrode surface. However, $LiPF_6$ is sensitive to moisture and reactive at elevated temperatures, which has led to the development of boron containing compounds such as $LiBF_4$, chelated borates, lithium bis(oxalato)borate and lithium difluoro(oxalato)borate. Improvements in selected properties are seen, but the overall performance of $LiPF_6$ has yet to be matched [21].

2.3.2.1 The solid-electrolyte interface

The nature of the solid-electrolyte interface is an important element to consider when choosing an electrolyte for a battery. The SEI consists of various electrolyte solvents and solutes that has undergone partial or complete reduction at the negative electrode surface, and is generally formed during the first charge. The various decomposed organic and inorganic electrolyte species form a passivating layer, which prevents further reduction of the electrolyte by prohibiting electron transfer while being permable to lithium ions.

Every physical and chemical characteristic of the SEI, such as thickness, morphology, compactness and composition, affects battery performance, so the formation of a stable passivating layer is of great importance. Unfortunately, the nature of the SEI makes it difficult to analyze, as SEI formation has no fixed onset potential, which varies between different solvents, salts and additives. Cyclic carbonates like EC tend to form semicarbonates and Li_2CO_3 which passivate surfaces efficiently, whereas linear carbonates such as PC often fail to do so. Vari-

ables such as solvent dielectric constant, viscosity and reactivity determines the properties of the formed SEI, and are thus vital selection criteria when evaluating an electrolyte solution [22].

Although the formation of a stable SEI can ensure reliable battery performance, it is also associated with an irreversible capacity loss. This loss comes from reduction of the solvent and solute, in addition to trapping of lithium ions within the SEI layer. The capacity loss can be substantial, as the thickness of the SEI can increase to several tens of nanometers with cycling. An efficient way to reduce the SEI thickness and thus limit the associated capacity loss is pretreatment of the anode surface, particularly for carbon-containing surfaces. Uniform, hard carbon surfaces promote SEIs that are thin, homogeneous and compact. Further, SEIs formed over large surface areas will necessarily lead to a larger irreversible capacity loss [23].

SEI formation also has a significant economic impact on lithium ion battery manufacturing. As manufacturers want to control the SEI as much as possible, proprietary formation cycling is employed. Formation cycling requires the installation of thousands of cycling stations, constituting a heavy capital equipment investment and a considerable production line bottleneck, in addition to a significant processing energy cost [8].

2.3.3 Anode materials

An ideal anode material fulfills the following criteria:

1. Low weight.
2. The ability to store large quantities of lithium to achieve a high gravimetric and volumetric capacity.
3. A low redox potential with respect to Li/Li^+ at all Li concentrations to give a large voltage window, resulting in high energy density.
4. Fast lithium diffusion and electronic conductivity are paramount to maximize the power density of the cell.
5. Good chemical stability, i.e. unreactive to the selected lithium salt and unsoluble in the electrolyte.
6. High safety to minimize the risk of thermal runaway.
7. Be constructed of cheap and environmentally friendly materials.

As it fulfills many of these requirements, graphite is still the most widely used commercial anode material.

Still, in order to increase the specific capacity of a finished battery, new high-capacity anode materials are required, as the specific capacity of graphite and

commercial cathode materials are limited to 140-180 and 372mA h g^{-1}, respectively [24]. As illustrated in Figure 2.6, anode materials with a specific capacity of 500mA h g^{-1} can offer a 10% increase in battery specific capacity over a graphite anode (370mA h g^{-1}) [25].

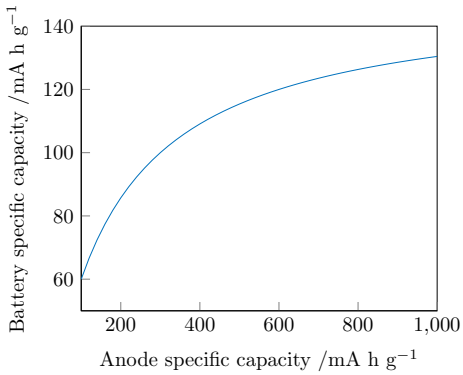

Figure 2.6: Battery specific capacity as a function anode capacity, assuming a fixed cathode capacity of 150mA h g^{-1} [25].

There are three categories of anode materials for lithium ion batteries: intercalation or insertion, conversion and alloy anodes, which differ in lithium storage mechanism, as illustrated in Figure 2.7. Insertion materials are generally characterized by their low reversible capacity and high working potential against Li/Li^+, with graphite as a notable exception. Conversion anodes on the other hand exhibit a larger reversible capacity and good power performance, at the cost of significant polarization, high working potentials, large volume changes during cycling and unstable SEI formation. Therefore, conversion anodes are not yet used in commercial cells. Alloy anodes are regarded as the most promising option for the next generation of lithium ion battery anodes. This is due to a favourable mix of high capacity, low operating potential and good power capability. However, alloy anodes face similar challenges as the conversion materials, namely large volume changes during cycling, which results in poor long-term performance [6].

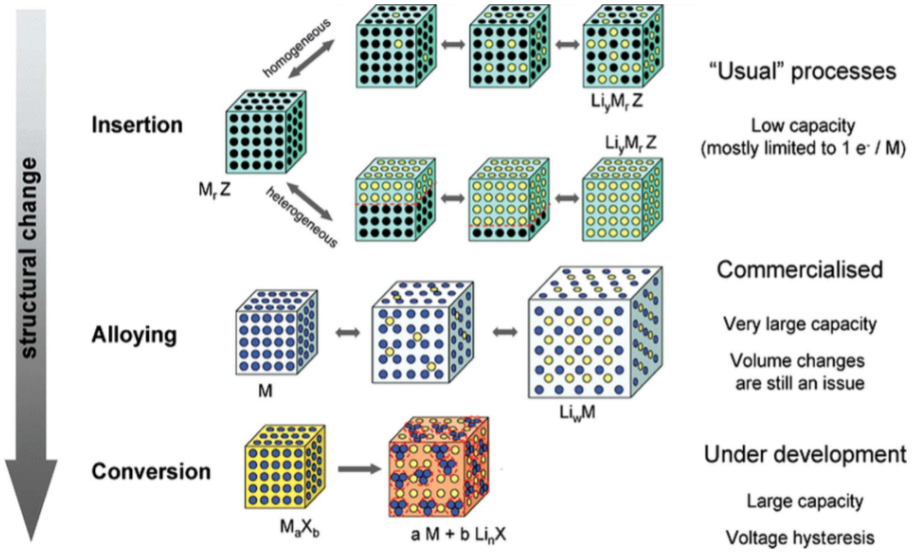

Figure 2.7: Schematic illustration of the different lithium ion storage mechanisms observed in anode materials for lithium ion batteries. Black circles: voids in the crystal structure, blue circles: metal, yellow circles: lithium [6]

2.3.3.1 Intercalation anodes

Since rechargeable lithium ion batteries were commercialized in 1991, graphite has been the de-facto industry standard anode. Graphite anodes are characterized by good cycle life, low working potential with respect to Li/Li^+ as well as low cost.

Graphite has a layered structure, consisting of stacked layers of graphene planes. The carbon atoms in the graphene planes are sp^2-hybridized with half-filled p_z orbitals perpendicular to graphene plane, which interacts with Li^+'s 2s orbitals to give reversible intercalation up to a maximum theoretical capacity of $372\,mA\,h\,g^{-1}$ based on the stoichiometry LiC_6 [21]. Lithium ion intercalation takes place in several stages at potentials below 0.2V vs. Li/Li^+, due to the fact that the expansion energy increases with the number of adjacent graphene planes on both sides of the intercalation gap in question [23].

The performance of graphite anodes are heavily dependent on the properties of the SEI formed during the intial cycling. A stable, preferably thin SEI prevents degradation of the anode from cointercalation of solvated ions, which results in irreversible exfoliation of graphene sheets. Nevertheless, SEI formation is accompanied by an irreversible capacity loss, which limits the performance of the cell [23]. Further, the rate-determining step during charging is the diffusion and intercalation of lithium ions between the graphene plances. Improved kinetics of lithium intercalation is vital in order for graphite anodes to be a viable candidate for power applications. One strategy to improve charging performance is to minimize Li^+ diffusion lengths by decreasing particle size. However, this leads to an increased irreversible capacity loss, since the SEI will form over a larger surface area [26].

Several different carbon allotropes have been employed as potential anode materials, examples include graphene, nanotubes, hard and soft carbon, either as a single anode component or in combination with other active or inactive materials. Even though some performance increases can be observed, low capacity, poor cyclability or scalability problems are significant obstacles for further development [24].

The spinel lithium titanate $Li_4Ti_5O_{12}$ (LTO) is an important intercalation compound currently being considered for large-scale energy storage systems. LTO is unique as Li^+-ions can intercalate with zero strain to a capacity of $150\,mA\,h\,g^{-1}$ at 1.5V vs. Li/Li^+ [27]. An important consequence of the high operating voltage is that no reductive decomposition of electrolyte species and resulting passivating phenomena occur, and the amount of lithium from the cathode is mostly conserved. Compared to a cell containing a graphite anode, the capacity would be higher but operating voltage lower, which yields a similar energy density overall. Further, due to the zero-strain intercalation mechanism, lithium ion battery cells containg LTO anodes can be charged approximately six times faster than graphite anodes, with improved low-temperature performance and outstanding cycle life [21].

Another interesting family of intercalation compounds are based on titanium dioxide. Theoretically, all polymorphs of TiO_2 are able to store up to one mole of Li^+-ions to give a capacity of $355\,mA\,h\,g^{-1}$ at an operating voltage similar to LTO. TiO_2 are attractive due the low cost, eco-friendliness, easy synthesis and scalability potential [6].

Other researched intercalation materials include vanadium oxides, NASICON-type materials and titanium disulfide, among others [6].

2.3.3.2 Conversion anodes

Conversion anodes are based on the following reversible reaction between a metal containing compound, MX_y (X=P, S, O, F, Cl etc.), which is electrochemically destroyed and reduced to elemental metal, M^0, in the process:

$$M_xO_y + 2\,ye^- + 2\,yLi^+ \longleftrightarrow xM^0 + yLi_2O \tag{2.5}$$

Compared to intercalation materials, conversion anodes are able do deliver a higher reversible capacity due to the multiple-electron reaction. Further, the operating voltage of the anode can be tuned to meet the demands of a specific application as the operating potential varies from metal to metal [27].

As for graphite anodes, an SEI is formed during the initial cycle, accompanied by an irreversible loss, generally larger than for carbon-based anodes. In addition, conversion anodes typically show significant polarization, high operating voltage and large volume variation during cycling, all of which are difficult challenges to overcome. Still, carbon coatings and passive matrix materials can enhance cycling performance, and the initial irreversible can be mitigated by employing sacrificial salts and pre-lithiating the anode before assembly [6].

2.3.3.3 Alloy anodes

A wide range of metallic and semi-metallic compounds can alloy reversibly with lithium in the presence of aprotic solvents. Alloy anodes provide both a very high theoretical capacity and a low operating voltage with respect to Li/Li^+ compared to insertion or conversion anodes, and are therefore essential for high-energy batteries. The group IV elements Si, Ge, Pb and Sn are especially attractive, and both Panasonic (Si) and Sony (Sn-Co-Ti-C) offer commercial alloy anodes [6].

The main problem associated with alloy anodes is the significant volume variation during lithiation and delithiation, e.g. more than 300% for amorphous silicon. The volume variation results in pulverization of the electro-active particles, a breakdown of the electrically conductive network and eventually detachment from the current collector. In addition, poor capacity retention and large first-cycle irreversible capacity loss are issues which remains largely unsolved [28]. Further, SEIs formed over alloy anodes possess notably different characteristics

from graphite anode SEIs. Due to the volume variation during alloying and dealloying, the SEI is formed in a dynamic process of detachment and reforming, which further worsens capacity retention [6][24]. The most common degradation methods of alloy anodes, represented by Si, are illustrated in Figure 2.8.

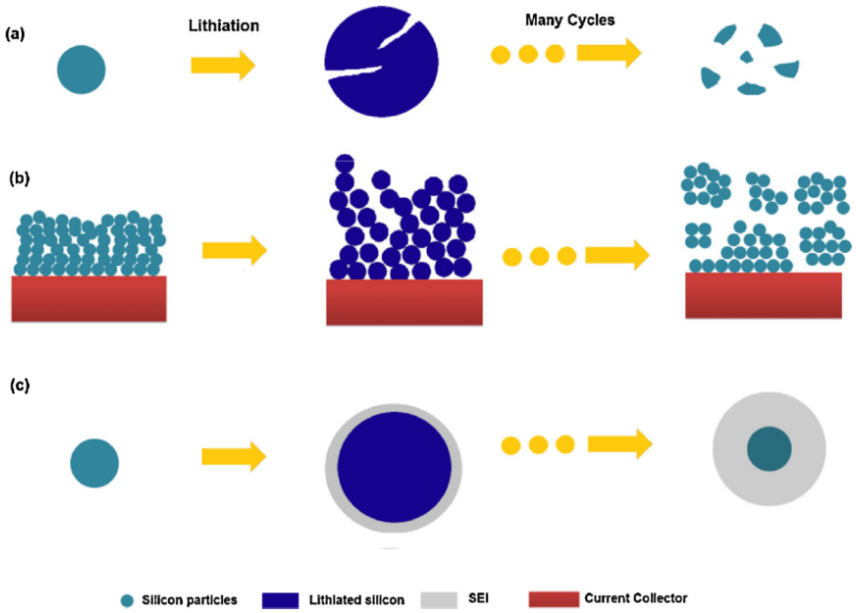

Figure 2.8: Schematic representation of the different degradation mechanisms observed in anode materials, represented by silicon. a) Material pulverization, b) morhology and volume change of the entire electrode, c) continuous SEI formation [29].

Silicon is the most investigated material to replace the industry-standard graphite anode, offering very high gravimetric and volumetric capacities, 3862 mA h g^{-1} and 9786 mA h cm^{-3} respectively, based on the stoichiometry $Li_{15}Si_4$, as well as high abundance. The safety of Si anodes is also improved compared to carbonaceous anodes, as the onset alloying potentials lies 0.3-0.4V above the potential of Li/Li^+, eliminating the risk of lithium plating or dendrite formation, which can short circuit the battery and lead to thermal runaway.

In order to mitigate the volume changes from the alloying and dealloying processes and minimize the resulting capacity fade from pulverization of the active material, a wide array of morphologies and designs have been investigated. The approaches can be divided into the following categories [28]:

1. Micro- or nanoscale pure Si structures

2. Si dispersed in an inactive matrix
3. Si dispersed in an active matrix
4. Si anodes with different binders
5. Si thin films

Due to the large volume change during cycling, cracks are induced in the silicon particles, which propagate under the tensile stress following the dealloying process. An efficient way to slow down crack propagation is to use nano-sized Si particles, as nanostructured particles can absorb the strains following the volume change, and thus avoid pulverization. *In situ* measurements show that cracks become less frequent for particles below 150 nm, even at high charge rates [24]. Reducing the size has also been shown to minimize capacity fading, but no effect is observed for the first-cycle irreversible capacity loss [28]. Examples of succesful silicon nanostructures are nanowires, thin films and yolk-shell structures, which have demonstrated a reversible capacity of 2800 $\mathrm{mA\,h\,g^{-1}}$ over 1000 cycles [29][30].

An alternative approach to contain the volume variations, is to disperse the silicon particles in a suitable matrix material, as the matrix can act as a buffer for the volume change, thus avoiding pulverization of the active particles [28]. Matrix materials typically have high mechanical strength to counteract the volume variation, and high electrical conductivity to facilitate efficient charge transfer. Further, matrix materials are either active towards Li, as is the case for Si-Ag and Si-Mg alloys, or inactive, such as Ni, Cu, Fe, Li_2O, SiC, TiC, TiN and TiB_2. Often, the cycle life of active-matrix anodes is shorter than for anodes with a mixed active-inactive matrix, and very dependent by depth of charge [31].

Carbon is the most widely used active matrix material, and carbon coatings are an efficient way to improve the performance of Si-based anodes. Carbon coatings are known to improve cycling stability due to the increased electronic conductivity and volume buffering effect. Further, carbon coatings can be fabricated using a variety of techniques and precursors, ranging from chemical vapour deposition to pyrolysis of carbon-containing precursors [31]. An in-depth discussion of carbon coatings will be provided in the context of silica anodes.

The choice of binder and the overall binder content can significantly influence the cycling performance of powderous Si-based anodes. A binder is added to maintain the structural integrity of the electroactive particles, and keep them attatched to the current collector. Polyvinylidene fluoride (PVDF) is one of the most common binder materials used for silicon-based anodes. However, as PVDF is a thermoplastic, it shows negligible elongation and may not be able to endure the volume change of the Si particles during alloying and dealloying. This has led to development of alternative binders, which include cross-linked polyethylene glycol with lithium perchlorate, rubber-like polyisobutene and electronically conductive polypyrrole [28]. Another recently developed binder material is alginate,

a naturally occuring polysaccharide extraced from the cell walls of brown algae. When used in conjunction with silicon active material, an anode with very high reversible capacity and cycling stability results [32]. Alginate binders perform well with Si due to the large amounts of carboxy groups in binder, which can form hydrogen bonds to SiO_2 present on the surface of the Si particles. As hydrogen bonds can form and reform easily, this leads to a self-healing effect if the binder-particle bond is broken, efficiently stabilizing the particles against pulverization [32]. Further, the alginate binder allows easy access of Li^+-ions to the surface of the active particles, and interacts weakly with the electrolyte, which helps to form a stable SEI [33].

An alternative way to use silicon as an anode materials is by forming thin films. The major benefit of thin film anodes is the lack of inactive materials such as binders and conductive fillers. This gives thin films anodes increased specific capacity and energy density compared to powder-based anodes [29]. In addition to high reversible capacity, thin film anodes typically show good cycling stability, attributed to the strong adhesion to the current collector [24].

2.4 Silica-based anodes

Silica (SiO_2) has recently come to light as a potential anode material for the next generation of high-energy lithium ion batteries. (SiO_2) shares the advantages of elemental silicon, providing a high theoretical capacity at a low operating potential vs. Li/Li^+, but in addition silica is environmentally friendly and obtainable at a very low cost from a range of organic and inorganic sources.

Silica was presumed to be electrochemically inactive towards lithium until Gao *et al.* found that commercial 7nm SiO_2 particles could react with lithium at an operating voltage between 0 and 1.0V vs. Li/Li^+ to a reversible capacity of $400\,mA\,h\,g^{-1}$ [34]. Since then, a multitude of silica structures and morphologies have been investigated for use as an anode material in lithium ion batteries, most of which are summarized in Table 2.4.

Although silica is a promising substitute for today's graphite anodes, the material shares many of the challenges facing elemental silicon anodes. Both materials suffer from large volume variations upon cycling and subsequent capacity fade from pulverization of the active particles, relatively poor electronic conductivity and a substantial irreversible capacity loss during the initial cycle. As the surface chemistry is similar, and both materials share chemical constituents, many of the same strategies and solutions applied to silicon anodes can be employed for silica anodes.

The two most common solutions to the aforementioned problems are matrix materials, commonly carbon, and employing nanosized, hollow or porous particles. A conductive matrix can simultaneously improve electrical conductivity and contain the volume changes, while nano-sized, hollow, porous particles provide good electrolyte access, short diffusion pathways for solvated Li^+ ions and room for

the particle to to expand during lithiation.

These measures are of great importance, as they promote good Coulombic efficiency, i.e minimizing loss of lithium, during cycling. This is important as the large irreversible capacity losses during the initial cycle limits the usable capacity of the anode. The low efficiency is associated with the formation of an inactive matrix of lithium oxide and lithium silicates in the silica nanoparticles, in addition to SEI formation. This matrix is crucial for stabilizing the volume change during cycling, and is thus difficult to reduce.

2.4.1 Lithium storage mechanism

The lithium storage mechanism for SiO_2-based anodes was first investigated by Sun *et al.*, with a combination of *ex situ* transmission electron microscopy, select-area electron diffraction and X-ray photoelectron spectroscopy (XPS) measurements [58]. A Li-Si alloying reaction and a conversion reaction from SiO_2 to $Li_2Si_2O_5$ was suggested:

$$5\,SiO_2 + 4\,Li^+ + 4\,e^- \rightleftharpoons 2\,Li_2Si_2O_5 + Si \tag{2.6}$$

$$Si + xLi^+ + xe^- \rightleftharpoons Li_xSi \tag{2.7}$$

From Reaction 2.6, a theoretical reversible capacity of 749mA h g^{-1} was calculated, assuming that the $Li_{22}Si_5$-alloy is the final product [52]. The elemental silicon can alloy with lithium ions to form Li-Si alloys when the material is discharged below 0.25V vs. Li/Li^+. Hence, SiO_2 is defined as an alloy anode material, even though the material itself is an oxide.

This mechanism was later re-examined by Guo *et al.* [57]. From several XPS experiments, a mechanism where the nanosized SiO_2 was reduced to silicon and crystalline Li_4SiO_4 or amorphous Li_2O during the first lithiation was proposed:

$$SiO_2 + 4\,Li^+ + 4\,e^- \longrightarrow Li_4SiO_4 + Si \tag{2.8}$$

$$SiO_2 + 4\,Li^+ + 4\,e^- \longrightarrow 2\,Li_2O + Si \tag{2.9}$$

From equations 2.7 and 2.9 a theoretical reversible capacity of 1965 mA h g^{-1} was calculated, again assuming $Li_{22}Si_5$ as the end product. If the initial discharge proceeds according to 2.8, the theoretical specific capacity is reduced to 983 mA h g^{-1} [57].

Yan *et al.* affirmed the formation of $Li_2Si_2O_5$, Li_4SiO_4, Li_2O and pure Si, also by employing XPS [52]. From this result is was put forward that the reversible formation of $Li_2Si_2O_5$, and the irreversible emergence of Li_4SiO_4 and Li_2O phases co-occur. A similar development has been observed using ball-milled quartz as an anode material [53]. It is important to note that lithium will be irreversibly bound in the initial lithiation of the anode, resulting in a large irreversible capacity loss, regardless of which reaction mechanism is dominant.

Table 2.4: Morphology, reversible capacity, cycling performance, initial Coulombic efficiency and capacity retention for a variety of silica-based anode materials [35].

Morphology	**Reversible capacity, mA h g^{-1}**	**Cycling performance**	**Initial Coulombic efficiency**	**Capacity retention**
Binder-free silicon/silica/C nanofiber [36]	733	50 cycles	71.1%	69.7%
Nanoflake Si@SiO_2 [37]	1920, 100 mA g^{-1}	100 cycles	84.6%	75.7%
Hollow submicron SiO_2-C composite [38]	662	100 cycles	43%	91%
Dual-porosity SiO_2/C nanocomposite [39]	635.7	200 cycles	30%	99%
Graphene nanoplatelet supported SiO_x/C [40]	630	250 cycles	67.7%	99%
3D SiO_2@Graphene aerogel [41]	450	3 cycles	43.5%	97%
Hollow porous SiO_2 nanobelts [42]	860	100 cycles	50%	95%
SiO_x-C composite [43]	674.8	100 cycles	85%	83.5%
Electrospun SiO_2/C composite [44]	658	100 cycles	57%	97%
Hollow SiO_2 hard-templated nanotubes [45]	1266	100 cycles	43.3%	Negligible capacity loss
Mesoporous carbon@silicon-silica nanostructure [46]	920	100 cycles	44%	99%
Diatoms containing porous silica [7]	500	80 cycles	50%	94%
SiO_2/C by sol-gel and ball milling [47]	663	30 cycles	54%	98%
SiO_2@C@Graphene, hydrothermal synthesis [48]	225	200 cycles	36.1%	98%
Nanosilica/carbon composite spheres [9]	620	300 cycles	66.4%	100%
400nm amorphous SiO_2 spheres [49]	876.7	500 cycles	54.8%	Increases the first 300 cycles
SiO_2/Cu/polyacrylonitrile-C composite by ball milling [50]	537	200 cycles	72.2%	100%
Amorphous SiO2/C composite via sol–gel and ball milling [51]	600	100 cycles	72%	Increases during the first 20 cycles
150nm hollow porous SiO_2 nanocubes [52]	919	30 cycles	47%	Increases the first few cycles
SiO_2 from high-energy mechanical milling of quartz [53]	800	200 cycles	37%	82%
Si@SiO_x/C nanoporous spheres, magnesiothermic reduction [54]	913	60 cycles	44%	97%
30nm hollow silica nanospheres, templated [55]	355	500 cycles	48%	94%
Carbon-coated SiO_2 nanospheres, sucrose [56]	536	50 cycles	60%	93%
HC-SiO_2 by hydrothermal synthesis [57]	630	15 cycles	62%	100%
SiO_2 thin film by RF sputtering [58]	465	100 cycles	86%	87%

By examining Reactions 2.6, 2.8 and 2.9, it is apparent that the formation of Si and Li_2O results in the highest reversible capacity. A common hypothesis is that small SiO_2 nanoparticles tend to form Li_2O instead of Li_4SiO_4 or $Li_2Si_2O_5$, possibly because of quicker lithium ion diffusion kinetics [57]. Therefore, decreasing particle size or increasing surface area by using hollow, porous structures can favor the yield of reaction 2.9 [52]. From Table 2.4 it is observed that hollow porous particles with large surface areas, such as nanocubes and nanowires, show higher reversible capacities and enhanced cycling performance compared to solid particles.

The created Li_2O-phase is advantageous in two ways. First, from reactions 2.6, 2.8 and 2.9, note that SiO_2 is fully converted to silicon and stored lithium for the latter. This minimizes the initial irreversible capacity loss and results in the highest reversible capacity. Second, the Li_2O forms a microstructure in the active material where silicon nanodomains are nested in an inactive Li_2O matrix, which buffers the volume changes of Si and diminishes the unwanted side effects of the excess volume change [24].

2.4.2 The importance of carbon

When silica is used as an anode material, a conductive element is necessary to enhance the electrical conductivity of the anode, as pure silica is electrically insulating. Carbon is by far the most common additive, either used to form a composite or as a coating material.

The inclusion of carbon has several advantages. Most importantly, carbon has high electronic conductivity, and when added to an electrode, the internal resistance is decreased, performance at high current density is enhanced and internal heating is prevented. As shown in Figure 2.9b, when a particle is uniformly coated by carbon, the current is distributed more homogeneously around the particle, which results in shortened Li^+ diffusion pathways. Second, carbon has a large chemical and electrochemical stabiliy window in organic solvents, which improves the safety, lifetime and shelf-life of carbon coated anodes. Carbon is only electrochemically active towards the electrolyte at very low potentials, which combined with excellent chemical resistance, makes carbon a good coating material. Further, carbon coatings adhere well to curved and rough surfaces, and its high strenght allows the coating to serve as an elastic shell to contain the volume change of the active material, which prevents active material pulverization. Lastly, carbon coatings can be produced using a range of techniques, and carbon precursors, such as starch, pitch, polymers and hydrocarbons, are widely available at low cost [23].

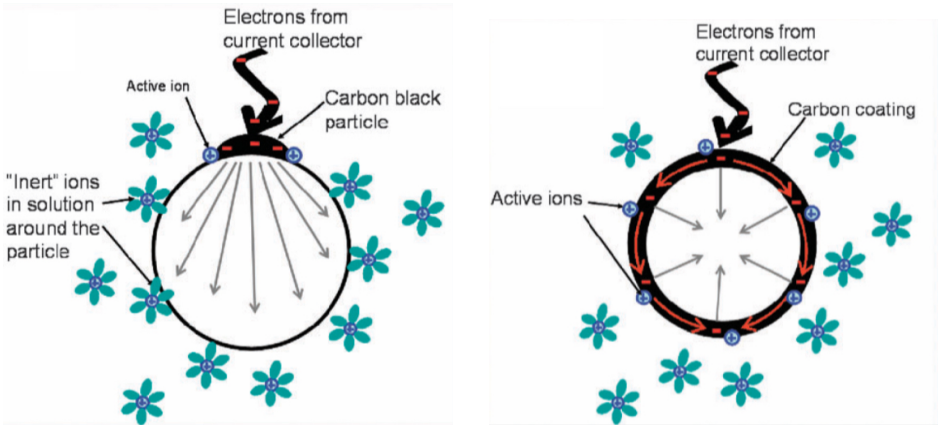

(a) Carbon point contact.

(b) Carbon coating.

Figure 2.9: Schematic illustration of the difference between carbon coating and a carbon point contact. Note the significantly reduced lithium diffusion length due to the increased electronic conductivity and homogeneous current distribution. Modified from [23].

Carbon coatings are also known to improve capacity retention, and decrease the first-cycle irreversible capacity loss concomitant with SEI formation in alloy anodes. The presence of a carbonaceous, solid outer shell which stays intact during the alloying-dealloying processes, circumvents the problem of continuous SEI formation, as the formed SEI remains stable. Thin, hard, carbon shells also tend to promote thin, homogeneous SEIs, which consume less lithium during formation [24][23].

The benefit of a uniform carbon coating for silica anodes was demonstrated by Yao *et al.*. Two samples with identical stoichiometry were prepared, the first consisting of silica spheres wet-mixed with sucrose and calcined in an inert atmosphere to give a homogeneous coating and the second consisting of dry-mixed silca spheres and carbon black. The carbon coated SiO_2 showed a significant increase in reversible discharge capacity, and 60% smaller electrochemical impedance compared to the stoichiometrically equivalent dry-mixed sample. The increase was attributed to the improved electronic contact between the silica spheres and the carbon [56].

Further, Li *et al.* examined the cycle performance of carbon-coated silica spheres and otherwise identical uncoated spheres. The authors found that the lack of a carbon coating caused a low reversible capacity of only $29\,\mathrm{mA\,h\,g^{-1}}$, severe polarization and rapid capacity fade. After carbon coating, the silica spheres demonstrated a reversible capacity of $620\,\mathrm{mA\,h\,g^{-1}}$, and excellent cycling properties. The carbon coating was shown to efficiently buffer the volume change of the active particles and increased the electronic conductivity of the

anode [9].

2.4.3 Porosity

Hollow, porous silica particles, including nanocubes, nanospheres, nanobelts and nanorods, are an attractive way to use silica as an anode material. Compared to solid particles, hollow, porous particles exhibit comparatively higher reversible capacities and improved cycling performance, even without carbon coating in some cases, *cf.* Table 2.4. The capacity increase has in part been credited to the faster lithium ion transport kinetics, favouring the creation of a Li_2O inactive matrix as discussed in Chapter 2.4.1.

Further, the greater surface area and thinner walls of hollow, porous particles significantly improves the rate performance of the material, due to better electrolyte access and the significantly reduced lithium ion diffusion path length. Additionally, the large amount of internal voids provide free space for the material to expand into, which alleviates the mechanical stresses induced during lithiation and delithiation [52]. Another advantage of hollow structures is that the overall size of the active material remains unchanged during cycling. This overcomes the problem of continuous SEI formation, because no new unpassivated surface is exposed during operation [45].

However, there are two important drawbacks associated with the increased surface area of hollow, porous particles. First, Table 2.4 shows that hollow, porous structures display poor first-cycle Coulombic efficiency compared to solid particles. This is a consequence of the SEI forming over a larger area, which consumes more Li^+ in the process. Second, scalability is a concern, as hollow, porous structures often require sophisticated, time-consuming or expensive synthesis methods or precursors.

The effect of porosity has been demonstrated in several works. Li *et al.* fabricated mesoporous SiO_2 nanoparticles with a diameter of 120nm using a sol-gel approach, and added a carbon nanocomposite with dual porosity. Both the pristine and carbon-coated mesoporous nanoparticles were cycled, showing reversible capacities of 180 and 635 $mA\,h\,g^{-1}$, respectively. Even without a carbon coating, the porous silica nanoparticles exhibited excellent rate capability, attributed to the small size, large surface area and the available free space for volume expansion [39]. The performance of hollow, porous structure can be improved even further, as demonstrated by Sasidharan *et al.*, who fabricated hollow silica nanospheres with a uniform size of 30nm. The hollow particles exhibited a reversible capacity of 355 $mA\,h\,g^{-1}$, with 94% capacity retention over 500 cycles without a carbon coating [55]. Another example is hollow, porous nanotubes synthesized by Favors *et al.*, which showed the highest reversible specific capacity of reported pure silica anodes; 1266 $mA\,h\,g^{-1}$ over 100 cycles [45].

2.4.4 Binder choice

The impact of various binder materials on anode performance has been extensively studied for silicon, while work on binder materials for silica anodes is limited. However, as both materials are classified as alloy anodes and share a common surface chemistry, it is reasonable to assume that the same selection criteria apply. Therefore, a sodium alginate binder was chosen for this work, due to its good compatability with silicon-containing surfaces, ability to self-heal and assist in SEI formation.

An important consequence of this binder choice is that slurry preparation of silica anodes can be performed with water as a solvent, thereby replacing N-methyl-2-pyrrolidone (NMP) which is used in conjunction with PVDF binders. This reduces the hazard of slurry preparation, and has significant consequences for large-scale battery fabrication. The purchasing and handling of NMP adds significant manufacturing costs as well as capital costs, as NMP is expensive and volatile, requiring recovery by multiple condensers or distillation towers, and explosion-proof coating line equipment [8].

2.5 Alloy anode full cells

To the best of the author's knowledge, no works have been published on the use of silica anodes in a full cell configuration. Therefore, this section will discuss the use of alloy anodes, predominantly silicon and silicon monoxide, in full cells.

2.5.1 Improvement of energy density using high capacity materials

The most apparent reason to employ high-capacity materials is to increase the energy density of the battery. The energy density of a battery can be estimated using the specific capacities of the active materials and the following relation:

$$ED = \frac{C_{cathode} \cdot C_{anode}}{C_{cathode} + C_{anode}} V_{nominal} \tag{2.10}$$

Hence, there are two main ways of increasing the energy density of the battery; using high-capacity active materials and increasing the nominal cell voltage.

Additionally, the capacity of the active materials is closely related to the battery production costs. Increasing the capacity of the active materials effectively reduces the amount of material required, as well as the amount of electrode, per cell. This results in improved processing speed and lower cost. Further, the increased energy density also opens the possibility to reduce cell size and number of cells required to achieve a given capacity, simultaneously reducing system complexity, boosting packaging efficiency and lowering the amount of cell hardware [59].

2.5.2 Overcoming the large first-cycle irreversible capacity loss by prelithiation

The amount of lithium present in a given cell is limited by the lithium content of the cathode. Therefore, it is vital to avoid losing cyclable lithium in the first charge-discharge cycle. A large irreversible capacity loss will require an excess amount of cathode material solely for the first cycle, simultaneously lowering the energy density, increasing the cost of the battery, and the risk of lithium plating as a concequence of excess cathode capacity [59]. A current commercial graphite anode has an irreversible capacity loss of approximately 15% at low current densities, which is the acceptable limit for practical cells [60]. Hence, the irreversible capacity loss of a common alloy anode will in most cases be too large to use directly in a full cell configuration, and protocols to improve the Coulombic efficiency in the first cycle may be necessary.

One of the most common ways to minimize the first-cycle lithium loss is to prelithiate the anode prior to assembling the battery. This is an attractive option for silica anodes, as the long-term cycling performance depends on the formation of a Li_2O and lithium silicate matrix, as well as a stable SEI, in the initial cycle. By prelithiating the anode, the stabilizing matrix and SEI can form completely with an excess supply of lithium, likely to result in improved first-cycle Coulombic efficiency and long-term performance of the full cell battery.

The degree of lithiation is a critical factor for stable full cell operation. Insufficient lithiation will leave parts of the SiO_2-matrix unreacted and available to trap lithium ions, while overlithiation will eliminate the possibility of accepting Li^+ during the actual alloying reaction in the first charge of the full cell. This may result in lithium plating and dendrite growth due to overlithiation. Ideally, lithiation should be carried out to a potential below that which forms the SEI, but above the potential which progresses the alloying to a large extent. Thus electrolyte decomposition in the finished full cell is circumvented, and the anode will have enough capacity to accomodate the lithium ions from the cathode [60].

Prelithiation of alloy anodes can be succesfully achieved using a variety of methods, including solution processes, heat treatment with lithium metal powder, cycling in a half cell with an elemental lithium counter electrode, lithim-coated separators, and spontaneous self-discharge by short-circuting [60][61][62].

An important aspect to consider when choosing an appropriate prelithiation technique is the consequences for large scale production, e.g. roll-to-roll implementability and cost. The easiest way to achieve prelithiation is to treat the anode precursor prior to slurry preparation. Yom *et al.* demonstrated succesful prelithiation of SiO by heat treatment at 600 °C in argon with lithium metal. The irreversible Li_2O and lithium silicate phases that evolve during the first charge cycle were succesfully formed during the treatment, thereby reducing the first-cycle irreversible capacity loss of the anode from 41 to 18%. The prelithiated anode was tested in a full cell with a $LiCoO_2$ cathode, and showed a capacity retention of 80% over 15 cycles [61].

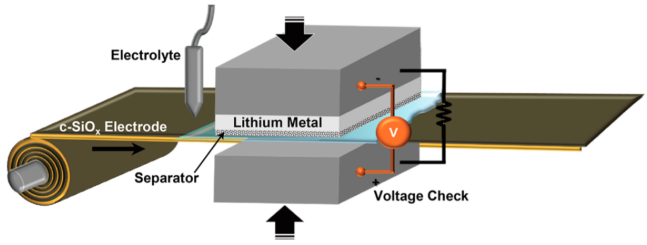

Figure 2.10: Roll-to-roll prelithiation scheme. Adapted from [60].

Another succesful approach was demonstrated by Kim *et al.* and Chae *et al.*, where a SiO and Si/C composite, respectively, was prelithiated using a self-discharge mechanism. The anode was placed in contact with lithium metal through the electrolyte solution, and the potential between the electrodes monitored. Prelithiation was stopped when the potential dropped below the SEI formation potential to avoid overlithiation. The irreversible capacity loss in a full cell configuration was decreased from 42 to 15% in the case of SiO and 43 to 19% in the case of the Si/C composite. Both full cells showed stable cycling over 100 cycles and improved energy density compared to commercial graphite-based full cells [60][63]. The main benefit of this method is the scalability potential, as it can be implemented on a roll-to-roll basis, and prelithiation time is short. A schematic is shown in Figure 2.10.

2.5.3 Maintaining high Coulombic efficiency during cycling

After the initial cycle, the most important aspect to consider is the Coulombic efficiency of the battery. A Coulombic efficiency of $> 99.95\%$ from cycle to cycle, or ideally higher, is essential to avoid losing cyclable lithium during operation to maximize the lifetime of the battery. A secondary battery is generally considered dead when the reversible capacity drops to 60-80% of the initial capacity. If 0.05% of the cyclable lithium is lost each cycle, the battery will be considered dead after only 500 cycles [59].

The effect of poor Coulombic efficiency in an NMC vs. Si/C full cell has been demonstrated by Kierzek *et al.*. As both electrodes exhibited poor Coulombic efficiency after the initial cycle, a rapid capacity decay of 28% over 100 cycles was oberseved [64].

An attractive way to improve capacity retention in a full cell with an alloy anode is to use SEI promoting agents as an additive to the electrolyte. Fluoroethyl carbonate (FEC) is a common example, and several studies have shown it's ability to improve cycling stability, decrease irreversible capacity loss and lower the resistance of the SEI [59][60][65]. Chae *et al.* found that the addition of FEC decreased the initial irreversible capacity of a $Li(Ni_{0.75}Co_{0.1}Mn_{0.15})O_2$ vs. Si/C

full cell slightly, but improved capacity retention from 90.2 to 92.4% over 100 cycles [63].

Beyond improving the intrinsic properties of the electrode materials, there are several ways to increase the lifetime of lithium ion batteries. Limiting both the cell voltage charge and discharge potentials will increase the lifetime of the battery, at the cost of decreased capacity and consequently energy density. Overcharge is especially detrimental to battery performance, as the cathode crystal structures are unstable in their delithiated states, which can cause transition metal atoms to move to lithium sites, thereby blocking the re-entry of Li^+, which decreases the capacity of the cathode. Further, the operating temperature of the battery should be kept near room temperature. Exposure to high temperature is in many cases more detrimental to the battery than cycling, especially in conjunction with high state-of-charge. However, too low temperatures will increase the viscosity of the electrolyte, efficiently increasing the resistance and lowering the reversible capacity [66].

2.5.4 Anode to cathode loading ratio

A less obvious point to consider is the ratio of anode-to-cathode loading. In practice, an excess anode capacity is used to avoid a potential drop below 0 V vs. Li/Li^+ at elevated current densities. This decreases the risk of lithium plating and thermal runaway, enhancing the safety of the battery [64].

The anode and cathode loadings will also influence the charge and discharge cell voltage cut-off potentials to a large degree, as the potential of the electrodes will change as a function of capacity. An optimized ratio of anode to cathode capacity is therefore an essential variable in the design of lithium ion battery full cells.

3 Experimental

The experimental work can be divided into multiple phases. First, the anode active material was prepared by cleaning the as-recieved diatom precursor from Planktonic AS, gently wet mixing the clean silica precursor with a carbon precursor and subjecting the obtained powder to heat treated in an inert atmosphere. The anode active material was then characterized using FE-SEM, XRD and TGA, in addition to surface area and porosity measurements. Second, the prepared anode material and the commercial cathode active materials were tapecasted onto copper and aluminium foil respectively, and assembled into coin cells. Half cells containing the individual active materials where then tested using galvanostatic cycling, cycling at different current densities and cyclic voltammetry. Finally, full cells containing both fresh and prelithiated diatom-based anodes and the commercial cathode materials were tested in the same way as the half-cells. Poor initial Coulombic efficiency was identified as the limiting factor, and strategies to improve the reversible capacity was explored.

3.1 Anode material preparation

The anode active material was prepared in the following fashion:

1. The as-recieved diatoms from Planktonic AS were dried for 36 hours at 120 °C.

2. The dried diatoms were then cleaned using the procedure explained in subsection 3.1.1.

3. The cleaned diatoms were baked at 650 °C in synthetic air for 2 hours to remove any organic matter.

4. Following the baking step, the pure SiO_2-nanostructures where then wet-mixed with 80wt.% cornstarch and ethanol to form a slurry. This slurry was thoroughly mixed in an beaker using a magnetic stirrer until all the ethanol had evaporated. Sucrose was also tried as carbon precursor using water as solvent.

5. The dry, mixed powder was transferred to a crucible and heated at 650 °C in a flowing argon atmosphere for 2 hours to form a carbon coating. An increased heat-treatment time of 8 hours was also investigated.

The various diatom-based active materials will be referred to according to the nomenclature listed in Table 3.1.

Table 3.1: Anode active material nomenclature.

Nomenclature	Carbon precursor	Weight percentage carbon precursor [%]	Heat treatment [°C]
SiO_2/C-st80	Cornstarch	80	650, 2 hours
SiO_2/C-su80	Sucrose	80	650, 2 hours
SiO_2/C-st80-8h	Cornstarch	80	650, 8 hours

3.1.1 Diatom cleaning

The received diatoms where cleaned according to the following procedure:

1. The dried diatoms were rinsed under running water and added to a large volume of deionized water, keeping the ratio of diatoms to water between 1:70 and 1:100.
2. The water temperature was increased to 130 °C under stirring at 500rpm for two hours.
3. After the initial boiling, the temperature was reduced to 80 °C, still under stirring at 500rpm.
4. A sieve of mesh size 63 µm was used to drain the excess hot water.
5. Fresh deionized water was added to the sample, with a ratio of diatoms to water of 1:50. The beaker was then immersed in an ultrasonic bath and sonicated for 30 minutes.
6. The diatoms were washed under flowing water for five minutes, dried at 90 °C for 24 hours in a drying oven, and finally dried for 18 hours in a vacuum oven at 10^{-5}bar at 150 °C.

3.2 Sodium alginate binder preparation

The sodium alginate binder was prepared from the sodium salt of alginic acid (Na-Alg, Sigma Aldrich). The ratio of Na-Alg (mass in grams), deionized water (volume in mL) and ethanol (volume in mL) in the binder was kept at 1:60:6. First, the sodium alginate was added to ethanol under stirring. Slowly, the temperature was increased to 100 °C, and the deionized water added to the mixture. The container was covered, and the binder stirred at 500 rpm and 50 °C for 18 hours.

3.3 Cathode material preparation

The cathodes used in this work were all commercially sourced, with the technical information summarized in Table 3.2.

In the case of LFP, the same carbon coating procedure as for the SiO_2/C was used; wet-mixing the recieved powder with 10wt.% or 25wt.% cornstarch and ethanol, and baking at 650 °C in a flowing argon atmosphere for 5 hours to form a carbon coating. These composites will be referred to as LFP/C-st10 and LFP/C-st25.

Table 3.2: Cathode material technical information.

Material	Producer	Purity [%]	Particle size (BET)
$Li(Ni_{1/3}Mn_{1/3}Co_{1/3})O_2$	Sigma-Aldrich	>98	<0.5 µm
$LiMn_2O_4$	Sigma-Aldrich	>99	<0.5 µm
$LiFePO_4$	Sigma-Aldrich	>97	<5 µm

3.4 Active material characterization

The prepared SiO_2/C anode material was characterized using a variety of techniques to facilitate in the interpretation of the electrochemical data. Field-emission gun scanning electron microscopy (Zeiss Supra 55 VP) was used to investigate the morphology and surface structure of the heat-treated, organics-free diatoms. Accelerating voltages and working distances of 10 kV and 5-7mm were used.

Thermogravimetric analysis (Netzsch STA 449 C) was performed to determine the amount of carbon present in the SiO_2/C and LFP/C active material. Approximately 10 mg of each powder was transferred to a small Al_2O_3 crucible and heated to 850 °C at a rate of 10 °C min^{-1} using synthetic air as the protective gas. The change in mass as a function of temperature and time was recorded.

The organics-free diatoms, carbon-coated SiO_2/C anodes, LFP and LFP/C cathodes were prepared for XRD analysis (Bruker D8 Advance DaVinci, 5°-75°, 2.33°min^{-1}, CuK_α radiation) by depositing a small amount of the powders onto a flat, silicon sample holder and adding a few drops of ethanol. Any large agglomorates were crushed with a spatula to yield a uniform coating of fine powder on the holder.

Nitrogen adsorption measurements were carried out on Tristar 3000 Surface Area and Porosity Analyzer at liquid nitrogen temperature (−195.85 °C) to investigate the Brunauer-Emmett-Teller (BET) specific surface area of the active materials. T-plot theory was employed to quantify micropore and external surface area for the organics-free diatoms and the different active materials. Before the measurements were started, the samples were degassed overnight at 250 °C.

3.5 Cell specification

In this work, stainless steel 2016 cells from Hohsen Corp. were used for assembly of the half and full cells. A schematic is shown in Figure 3.1. From bottom to top, the coin cell contains the cathode, a Celgard polymer separator and finally the anode. The case and cap of the battery hermetically seals these components with a plastic gasket, and metal spacers are used to fill any additional free space.

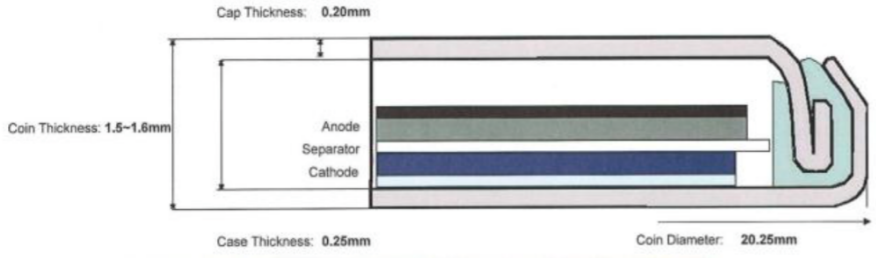

Figure 3.1: Partial cross-sectional view of a Hohsen 2016 coin cell, including cell dimensions [67].

When the SiO_2/C electrode is tested in a half cell configuration using a pure lithium counter electrode, the SiO_2/C electrode will act as a cathode and the lithium electrode as an anode, even though both are negative electrode (anode) materials. Silica simply has a higher potential vs. Li/Li^+, and will therefore act as a cathode in a half-cell assembly with lithium metal as the counter electrode.

3.6 Cell manufacture

3.6.1 Tape casting of electrode sheets

The anode electrode sheets were prepared by mixing the SiO_2/C active material (50wt.%) with carbon black (35wt.%, Timcal Super P) and sodium alginate binder (15wt.%), using a Retsch MM 400 mixing mill to form a homogeneous slurry. The slurry was then tape casted onto a copper foil current collector.

The cathode materials were prepared in a similar fashion. The cathode active material (80wt.%) was mixed with carbon black (10wt.%) and a 1:20 weight ratio PVDF binder (Kynar, reagent grade) dissolved in NMP (Sigma Aldrich, >99%), and casted on aluminium foil.

Following the tape cast, the wet film was dried for 2 hours on the tape caster at 60 °C before being placed in a Binder VD 23 vacuum oven overnight at 90 °C and 10^{-5}bar. The sample was then transferred to an argon-filled MBraun glove box to limit air and moisture exposure.

Several tape casts with different loadings of cathode and anode materials was tried, in order to strike a good balance between electrode loading and sufficient electrolyte penetration. The cathode casts were made with as high loading as possible, and the anode cast thickness was dimensioned to give approximately 10% excess capacity for the highest cathode loading, summarized in Table 3.3.

Table 3.3: Representative loadings of the different active materials.

Material	Reversible capacity [mA h g^{-1}]	Loading [mg]	Nominal capacity [µA h]
SiO_2/C-st80-8h	450	0.6	360
LMO	100	3.2	288
NMC	80	3.6	324
LFP/C-st10	60	2.4	144
LFP/C-st25	70	2.4	168

3.6.2 Cell assembly

The cells were assembled in an argon-filled MBraun glove box with less than 0.1ppm O_2 and H_2O.

Circular electrodes with a diameter of 16mm were cut from the tape casted electrode sheets, weighed and placed in the bottom of the coin cells. 15 µL 1:1 volume ratio of EC:DEC, 1M $LiPF_6$ electrolyte solution (Sigma-Aldrich, battery grade <15ppm H_2O, <50ppm HF) was applied to the cathode, followed by a 18mm Celgard 2320 ion-conducting polymer film of 20 µm thickness and another 15 µL of electrolyte to fully soak the separator and electrode. For the half cell assemblies, a 14mm counter electrode was cut from 0.75mm thick lithium foil (Alpha Aesar, 99.9%), and placed on top of the separator, followed by a 0.3mm stainless steel spacer and the battery cap. In the full cell assemblies, the lithium counter was replaced with a SiO_2/C-st80-8h anode, and followed by two 0.5mm spacers. The finished cells were hermetically sealed using a crimping machine (Hohsen Corporation).

Three-electrode cells (EL-CELL ECC-Ref) for cyclic volammetry (CV) where fabricated in a similar fashion, except for the addition of a second Li reference electrode, a 1.55 mm-thick glass fiber separator (EL-CELL) and an excess amount of electrolyte, approximately 50 µL.

3.7 Electrochemical testing

The electrochemical performance of the materials was investigated by a two-step approach. First, half cells containing lithium counter electrodes were prepared

and tested to investigate the electrochemical properties of the individual materials. Second, full cell assemblies with SiO_2/C anodes and commercial cathodes where evaluated. Cell combinations where cycled both galvanostatically and rate tested on a Lahne CT2001A computer-controlled multichannel battery tester.

Different C-rates where used for the electrochemical testing. A current density of 1C is defined as the current density that would charge or discharge and ideal cell with theoretical capacity completely in one hour. Consequently, a rate of 0.5C will charge or discharge an ideal cell in two hours, and so forth.

3.7.1 Half cell assemblies

All half cell assemblies where cycled galvanostatically at $50\,mA\,g^{-1}$ for 100 cycles, but at slighlty different conditions, as summarized in Table 3.4.

Table 3.4: Cycling conditions for the half cell assemblies.

Cathode	Theoretical capacity [$mA\,h\,g^{-1}$]	C-rate at $50\,mA\,g^{-1}$	Voltage limits [V]
SiO_2/C	2000	0.025C	0-3
LMO	100	0.5C	4.5-3.4
NMC	160	0.3C	4.2-2.5
LFP/C	160	0.3C	4.2-2.7

The rate tests were performed as follows, using the same conditions described in Table 3.4:

- 10 cycles of galvanostatic charge-discharge at $50\,mA\,g^{-1}$.
- 10 cycles of galvanostatic charge-discharge at $100\,mA\,g^{-1}$.
- 10 cycles of galvanostatic charge-discharge at $200\,mA\,g^{-1}$.
- 10 cycles of galvanostatic charge-discharge at $500\,mA\,g^{-1}$.
- 10 cycles of galvanostatic charge-discharge at $50\,mA\,g^{-1}$.

3.7.2 Cyclic voltammetry

Cyclic voltammetry was performed for the SiO_2/C-st80-8h electrode, using lithium foil as both counter and reference electrode, scanning from 0-3V at a rate of $0.3\,mV\,s$ on a Gamry Reference 600 potentiostat.

3.7.3 Full cell assemblies

The full cell assemblies constructed during this work were all cathode limited, meaning that the capacity and C-rate of the battery is defined by the by the

capacity and C-rate of the cathode material. The cells all have an anode excess capacity, with the amount varying according to cathode loading, as summarized in Table 3.3. The initial full cell experimental conditions can be found in Table 3.5. Cell voltage limits used for full cells with silicon anodes in combination with layered transition metal oxides or LFP cathodes were taken as a starting point for the full cell testing [60][62][63][64].

Table 3.5: Initial cycling conditions and cell voltage cut-off potentials for the full cell assemblies.

Cathode	Theoretical capacity [mA h g^{-1}]	C-rate at 50 mA g^{-1}	Cell voltage limits [V]
LMO	100	0.3	4.5-3.4
NMC	160	0.6	4.2-2.5
LFP/C	160	0.6	3.6-2.7

A SiO_2/C-st80-8h vs. LFP/C-st10 cell was cycled galvanostatically at 50mA g^{-1} to evaluate the initial performance of the full cells; an initial Coulombic efficiency of less than 15% was observed. It was therefore decided to investigate different strategies to increase the initial Coulombic efficiency of the full cells:

- Using a single, slow galvanostatic charge-discharge formation cycle at 10 mA g^{-1} to form a stable inert matrix and SEI.
- Using a prelithiated SiO_2/C-st80-8h anode.
- Using a prelithiated SiO_2/C-st80-8h anode and a formation cycle at 10 mA g^{-1}.

Anode prelithiation was performed by assembling a SiO_2/C-st80-8h half cell and cycling it once at a current density of 50 mA g^{-1} to allow the stabilizing matrix and SEI to form. The cycled cells were disassembled in an argon-filled glovebox, and the prelithiated anodes were assembled in full cell with a fresh-cut cathode. Additionally, one prelithiated SiO_2/C-st80-8h cell was disassembled, and the prelithiated anode was assembled in a new cell containing a fresh Li counter electrode, and cycled once at 50 mA g^{-1}.

An attempt was also made to increase the reversible capacity of the battery by decreasing the lower cut-off cell voltage, as summarized in Table 3.6. After an initial formation cycle at 10mA g^{-1} both galvanostatic cycling performance at 100mA g^{-1} and rate capability were evaluated.

Table 3.6: Cycling conditions for full cell assemblies with lower cell voltage cut-off limits.

Cathode	Theoretical capacity [mA h g^{-1}]	C-rate at 100 mA g^{-1}	Cell voltage limits [V]
LMO	100	1	4.5-1.2
NMC	160	0.6	4.2-1
LFP/C	160	0.6	3.6-0.5

4 Results

In this chapter, the results from the active material characterization and electrochemical testing will be presented. First, SEM micrographs of the diatom precursor will be displayed, followed by the results from the X-ray diffraction, thermogravimetric analysis, and nitrogen adsorption measurements. Then, galvanostatic charge-discharge curves, cyclic voltammograms and plots displaying specific capacity and Coulombic efficiency vs. cycle number will be used to illustrate the electrochemical performance of both half and full cells.

4.1 Structural characterization

4.1.1 Microstructure and morphology

The surface structure of the cleaned, organics-free diatoms is shown in Figure 4.1. The nanostructured, porous nature of the disk-like outer shell is clearly observable, displaying long-range order and pore sizes ranging from a few hundred nanometers to approximately 1 µm in diameter. The species of the diatoms is identified as coscinodiscus in the family of coscinodiscaceae, one of the largest marine diatom genera [68].

4.1.2 Crystallinity

The results from the XRD measurements are shown in Figure 4.2 and 4.3. Figure 4.2 shows the large, characteristic single feature centered at 22° of amorphous SiO_2. The absence of any crystalline phases confirms that all NaCl and KCL salts trapped in the porous structure was removed during the diatom cleaning procedure.

After the carbon coating process, the single peak at 22° remains, and the intensity at low scattering angles is increased. This indicates that the amorphous nature of the diatoms is preserved, and that the carbon coating is amorphous as well [69]. The amorphous carbon coating also contains vacancies and defects, which enhance the diffusion of Li^+ and offer reversible sites for Li^+ storage [39]. Also, there are no peaks for Si or SiC, proving that SiO_2 was not reduced during the coating process.

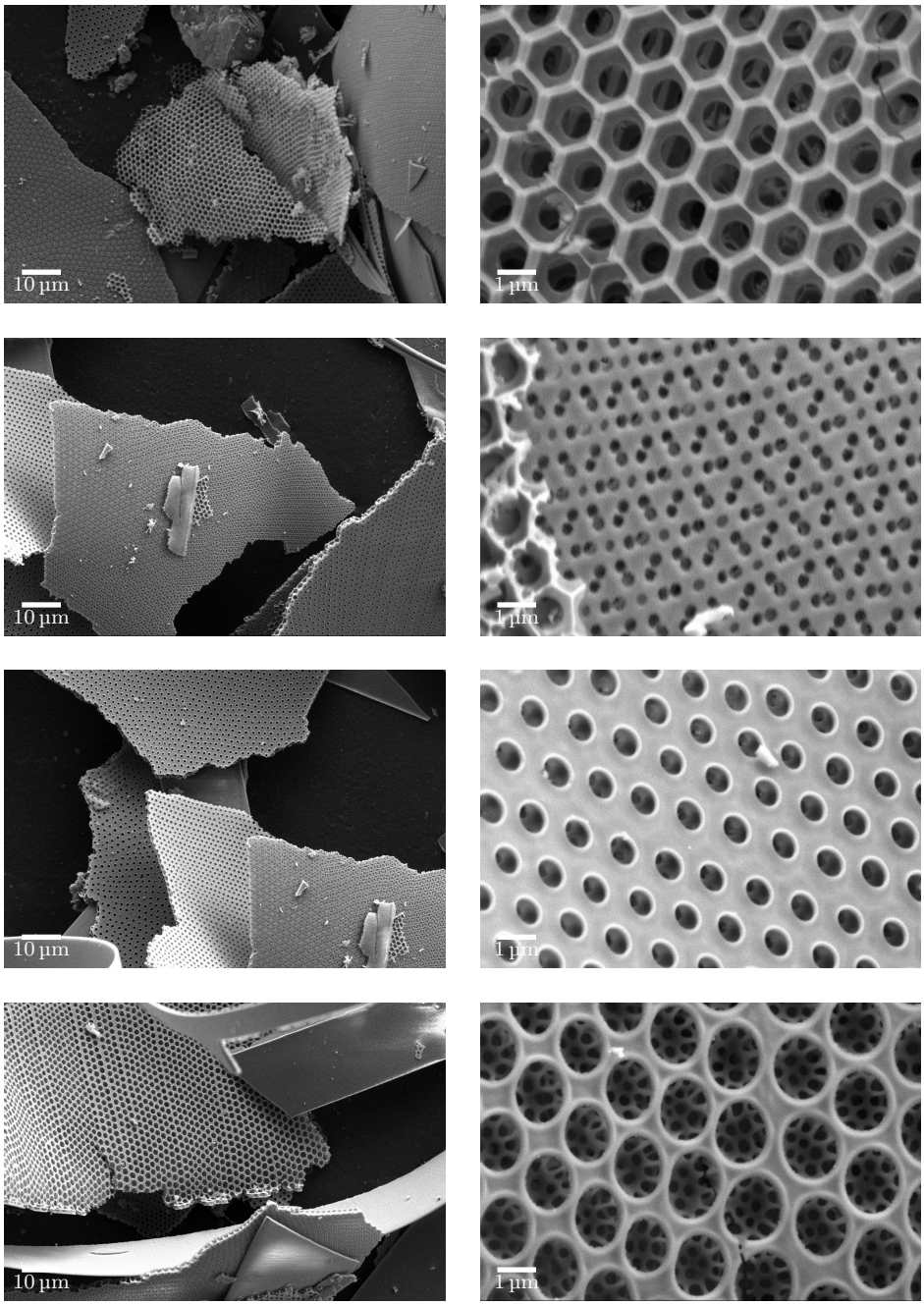

Figure 4.1: SEM micrographs of the cleaned, organics-free diatoms at low and high magnification.

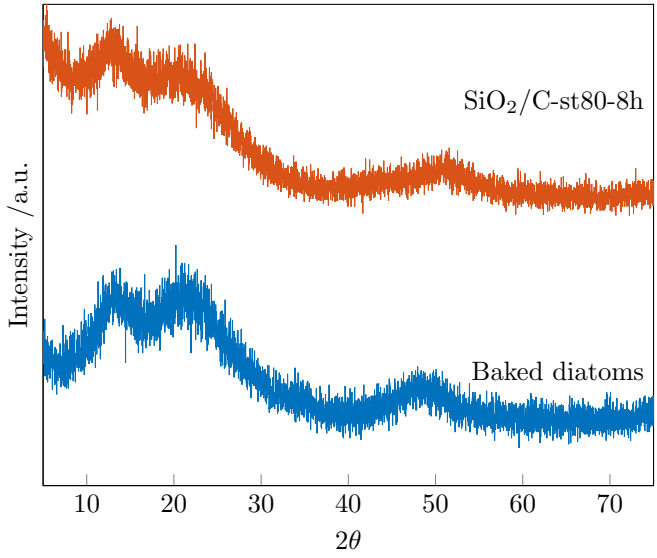

Figure 4.2: Normalized XRD diffractograms for baked, organics-free diatoms and the SiO_2/C-st80 composite.

An XRD measurement was also performed before and after carbon coating of LFP. The pre-carbonization scan agrees well with the expected pattern for $LiFePO_4$ as shown in Figure 4.3, but impurity phases were apparent, possibly lithiophosphate (Li_3PO_4) and lithium phosphate ($Li_4P_2O_7$).

After carbonization, the diffractogram retains the $LiFePO_4$ and impurity peaks. In addition, peaks corresponding to lithium iron pyrophosphate $Li_{1.875}Fe(P_2O_7)$ were discovered, but no Fe^{3+}-containing compounds were identified.

4.1.3 Thermogravimetric analysis

The results from the thermogravimetric analysis is displayed in Figure 4.4 and summarized in Table 4.1. The amount of carbon present in the sample can be estimated by assuming that the weight loss between 375 and 600 °C is due to carbon burn-off in a fixed oxygen flow rate. From Figure 4.4a, the carbon content of the SiO_2/C composites ranged from 39.2 to 49.3wt.%.

The obtained thermogravimetric curves for LFP/C-st10 and LFP/C-st25 are shown in Figure 4.4b. As for the SiO_2/C samples, it was expected to see a rapid decrease in mass from carbon burn-off from 375°C, and indeed a small drop was observed for the LFP/C-st25 samples, corresponding to 2.3wt.% carbon. However, no drop in mass was observed for the LFP/C-st10 sample, indicating that the sample contained very little, if any, carbon. At a temperature of 550°C

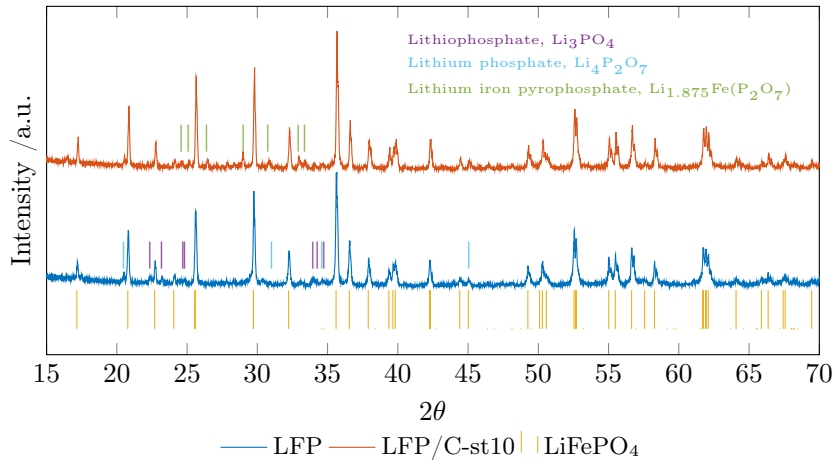

Figure 4.3: XRD diffractograms for uncoated and carbon-coated LFP/C-st10. Possible impurity phases are indicated.

Table 4.1: Carbon content of the different active materials.

Active material	Carbon content [wt.%]
SiO_2/C-st80	44.0
SiO_2/C-su80	49.3
SiO_2/C-st80-8h	39.2
LFP/C-st10	-
LFP/C-st25	2.3

the mass starts to increase rapidly. This increase was attributed to the formation of iron oxides, judging by the color change of the powder from dark grey to brownish-red [70].

4.1.4 Porosity

The results from the porosity measurements are summarized in Table 4.2. As expected, the organics-free diatoms showed similar surface area as in previous works, and no micropore area (pore width <2nm) [68]. Following the carbon coating, the specific surface area increases significantly, mostly as micropore area attributed to the amorphous carbon coating [69]. Interstingly, the external surface area of the SiO_2/C-st80, SiO_2/C-su80 and SiO_2/C-st80-8h increases as well. This implies the existence of meso- and macropores in the carbon coating (pore widht 2-50nm and >50nm, respectively). This trend is mirrored for the LFP/C-st10 and LFP/C-st25 samples.

Of the as-recieved cathodes LMO showed the highest external specific surface

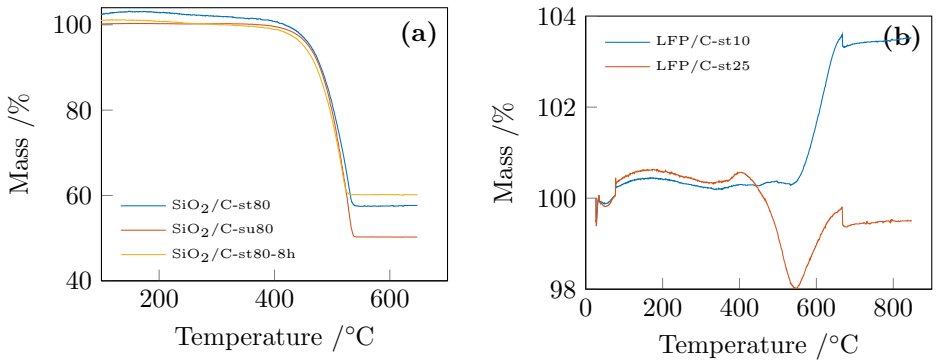

Figure 4.4: Thermogravimetric curve for the carbon coated **(a)** SiO_2/C anodes and **(b)** LFP/C cathodes at a heating rate of $10\,°C\,min^{-1}$.

area of $16.5\,m^2\,g^{-1}$. NMC also showed a moderately high specific surface area of $9.1\,m^2\,g^{-1}$, of which 15% was attributed to micropores. LFP exhibited the smallest specific surface area of the cathodes, only $1.7\,m^2\,g^{-1}$.

Table 4.2: BET surface area, t-plot micropore area and t-plot external area for the different active materials.

Material	BET specific surface area $[m^2\,g^{-1}]$	t-plot micropore area $[m^2\,g^{-1}]$	t-plot external surface area $[m^2\,g^{-1}]$
Organics-free diatoms	9.3	0	11
SiO_2/C-st80	212	173	39
SiO_2/C-su80	271	194	77
SiO_2/C-st80-8h	178	145	33
LMO	15	0	16
NMC	9.1	1.4	7.63
LFP	1.7	0	1.70
LFP/C-st10	6.0	2.5	3.6
LFP/C-st25	21	15	5.6

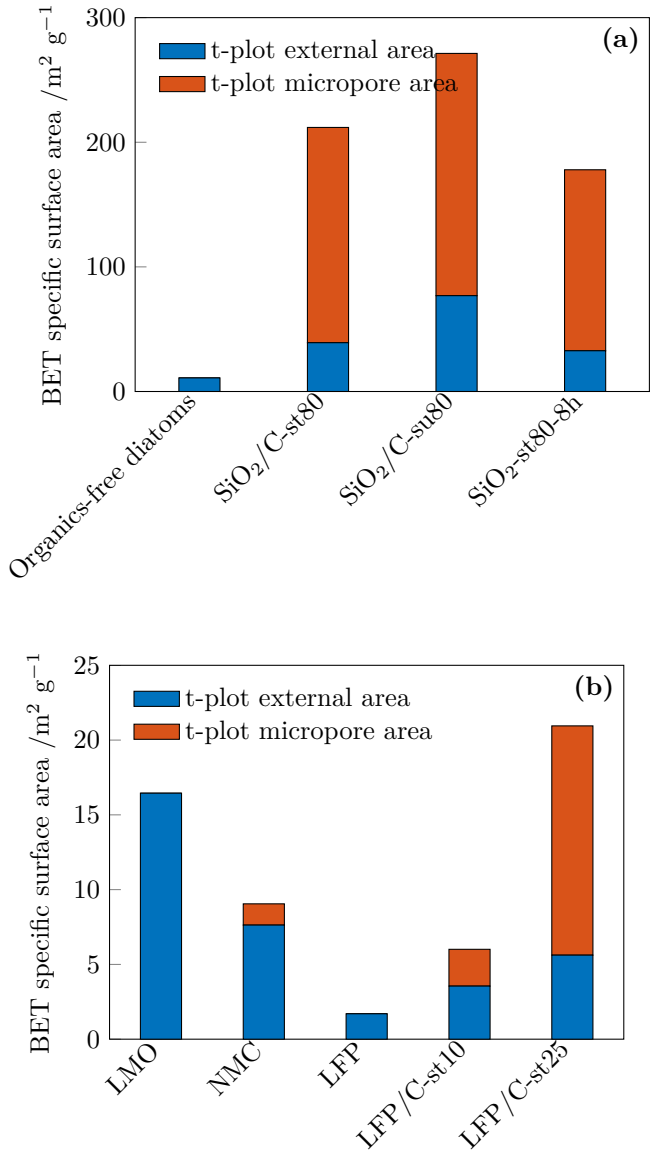

Figure 4.5: BET specific surface area, t-plot external surface area and t-plot micropore area for the **(a)** SiO_2/C anodes and **(b)** cathodes.

4.2 Electrochemical testing

This section will cover the results from the electrochemical measurements. Due to the large number of cell combinations, all the data obtained will not be presented, but enough to give a full representation of the electrochemical properties of the different materials, half cells and full cells.

4.2.1 Half cell assemblies

4.2.1.1 Galvanostatic charge-discharge

The results from the galvanostatic charge-discharge measurements for the SiO2/C anodes are shown in Figure 4.6 and Figure 4.7, with a summary provided in Table 4.3.

The galvanostatic charge-discharge curves for the SiO_2/C-st80-8h anode in Figure 4.6 show a different profile than those corresponding graphite anodes, as the curves are strongly sloping and not flat. Additionally, the first discharge curve, corresponding to initial lithiation of the SiO_2/C-st80-8h, shows a small voltage plateau between 0.75 and 0.5V, which dissappears from subsequent cycles. The following charge-discharge curves are all nearly overlapping and shift to higher capacities with cycling, indicating good reversibility of the redox reactions and increasing reversible capacity with cycling. The SiO_2/C-st80 and SiO_2/C-su80 anodes both show similar charge-discharge characteristics; dissappearing first-cycle voltage plateau, strongly sloping charge-discharge curves, and an increase in reversible specific capacity with cycling.

The long-term cycling performance of the SiO_2/C anodes is shown in Figure 4.7, and a few trends can be observed. After a high first-cycle discharge capacity an irreversible capacity loss of 60-65% is observed. The reversible charge and discharge capacity then continues to decrease over the next 10-15 cycles, before stabilizing at a specific capacity above 400mA h g^{-1}. A gradual increase in both charge and discharge capacity is observed over the next 40-80 cycles, before reaching a reversible capacity higher than the intitial charge capacity. The end of the capacity increase could not be distinguished after 100 cycles. The largest capacity increase occurred for the SiO_2/C-st80-8h anode. It is important to note that the increase in capacity can not be exploited in a full cell where the amount of cyclable lithium is limited by the amount of lithium in the cathode. Hence, the minimal reversible capacity should be taken as the reversible capacity of the anode. Further, all the anodes showed fairly good Coulombic efficiency after the second cycle, above 98% for all the anodes tested, and highest for the SiO_2/C-st80-8h anode at 98.3%.

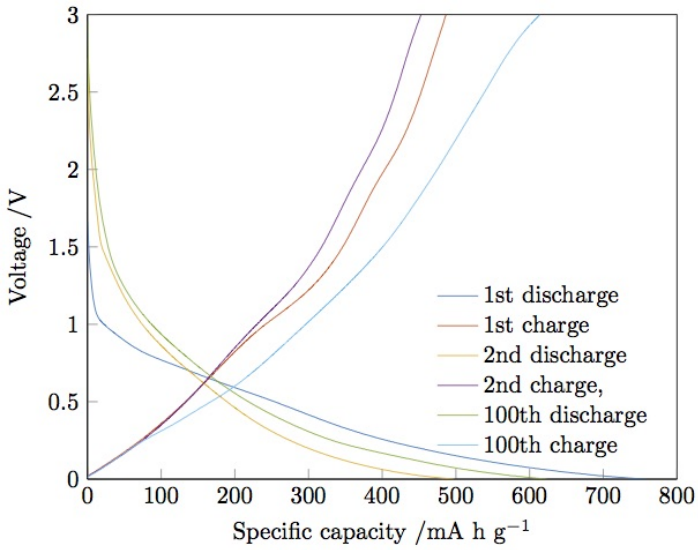

Figure 4.6: First, second and 100th cycle galvanostatic charge-discharge curves for SiO_2/C-st80-8h vs. Li.

Table 4.3: Initial discharge capacity, charge capacity, initial Coulombic efficiency, smallest reversible capacity, average Coulombic efficiency after the second cycle, and capacity retention for the SiO_2/C anodes when cycled galvanostatically at 50mA g^{-1}.

Anode	SiO_2/C-st80	SiO_2/C-su80	SiO_2/C-st80-8h
Initial discharge capacity [mA h g^{-1}]	672	896	757
Initial charge capacity [mA h g^{-1}]	437	538	487
Initial Coulombic efficiency [%]	65.1	60	64.3
Smallest reversible capacity [mA h g^{-1}]	403	480	440
Average Coulombic efficiency after the second cycle [%]	98	98.1	98.3
Capacity retention [%]	101.8	119.0	124.7

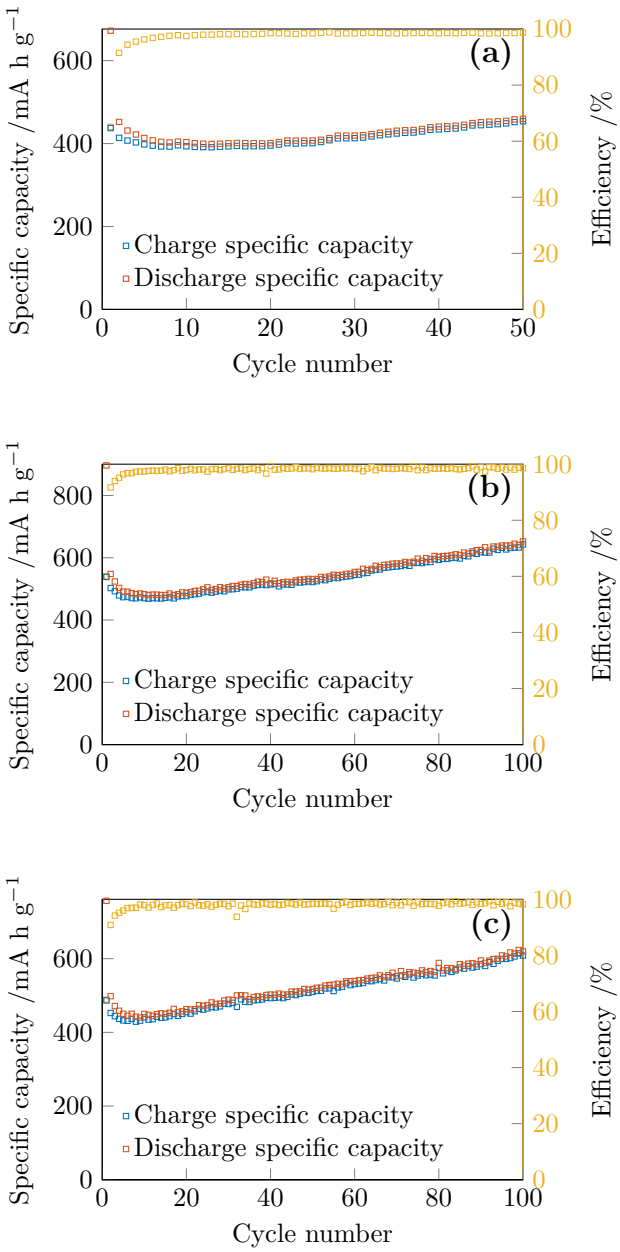

Figure 4.7: Galvanostatic charge capacity, discharge capacity and Coulombic efficiency for **(a)** SiO_2/C-st80, **(b)** SiO_2/C-su80 and **(c)** SiO_2/C-st80-8h vs. Li. All cycles were performed at a current density of 50mA g^{-1}.

The results from the galvanostatic charge-discharge measurements for the cathode materials are shown in Figure 4.8, Figure 4.9 and Figure 4.10, with a summary provided in Table 4.4.

The galvanostatic charge-discharge curves for the cathode materials are shown in Figure 4.8. The charge curve for LMO in Figure 4.8a shows a slighly sloping voltage plateau up to a specific capacity of 140mA h g^{-1} at an average potential of 4.1V, before a rapid potential increase to the final charge capacity of 150mA h g^{-1}, above the theoretical maximum specific capacity. The discharge curve has a somewhat steeper decline with an average potential of 3.9V, and a discharge capacity of 117mA h g^{-1}, giving an initial Coulumbic efficiency of 78.3%. However, with increased cycling the characteristic, gradual capacity fade of LMO is observed, and the specific capacity drops irreversibly to 100 mA h g^{-1} from the second to the 100th cycle, as shown in Figure 4.9a.

Re-examing 4.8a, it is observed that NMC shows a slightly different galvanostatic charge-discharge behaviour than LMO. Contrary to initial expectations, the first charge specific capacity of 122mA h g^{-1} was actually lower than for LMO, as was the initial discharge specific capacity of 95mA h g^{-1}. The first-cycle Coulombic efficiency was slightly lower for NMC at 77.9%, vs. 78.3% for LMO. Further, the voltage plateaus during charge and discharge are less defined, centered at approximately 3.9 and 3.8V for charge and discharge, respectively. This is attributed to the overlapping plateaus resulting from the different transition metal redox pairs. The area where NMC outperforms LMO is readily apparent when comparing Figure 4.9a and 4.9b; the capacity retention of NMC is excellent, and more than 98% of the second-cycle capacity is retained over 100 cycles.

Figure 4.8b shows the galvanostatic charge-discharge curves for the LFP/C cathodes. As expected from Gibb's phase rule and the phase-transitional lithium storage mechanism, almost horizontal voltage plateaus are observed at approximately 3.5 and 3.4V during charge and discharge, respectively. The initial charge and discharge capacities where 82 and 51mA h g^{-1}, 95 and 61mA h g^{-1} for LFP/C-st10 and LFP/C-st25 respectively, corresponding to initial Coulombic efficiencies of 62.6 and 63.7%.

The galvanostatic cycling stability of the LFP/C cathodes is shown in Figure 4.10a and Figure 4.10b. Compared to LMO and NMC, the performance is noticably poorer, especially so for LFP/C-st10. Notice in Figure 4.10a that the Coulombic efficiency of LFP/C-st10 only slowly approaches 100%, and is on average 98.5% after the second cycle. Further, the cathode showed poor capacity retention; only 83.7% of the second-cycle specific capacity was retained after 100 cycles.

In comparison, the LFP/C-st25 cathode performed somewhat better. The reversible specific capacity was increased, and a slight improvement in initial as well as average Coulombic efficiency was noted. The most improved performance metric was the capacity retention, which was 93.4% over 100 cycles referenced to the second-cycle discharge capacity.

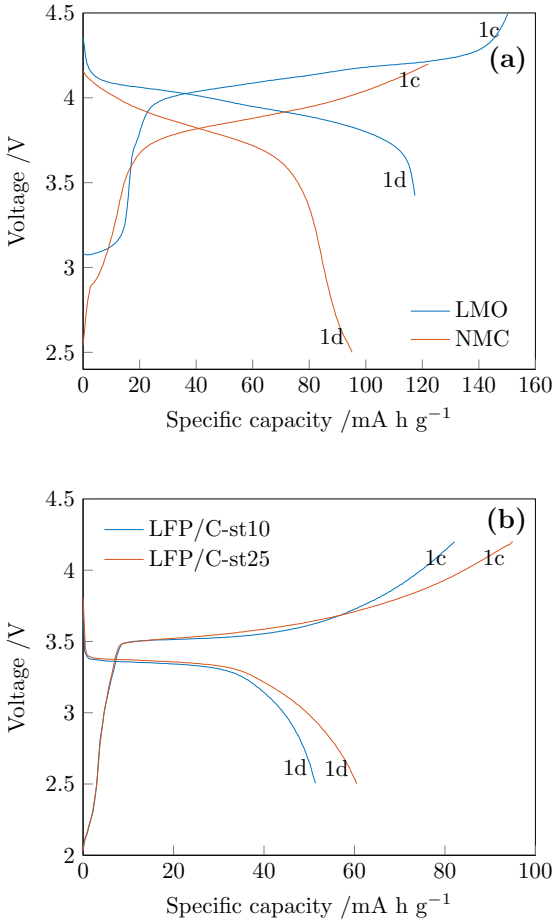

Figure 4.8: First-cycle galvanostatic charge-discharge curves for **(a)** LMO and NMC, **(b)** LFP/C-st10 and LFP/C-st25 cathodes vs. Li. 1c and 1d denotes first charge and first discharge, respectively. All cycles were performed at a current density of 50 mA h g^{-1}.

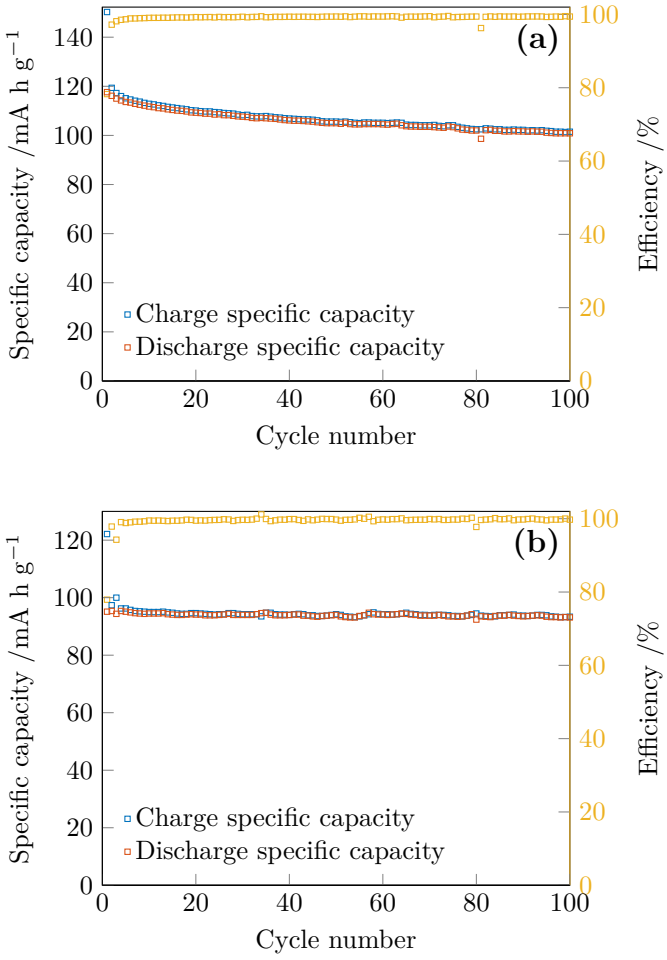

Figure 4.9: Galvanostatic charge capacity, discharge capacity and Coulombic efficiency for **(a)** LMO, **(b)** NMC cathodes at a current density of 50 mA g^{-1}.

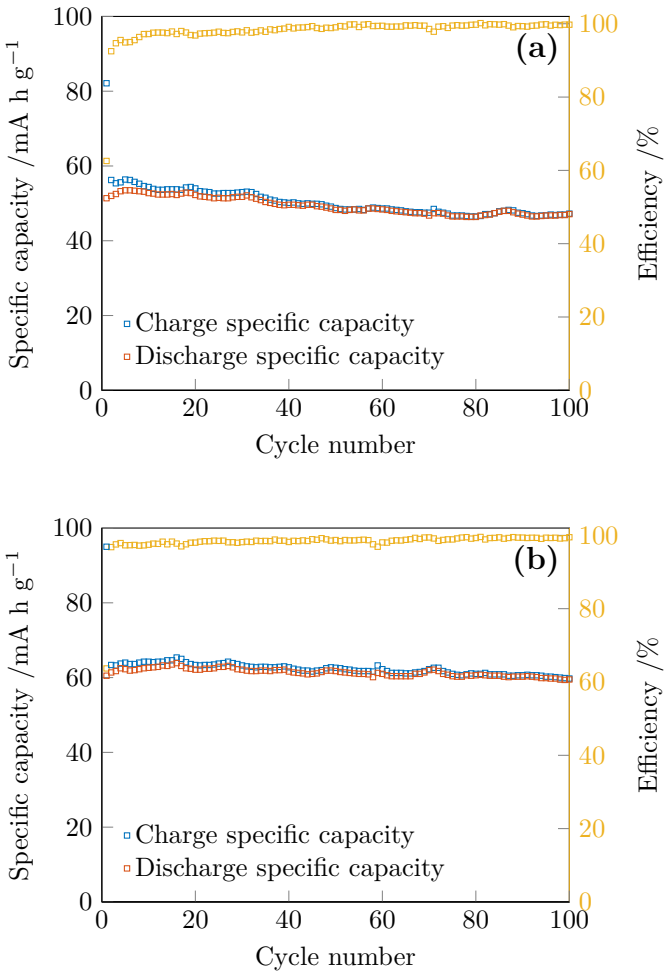

Figure 4.10: Galvanostatic charge capacity, discharge capacity and Coulombic efficiency for **(a)** LFP/C-st10, **(b)** LFP/C-st25 cathodes vs. Li at a current density of 50 mA g^{-1}.

Table 4.4: Initial charge capacity, discharge capacity, initial Coulombic efficiency, second-cycle reversible capacity, average Coulombic efficiency after the second cycle and capacity retention for the commercial cathodes when cycled galvanostatically at 50mA g^{-1}.

Cathode	LMO	NMC	LFP/C-st10	LFP/C-st25
Initial charge capacity [mA h g^{-1}]	150	122	82	95
Initial discharge capacity [mA h g^{-1}]	117	95	51	61
Initial Coulombic efficiency [%]	78.3	77.9	62.6	63.7
Second-cycle reversible capacity [mA h g^{-1}]	116	95	52	61
Average Coulombic efficiency after the second cycle [%]	99.2	99.6	98.5	98.6
Capacity retention [%]	86.9	98.2	83.7	93.4

4.2.1.2 Rate capability

The results from the rate capability measurements for the different anode materials are shown in Figure 4.11 and summarized in Table 4.5. Based on the performance of the anodes in the galvanostatic experiment, only SiO_2/C-su80 and SiO_2/C-st80-8h were evaluated.

From Figure 4.11 it is readily observable that both the SiO_2/C-su80 and SiO_2/C-st80-8h anodes show excellent rate performance, retaining 66.3 and 69.3% of the second-cycle capacity for a tenfold increase in current density, while maintaining Coulombic efficiencies well above 99% at 500mA g^{-1}, and above 99.5% in the case of SiO_2/C-st80-8h. Further, the SiO_2/C-st80-8h anode shows no clearly distinguishable drop in capacity when moving from 50 to 100mA g^{-1}. Also, the reversible specific capacity at 50mA g^{-1} is fully retained for both anodes after 50 cycles. Also, note that the capacity increases over the last 10 cycles, with the trend being more pronounced for the SiO_2/C-su80 anode.

Further, the initial charge capacity of the SiO_2/C-su80 anode dropped significantly compared to the previous measurement, while the charge capacity of the SiO_2/C-st80-8h remained approximately constant. Average Coulombic efficiency was found to be higher for the SiO_2/C-st80-8h anode.

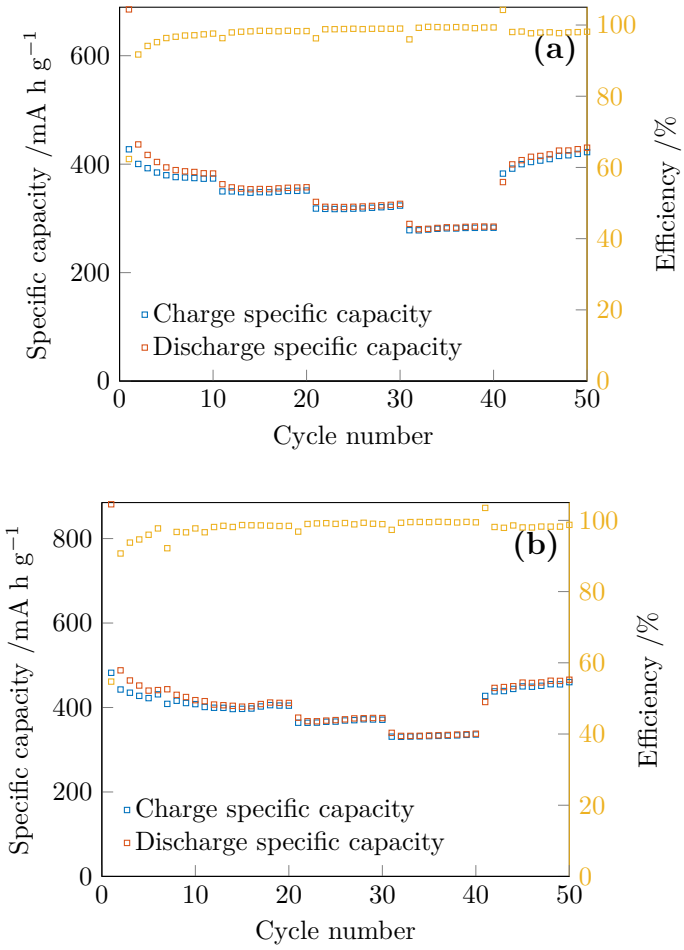

Figure 4.11: Rate capability and Coulombic efficency of **(a)** SiO_2/C-su80 and **(b)** SiO_2/C-st80-8h. Plateaus correspond to current densities of 50, 100, 200, 500 and 50 mA g^{-1}.

Table 4.5: Initial discharge capacity, charge capacity, reversible capacity at 500mA g^{-1}, percentage reversible capacity at 500mA g^{-1}, average Coulombic efficiency and capacity retention for the SiO_2/C anodes when subjected to the rate capability measurement described in Chapter 3.7.1.

Anode	SiO_2/C-su80	SiO_2/C-st80-8h
Initial discharge capacity [mA h g^{-1}]	685	881
Initial charge capacity [mA h g^{-1}]	427	482
Initial Coulombic efficiency [%]	62.4	54.2
Reversible capacity at 500mA g^{-1} [mA h g^{-1}]	283	334
Percentage reversible capacity retention at 500mA g^{-1} [%]	66.3	69.3
Average Coulombic efficiency [%]	98.0	98.1
Capacity retention [%]	100.7	96.6

The results from the rate capability measurements for the cathodes are shown in Figure 4.12 and Figure 4.13 and summarized in Table 4.6.

The rate performance of LMO is shown in Figure 4.12a, and was the worst of the cathode materials tested. A capacity drop of 67% compared to the initial value was observed for a current density of $200\,\mathrm{mA\,g^{-1}}$, and the cell showed neglgible capacity at $500\,\mathrm{mA\,g^{-1}}$, which equated to a rate of 5C. However, the average Coulombic efficiency was very high, above 99.6%, when correcting for the spikes in Coulombic efficiency at cycles 38-42, and between changes in current density. Capacity fading was observed, and the cathode retained 91.6% of it's second-cycle capacity at the end of 50 cycles.

NMC (Figure 4.12b) shows overall good rate performance; 63.3% of the second-cycle specific capacity was retained when moving from 50 to $500\,\mathrm{mA\,g^{-1}}$ corresponding to a rate of 3C. Further, the cell maintained the second-cycle capacity when the current density returned to the initial value. The Coulombic efficiency was also excellent, on average 99.1%, following the same methodology as for LMO.

By comparing Figures 4.13a and 4.13b it is noted that LFP/C-st25 posessed the highest reversible specific capacity of the LFP/C cathodes, as well as retaining most of the second-cycle specific capacity at $500\,\mathrm{mA\,g^{-1}}$; 44.6% vs. 47.0% for LFP/C-st10 and LFP/C-st25, respectively. Average Coulombic efficiency was slightly lower for the LFP/C-st25 cathode, 98.2% compared to 98.7% for LFP/C-st10. However, the capacity of LFP/C-st10 decreases to 95.6% of it's second-cycle value after 50 cycles, while the capacity of LFP/C-st25 increased by 1.6%.

4.2.1.3 Cyclic voltammetry

The obtained cyclic voltammograms for SiO_2/C-st80-8h are shown in Figure 4.14. There are several reductive peaks visible during the first cathodic scan. The first appears at a potential of 0.75V, followed by a another smaller peak at 0.41V, which both dissappear in the following cycles. Further, the strongest reduction peak appears below 0.25V and corresponds to lithiation of the SiO_2/C-st80-8h particles. The following anodic, delithiation peak is centered at approximately 0.04V, and increases in amplitude with cycling. Also, the center of the peak shifts to higher potentials from cycle to cycle. A second, wide anodic peak is observed at 1.05V, and the small cathodic counterpart appears in the second cycle at a potential of 0.75V. The curves are nearly overlapping, indicating good reversibility of the electrochemical reactions.

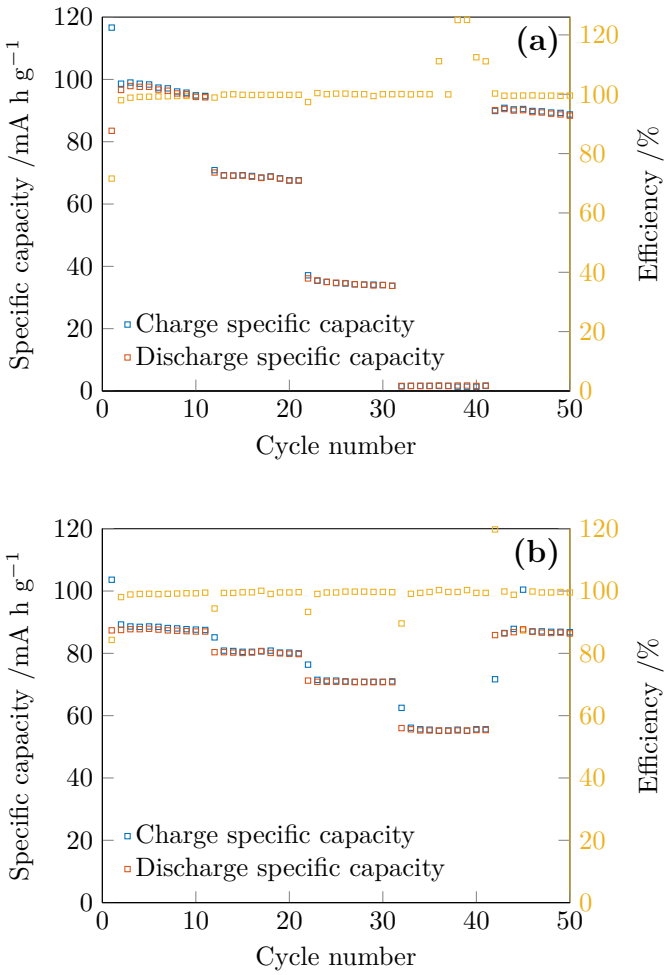

Figure 4.12: Charge-discharge capacities and Coulombic efficiency of **(a)** LMO, **(b)** NMC vs. Li at current densities and of 50, 100, 200, 500 and 50 mA g^{-1}.

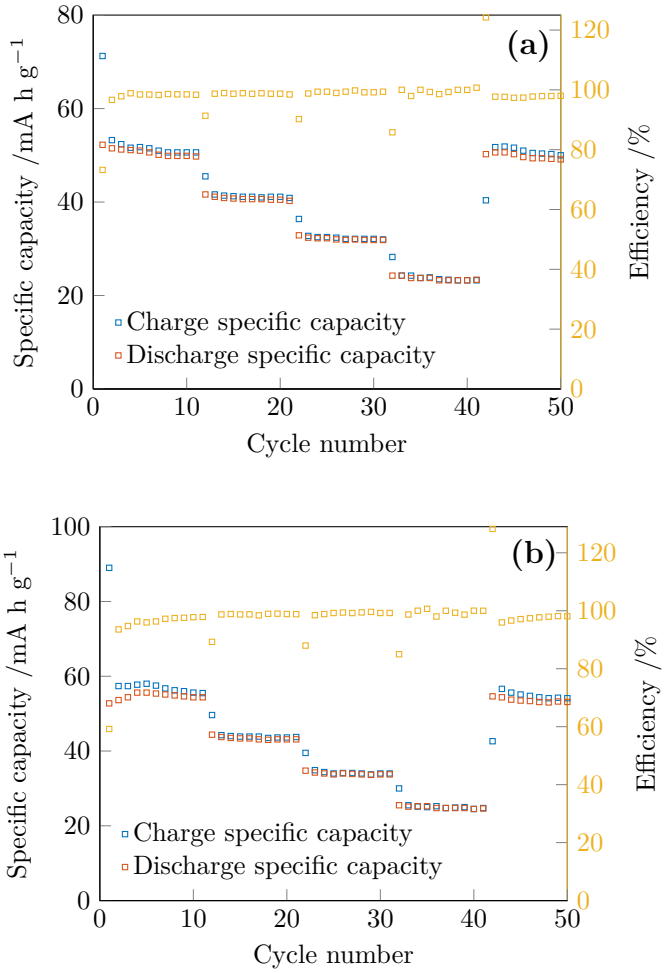

Figure 4.13: Charge-discharge capacities and Coulombic efficiency of **(a)** LFP/C-st10 and **(b)** LFP/C-st25 vs. Li at current densities and of 50, 100, 200, 500 and 50 mA g^{-1}.

Table 4.6: Initial discharge capacity, charge capacity, reversible capacity at 500mA g^{-1}, percentage reversible capacity at 500mA g^{-1}, average Coulombic efficiency and capacity retention for the commercial cathodes when subjected to the rate capability measurement described in Chapter 3.7.1.

Material	LMO	NMC	LFP/C-st10	LFP/C-st25
Initial charge capacity [mA h g^{-1}]	117	104	71	89.
Initial discharge capacity [mA h g^{-1}]	84	87	52	53
Initial Coulombic efficiency [%]	71.6	84.3	73.2	59.2
Reversible capacity at 500mA g^{-1}	1.8	55	23	25
Percentage reversible capacity retention at 500mA g^{-1} [%]	2.2	63.3	44.6	47.0
Average Coulombic efficiency [%]	99.6	99.1	98.7	98.2
Capacity retention [%]	91.6	98.9	95.6	101.6

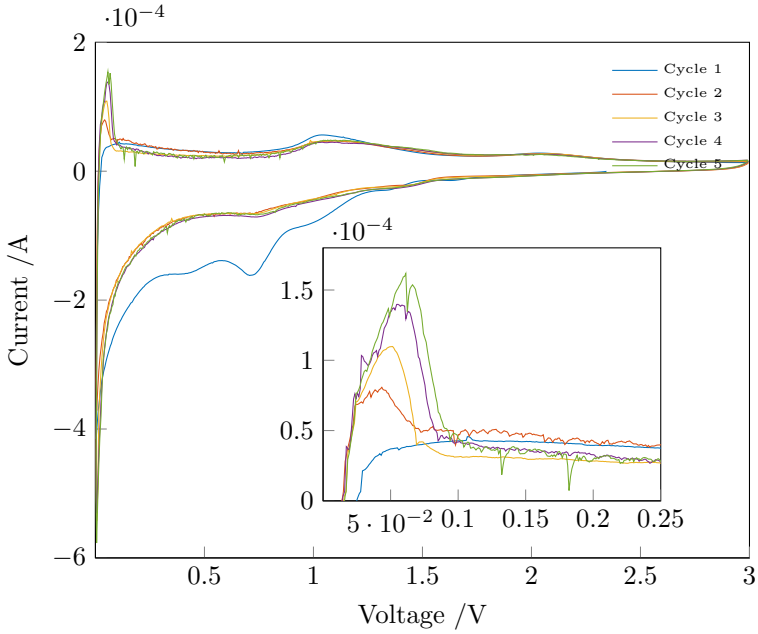

Figure 4.14: Cyclic voltammogram of SiO_2/C-st80-8h at a scan rate of 0.3 mV s .

4.2.2 Full cell assemblies

This section will cover the performance of lithium ion battery full cell assemblies with SiO_2/C anodes, investigated here for the first time, to the best of the author's knowledge.

As previously mentioned, the first LFP/C-st10 vs. SiO_2/C-st80-8h cycled at $mA\,g^{-1}$ showed an initial Coulombic efficiency of less than 15%, demonstrating that poor first-cycle Coulombic efficiency was the key limiting factor of the full cells. To mitigate this issue, the effect of a formation cycling, prelithiation and decreasing the lower cell voltage cut-off potential were investigated.

All specific capacities presented are normalized to the weight of the cathode active material to allow straight-forward comparison between the data obtained for the commercial cathodes in the previous subchapter and the full cells in the following.

The SiO_2/C-st80-8h anode was chosen for use in the full cell assemblies, as the anode showed good initial Coulombic efficiency, and the highest average Coulombic efficiency during cycling, as well as the best rate capability. The most importantly advantage however, was the ease of active material fabrication, and good capacity reproducibility. The sucrose precursor was found to yield higher capacities, but large batch-to-batch variability, as was observed for the galvanostatic and rate capability measurement for SiO_2/C-su80.

4.2.2.1 Galvanostatic charge-discharge

Formation cycling The full cells containing LMO, LFP/C-st10 and LFP/C-st25 cathodes that underwent a single formation cycle with a fresh SiO_2/C-st80-8h anode all had high initial charge capacities of 165, 73 and 76$mA\,h\,g^{-1}$ respectively, but very poor first-cycle discharge capacities, below $10\,mA\,h\,g^{-1}$. Only the NMC-containing full cell showed any significant reversible capacity; 35$mA\,h\,g^{-1}$, after an initial charge of 131.2$mA\,h\,g^{-1}$. 67% of the second-cycle capacity was retained after 200 cycles for the NMC vs. SiO_2/C-st80-8h full cell.

This result demonstrates that the formation of the inert matrix and SEI on the anode side irreversibly bound a large quantitiy of the available cyclable lithium even with the inclusion of a formation cycle, rendering the full cells practically without capacity.

Prelithiation The SiO_2/C-st80-8h anodes where prelithiated by fully lithiating and delithiating assembled coin cells, as described in Chapter 3.7.3. The re-assembled, prelithiated SiO_2/C-st80-8h anode showed no decrease in reversible capacity following the prelithiation cycle, proving that disassembling and reassembling cells effectively reduced the irreversible capacity loss for the anode, and maintained the integrity of the formed SEI.

On average, the prelithiated cells showed a first discharge specific capacity of

772 ±63mA h g^{-1}, charge specific capacity of 469±37mA h g^{-1}, and initial Coulombic efficiency of 60.7±2.8%.

The galvanostatic charge-discharge curves, galvanostatic charge-discharge specific capacities and Coulombic efficiency for the full cells with LMO and NMC cathodes are shown in Figure 4.15. It is observed that the charge curves for both cells are strongly sloping at low capacities compared to those reported for the half-cell configuration (Figure 4.8a). Two distinct voltage slopes can be seen in the charge curve for both full cells, the first and steepest slope occurs at potentials between 2.9 and 3.9V for LMO and 2.7 and 3.7V for NMC, before the charge curves flatten towards to upper cut-off potential.

Initial charge and discharge capacities were similar to those reported previously for the half-cell configurations, with initial specific charge capacity of 165 and 107mA h g^{-1} for LMO and NMC respectively. Initial discharge capacities were 38 and 55mA h g^{-1}, giving initial Coulombic efficiencies of 23.2 and 51.3%.

The discharge curve for LMO was very steep, reaching the lower cut-off cell voltage quickly, resulting in a low discharge capacity of 38mA h g^{-1} which decayed rapidly over the following 20 cycles. The capacity retention referenced to the second cycle was 43.3% after 200 cycles of galvanostatic charge-discharge at 50mA g^{-1}.

Comparatively, NMC showed better performance. Although the reversible capacity decreased quickly over the first 10 cycles, a capacity retention of 65.0% with respect to the second-cycle discharge capacity was seen after the 200 cycles were completed.

The first specific charge and discharge capacity of the LFP/C-st10 and LFP/C-st25 cathodes was 76, 11mA h g^{-1}, and 73, 17mA h g^{-1}, which was higher than for the cells cycled with a fresh anode, but negligible compared to the requirements for a commercial cell.

Prelithiation and formation cycling The performance of the full cells, with the exception of LMO, was somewhat improved after undergoing an initial formation cycle at a low current density of 10 mA g^{-1} as shown in Figure 4.16 and Figure 4.17. A summary is provided in Table 4.7.

The first-cycle charge and discharge capacity for LMO remained approximately constant compared to the full cell cycled at a constant current density, but the capacity retention referenced to the second-cycle capacity decreased slightly to 40.4%, as shown in Figure 4.16a. The average Coulombic efficiency was 98.2%.

For NMC, the first charge and discharge capacities were larger than the values obtained without an initial formation cycle, at 125 and 62mA h g^{-1}, shown in Figure 4.16b. As for the sample cycled only at 50mA g^{-1}, a rapid capacity decrease over the first ten cycles was observed, but in contrast, the capacity did not fade over the next 190 cycles, resulting in a final capacity retention of 85.4% with respect to the second cycle charge capacity. On average, the Coulombic efficiency was 99.2% over 200 cycles.

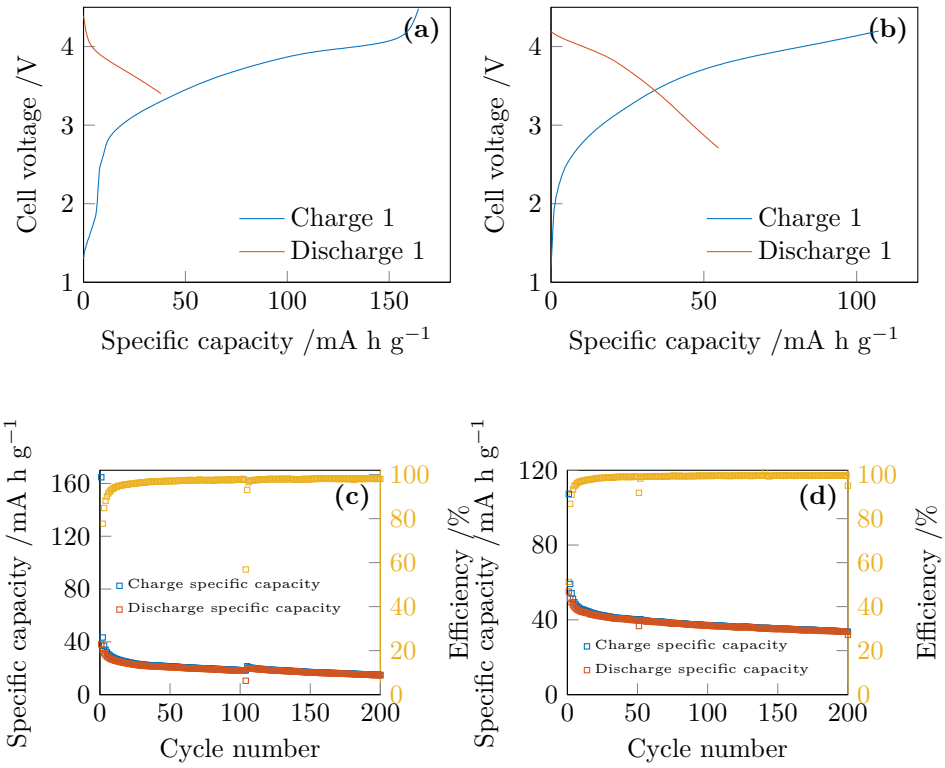

Figure 4.15: Galvanostatic charge-discharge curves for full cells with a prelithiated SiO_2/C-st80-8h anode and **(a)** LMO, **(b)** NMC cathode. Corresponding galvanostatic charge-discharge capacities are shown in **(c)** and **(d)**, for LMO and NMC respectively. All cycles were performed at 50mA g^{-1}.

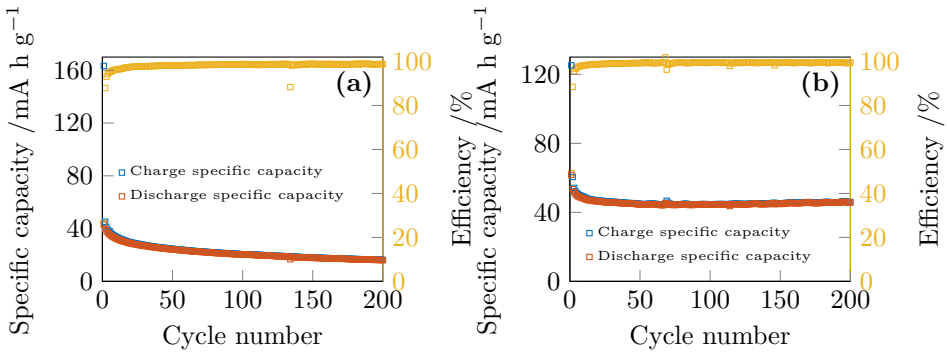

Figure 4.16: Galvanostatic charge-discharge capacities and Coulombic efficiency for full cells containing a prelithiated SiO_2/C-st80-8h anode and **(a)** LMO, **(b)** NMC cathodes. The first cycle was performed at a current density of $10\,mA\,g^{-1}$, all subsequent cycles at $50\,mA\,g^{-1}$.

The greatest improvement compared to the prelithiation-only approach was observed for the full cells containing LFP/C cathodes. The first-cycle galvanostatic charge-discharge curve for LFP/C-st10 in Figure 4.17a shows a high initial charge capacity of $125 mA\,h\,g^{-1}$ and discharge capacity of $34 mA\,h\,g^{-1}$ at the lower cell voltage cutoff. The capacity retention of the LFP/C-st10 cathode was 77% compared to the second-cycle discharge capacity, and the Coulombic efficiency was on average 98.6%.

The LFP/C-st25 vs. SiO_2/C-st80-8h full cell exhibited an initial specific charge capacity of $88 mA\,h\,g^{-1}$ and a specific discharge capacity of $21 mA\,h\,g^{-1}$, which dropped to $15.8 mA\,h\,g^{-1}$ in the following cycle. However, good capacity retention was observed; 92.4% of the second-cycle discharge capacity was still available after 200 cycles, owed to the high average Coulombic efficiency of 99.5%.

The overall shape of the charge-discharge curves for the LFP/C full cells in Figure 4.17a and Figure 4.17b are different compared to the LFP/C vs. Li half-cell configuration in Figure 4.8b. Most notably, the rapidly increasing voltage and flat voltage plateau characteristic for the LFP/C vs. Li half cell was replaced with an almost linear increase in cell voltage with increasing capacity. The discharge curves were also linear in shape, reaching the lower cut-off voltage quickly.

The charge curve in Figure 4.17a and discharge curve in 4.17a both contain an asymptotic break in the curve due to interruption in the power supply to the Lanhe battery testing stations.

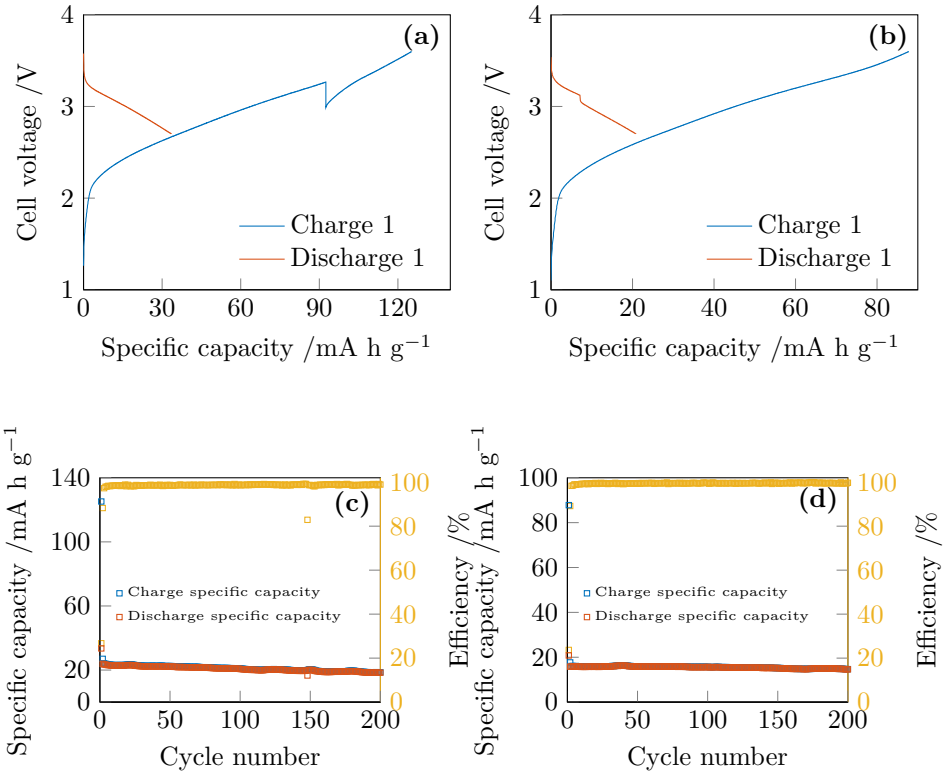

Figure 4.17: Galvanostatic charge-discharge curves for full cells with a prelithiated SiO_2/C-st80-8h anode and **(a)** LFP/C-st10, **(b)** LFP/C-st25 cathode. Corresponding galvanostatic charge-discharge capacities and Coulombic efficiency is shown in **(c)** and **(d)** for LFP/C-st10 and LFP/C-st25, respectively. The first cycle was carried out at 10mA g^{-1}. All subsequent cycles were performed at 50mA g^{-1}.

Table 4.7: Initial charge capacity, discharge capacity, initial Coulombic efficiency, stable reversible capacity (10th cycle), average Coulombic efficiency and capacity retention for full cells containing SiO_2/C-st80-8h prelithiated anodes and LMO, NMC, LFP/C-st10 and LFP/C-st20. All cells underwent a single formation cycle at 10mA g^{-1} before cycling at 50mA g^{-1}.

Cathode	LMO	NMC	LFP/C-st10	LFP/C-st25
Initial charge capacity [mA h g^{-1}]	163	125	125	87
Initial discharge capacity [mA h g^{-1}]	43	62	34	21
Initial Coloumbic efficiency [mA h g^{-1}]	26.5	49.3	26.8	23.7
10th cycle capacity [mA h g^{-1}]	32	48	23	16
Average Coulombic efficiency [%]	98.2	99.2	98.6	99.5
Capacity retention [%]	40.4	85.4	77.0	92.4

Decreasing the lower cell voltage cut-off potential The results for the cells cycled with a decreased lower cell voltage cut-off potential according to the conditions specified in Table 3.6, are shown in Figures 4.18-4.21 and summarized in Tables 4.8 and 4.9.

The galvanostatic charge-discharge curves for the full cells with decreased cell voltage cut-off potential are shown in Figures 4.18 and 4.19. As expected, the charge curves for all the cathodes are similar in shape to those reported previously, showing the same two-slope behaviour for the LMO and NMC vs. SiO_2/C-st80-8h full cells, and almost linear shape for LFP/C full cells. First-cycle charge capacities were 155, 118, 89 and 94mA h g^{-1} for LMO, NMC, LFP/C-st10 and LFP/C-st25-containing full cells, respectively. The discharge curves however are very different, extending to much higher capacities due to the lowered cut-off potential.

The galvanostatic discharge curve for the LMO full cell, shown in Figure 4.18a, also display two slopes during discharge. The first voltage slope is observed for potentials between 4 and 2.7V, and the second from 2.7V to the cut-off cell voltage at 1.2V, resulting in an average discharge voltage of 3.01V. The corresponding values for the NMC vs. SiO_2/C-st80-8h full cell (Figure 4.18b) are 4.2-2.6V and 2.6-1V for the first and second voltage slopes respectively. The average discharge voltage was found to be 2.94V.

The jump in the LMO discharge curve occurred due to interruption in the power supply to the Lanhe battery tester, causing the potential of the battery to increase spontaneously when no current was drawn.

Displayed in Figure 4.19 are the galvanostatic charge-discharge curves for the LFP/C vs. SiO_2/C-st80-8h full cells. As for the LMO and NMC full cells, a two-slope behaviour was observed for the discharge curves at potentials of 3.2-2V and 2-0.5V for both LFP/C cathodes. The average discharge voltage of the full cells was 2.26V and 2.27V for LFP/C-st10 and LFP/C-st25 respectively.

As a direct consequence of the reduced lower cell voltage cut-off potential, the intial Coulombic efficiency improved drastically, proving that the poor initial Coulombic efficiency obtained previously was largely due to under-discharge of the batteries. First-cycle Coulombic efficiency was above 74% for LMO and NMC, while the LFP/C-st10 and LFP/C-st25 vs. SiO_2/C-st80-8h full cells exhibited initial Coulombic efficiencies of 84.2 and 80.6% respectively.

However, the reversible capacity dropped further for all the full cells when the current density was increased to 100mA g^{-1}, and continued to decrease rapidly before stabilizing somewhat after approximately ten cycles for the LMO and NMC-containing full cells, and after two cycles for the LFP/C-contaning full cells. Overall, the capacity retention after 200 cycles for the LMO-containing full cell was 48.0%, vs. 59.8% for the NMC-containing full cell. The capacity retention of the LFP/C-st10 and LFP/C-st25 vs. SiO_2/C-st80-8h full cells was 74.2 and 77.5%, respectively . Although capacity fading was observed, average Coulombic efficiency remained high, above 99%, for LMO, NMC and LFP/C-st10. The LFP/C-st25 vs. SiO_2/C-st80-8h cell had a poor average Coulombic efficiency of 95.5%, despite the best capacity retention of all the full cells cycled to a lower cell voltage cut-off.

Table 4.8: Initial charge capacity, discharge capacity, intial Coulombic efficiency, stable reversible capacity (10th cycle), average Coulombic efficiency and capacity retention for full cells containing SiO_2/C-st80-8h pre-lithiated anodes and LMO, NMC, LFP/C-st10 and LFP/C-st20. All cells underwent a single formation cycle at 10mA g^{-1} before cycling at 100mA g^{-1} at the conditions specified in Table 3.6.

Cathode	LMO	NMC	LFP/C-st10	LFP/C-st25
Initial charge capacity [mA h g^{-1}]	155	118	89	94
Initial discharge capacity [mA h g^{-1}]	115	88	75	76
Initial Coloumbic efficiency [mA h g^{-1}]	74.2	75.0	84.2	80.6
10th cycle capacity [mA h g^{-1}]	82	65	41	44
Average Coulombic efficiency [%]	99.1	99.2	99.7	95.5
Capacity retention [%]	48.0	59.8	74.2	77.5

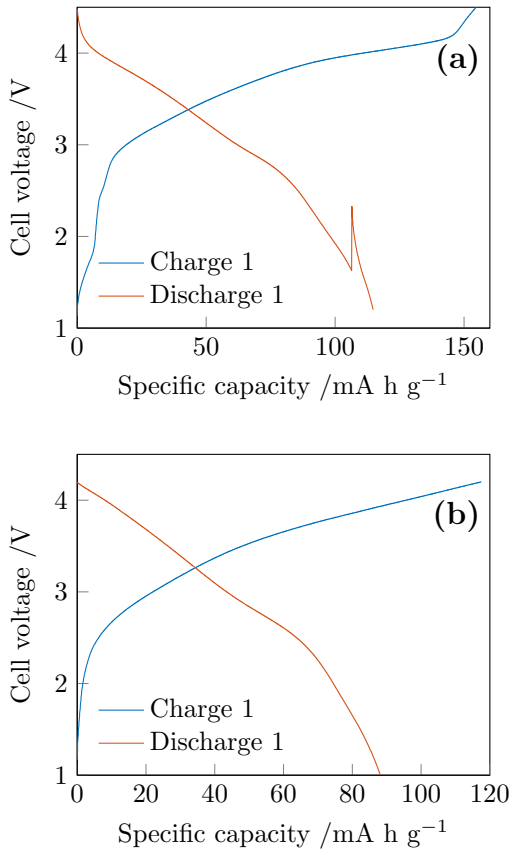

Figure 4.18: First-cycle galvanostatic charge-discharge curves for the full cells containing prelithiated SIO_2/C-st80-8h anodes and **(a)** LMO, **(b)** NMC cathodes.

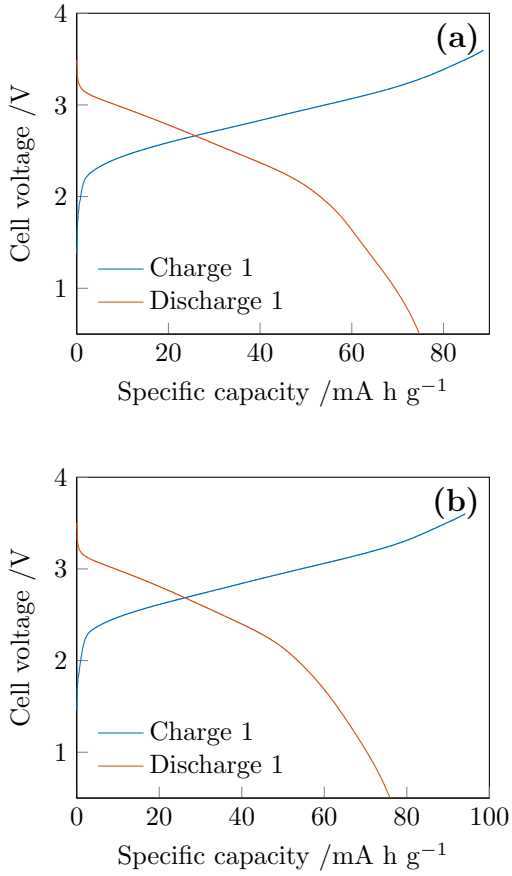

Figure 4.19: First-cycle galvanostatic charge-discharge curves for full cells containing prelithiated SIO_2/C-st80-8h anodes and **(a)** LFP/C-st10, **(b)** LFP/C-st25 cathodes.

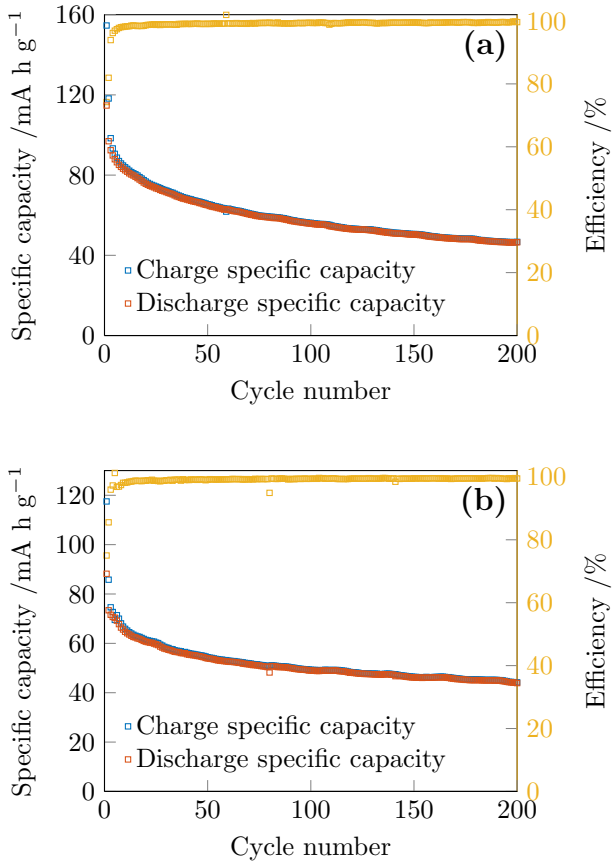

Figure 4.20: Galvanostatic charge-discharge capacities and Coulombic efficiency for full cells with prelithiated SiO_2/C-st80-8h anodes and a **(a)** LMO, **(b)** NMC cathode. The first cycle was carried out at 10mA g^{-1}, and all subsequent cycles at 100mA g^{-1}.

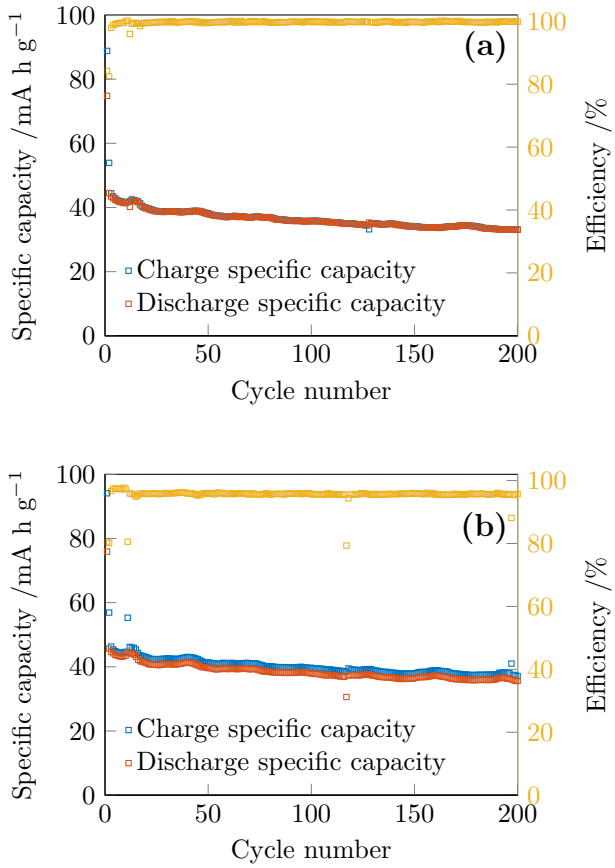

Figure 4.21: Galvanostatic charge-discharge capacities and Coulombic efficiency for full cells with a prelithiated SiO_2/C-st80-8h anode and a **(a)** LFP/C-st10, **(b)** LFP/C-st25 cathode. The first cycle was carried out at 10mA g^{-1}, and all subsequent cycles at 100mA g^{-1}.

Table 4.9: Operating voltage for the full cells with a prelithiated SiO_2/C-st80-8h anode and LMO, NMC, LFP/C-st10 and LFP/C-st25 cathode.

Cathode	Operating voltage [V]
LMO	3.01
NMC	2.94
LFP/C-st10	2.26
LFP/C-st25	2.27

4.2.2.2 Rate capability

The rate capability of full cells containing LMO, NMC and LFP/C-st25 vs. SiO_2/C-st80-8h cycled to the lower cell voltage cut-off limit was evaluated. The results are shown in Figure 4.22 and summarized in Table 4.10.

All the full cells showed lower initial charge and discharge capacities after the slow galvanostatic formation cycle compared to the galvanostatic charge-discharge cycling at 100mA g^{-1}, but similar initial Coulombic efficiency. Reversible capacity at the tenth cycle was therefore reduced for both LMO and LFP/C-st25, but slightly higher for the NMC-containing full cell.

Compared to the results from the rate capability measurement for the LMO half cell (4.12a) the full cell showed a drastically improved response to increased current density, retaining 54.5% of the second cycle capacity at a current density of 500mA g^{-1}, compared to only 2% for the half cell configuration. High Coulombic efficiency, on average 98.2%, was maintained throughout, but the final capacity retention was only 66.9%.

The NMC-containing full cell also performed well at elevated current densities, showing a capacity retention at 500mA g^{-1} of 61.2%, which is only slightly lower than for the half-cell measurment. Coulombic efficiency was also high, 98.5% on average, contributing to a capacity retention of 73.8% after 50 cycles, compared to the second-cycle discharge capacity.

The full cell with a LFP/C-st25 cathode had the lowest capacity retention at a current density at 500mA g^{-1} at 48%, which was slightly better than the for the half cell configuration. Both the average Coulombic efficiency and capacity retention, 99.3 and 87.1%, respectively, was higher than for the LMO and NMC-containing full cells.

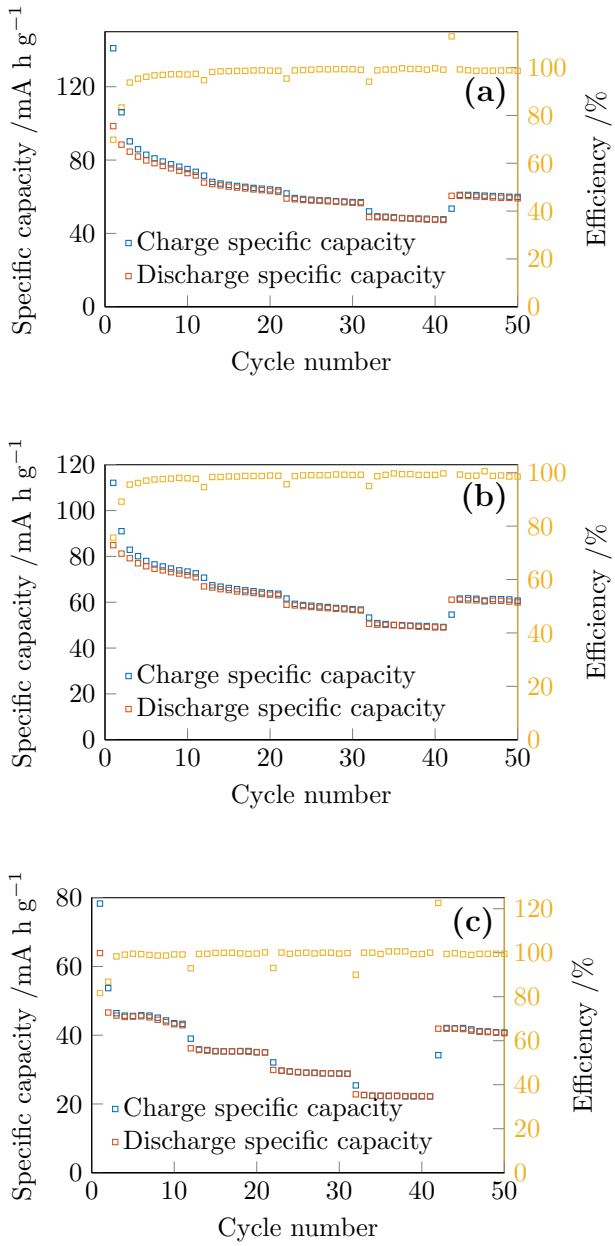

Figure 4.22: Rate performance of the full cells with a prelithiated SiO_2/C-st80-8h anode and **(a)** LMO, **(b)** NMC, **(c)** LFP/C-st25 cathode. The first cycle was performed at a current density of 10mA g^{-1}, plateaus correspond to current densities of 50, 100, 200, 500 and 50mA g^{-1}.

Table 4.10: Initial discharge capacity, charge capacity, initial Coulombic efficiency, reversible capacity at the tenth cycle, reversible capacity at 500mA g^{-1}, percentage reversible capacity retention at 500mA g^{-1}, average Coulombic efficiency and capacity retention for the full cells with a prelithiated SiO_2/C-st80-8h anode and a LMO, NMC, or LFP/C-st25 cathode when subjected to the rate capability measurement described in Chapter 3.7.1. The first cycle was performed at a current density of 10mA g^{-1}.

Material	LMO	NMC	LFP/C-st25
Initial charge capacity [mA h g^{-1}]	141	112	78
Initial discharge capacity [mA h g^{-1}]	98	85	64
Initial Coulombic efficiency [%]	69.9	75.7	81.7
Reversible capacity, 10th cycle [mA h g^{-1}]	74	72	43
Reversible capacity at 500mA g^{-1} [mA h g^{-1}]	48	50	22
Percentage reversible capacity retention at 500mA g^{-1} [%]	54.5	61.2	48.1
Average Coulombic efficiency [%]	98.2	98.5	99.3
Capacity retention [%]	66.9	73.8	87.1

5 Discussion

In this chapter, the results will be discussed in the same order as presented in Chapter 4. The results from active material characterization and the electrochemical testing of the half-cell assemblies and will be used to discuss the performance of the full-cell batteries, before the feasibility of using the constructed batteries as the basis of a large-scale energy storage system for the WIN WIN project is discussed.

It is important to keep in mind that the cathodes employed in this work were all commercially sourced and are expected to show excellent cycling stability as well as rate capability. Again, it should be emphasized this is the first published work to date on silica anodes in lithium ion battery full cells.

5.1 Structural characterization

The SEM micrographs in Figure 4.1 reveal the highly porous nature of the outer shell of the diatoms, and the XRD measurement confirms they consist of amorphous silica without crystalline phases, demonstrating the succesful removal of NaCl and KCl during the cleaning procedure, as well as the absence of reduced species such as Si or SiC which might have formed during the heat treatment. From the nitrogen adsorption measurements, the specific surface area was found to be $9.3\,m^2\,g^{-1}$, with no micropore area.

Further, the particles were succesfully coated with an amorphous carbon coating using both starch and sucrose as carbon-containing precursors. The thermogravimetric analysis confirmed that the SiO_2/C-st80, SiO_2/C-su80 and SiO_2/C-st80-8h anodes contained 44, 49.3 and 39.2 wt.% carbon respectively, even though the initial weight ratio of diatoms to carbon precursor was identical. The sucrose precursor resulted in the highest amount of carbon, and longer calcination times decreased the carbon content for the cornstarch precursor. The carbon content of the LFP/C cathodes was also determined by TGA. Little to no carbon was detected for the LFP/C-st10, although the increase in specific surface area measured by BET indicates that some carbon must be present. On the other hand, the LFP/C-st25 active material contained 2.3wt.% C, which is in the lower end of the spectrum of carbon contents reported in literature [71][72]. The rapid increase in mass for the LFP/C was attributed to the oxidation of iron to give Fe_2O_3, judging by the reddish-brown colour.

The carbon coating resulted in a large increase in BET specific surface area, most of which consisted of micropore area from the amorphous carbon coating

[69]. The presence of micropores is predicted to have little to no impact on battery performance, as the micropores are smaller than the radius of solvated $Li(EC)_{2/3^+}$, and will therefore participate only to a very small extent in SEI formation and lithium intercalation/deintercalatation processes [73]. Meso- and macropores on the other hand can readily accomodate solvated Li^+, allow transport of lithium ions to the surface of the SiO_2 diatom shell, and SEI to be formed over the surface area of the pore.

In order to verify that the LFP cathode remained phase pure after carbon-coating an XRD scan before and after the carbonization was carried out. The as-recieved powder was not phase-pure and contained small impurity peaks, possibly lithiophosphate (Li_3PO_4) and lithium phosphate ($Li_4P_2O_7$). After carbon coating, peaks corresponding to lithium iron pyrophosphate ($Li_{1.875}Fe(P_2O_7)$) were discovered. Impurity phases in LFP are known to be detrimental to cathode performance, as the one-dimensional lithium intercalation and deintercalation pathways can be blocked by iron atoms occupying lithium sites. However, all the impurity phases discovered in the XRD diffractogram are known to be permeable to lithium when present on particle surfaces [74]. Most importantly, no Fe^{3+} containing impurities were discovered, as phases with Fe^{3+} tend to block the 1D channels of the $LiFePO_4$ crystal structure, hindering lithium diffusion and movement of the $LiFePO_4/FePO_4$ phase boundary [20].

5.2 Electrochemical performance

5.2.1 SiO_2/C half cells

The obtained charge-discharge curves for all the SiO_2/C anodes are in good agreement with those reported in literature. Present in all the charge-discharge curves is a voltage plateau centered at 0.75V during the first discharge, which dissappears in following cycles. This plateau can be explained by examining the cyclic voltammogram in Figure 4.14, where a reductive peak is present at the same potential, which also dissapears in the next cycle. This peak is associated with the irreversible decomposition of the EC component in the electrolyte to form the SEI [50]. Similarly, the slope between 0.35 and 0V of the galvanostatic charge-discharge curve in Figure 4.6 corresponds to the strong reductive peak in the cyclic voltammogram, associated with the irreversible formation of the inert Li_2O and Li_4SiO_4 matrix, as well as the reversible alloying reaction between lithium ions and silicon [39]. Further, the wide anodic peak at 1.05V in the cyclic voltammogram has a corresponding change in slope for the first charge curve in Figure 4.6. This peak is thought to corresponds to the reversible conversion reaction between SiO_2 and $Li_2Si_2O_5$ (Reaction 2.6) [68].

The anode material prepared with the sucrose precursor, SiO_2/C-su80, showed the highest initial discharge and charge capacity of all the SiO_2/C active materials in the galvanostatic cycling measurement, at 896 and 538mA g^{-1} respectively,

at a current density of 50mA g^{-1}. The SiO_2/C-st80 showed the smallest initial discharge and charge capacity of 672 and 437mA g^{-1}. High capacity was also achieved for the SiO_2/C-st80-8h, but not as high as for the sample using sucrose as the carbon precursor, at 757 and 487mA h g^{-1} for discharge and charge respectively. The reversible capacities of the anodes were not among the highest reported in literature, *cf.* Table 2.4, but comparable to similar reported morphologies.

Interestingly, the obtained reversible discharge and charge capacities did not follow any specific trend with respect to carbon content, with the exception that the highest reversible capacity was obtained for the highest carbon content. Judging by carbon content alone, the SiO_2/C-st80 active material containing 44.0wt.% C should outperform the SiO_2/C-st80-8h, which contained 39.2wt.% C. As this did not occur, the effect of increased calcination time had a larger effect on anode performance than the absolute amount of carbon. One possible explanation is that the longer heat-treatment time gave rise to a denser, more homogeneous coating with higher degree of graphitization, and consequently, higher electronic conductivity [23]. This is further supported by the high capacity of SiO_2/C-st80-8h compared to SiO_2/C-su80, which differ more then 10wt.% in carbon content, but only ∼40mA h g^{-1} in reversible capacity.

The initial Coulombic efficiency of the anodes tested were in the higher range of those reported in literature, ranging from 60-65% in the galvanostatic charge-discharge measurement. The corresponding irreversible capacity loss of 35-40% is partly attributed to the formation of a stabilizing, inert matrix of Li_2O and Li_4SiO_4, embedding the formed Si-phase and contributing to the resulting stable cycling performance of the SiO_2/C anodes apparent in Figure 4.7. As the magnitude of the capacity loss is small, it can be assumed that a higher fraction of Li_2O compared to Li_4SiO_4 is formed. Further, the irreversible capacity loss also has a contribution from SEI formation, implying a relationship between surface area and the observed capacity loss. This trend was noted for the SiO_2/C half cells cycled at 50mA g^{-1}, that is, the lowest inititial Coulombic efficiency of 60% was observed for the sample with the highest surface area, namely SiO_2/C-su80. Both samples with cornstach precursor showed a similar initial Coulombic efficiency of 64.3% and 65.1% for SiO_2/C-st80-8h and SiO_2/C-st80 respectively.

Common for all the SiO_2/C anodes was excellent cycling stability, and high average Coulombic efficiency during cycling, above 98% for all anodes tested, and highest for SiO_2/C-st80-8h at 98.3%. Again, no clear trend with regard to carbon content could be observed. A very slight improvement in Coulombic efficiency was noted for the increased carbon content of SiO_2/C-su80, and for the prolonged heat-treatment time in the case of SiO_2/C-st80-8h. A possible explanation is that the Coulombic efficiency is enhanced by an increase in electronic conductivity, manifested as a larger fraction of conductive material in the case of SiO_2/C-su80, and a denser, more homogeneous coating with improved conductivity due to higher degree of graphitization, as a result of prolonged heat-treatment time for SiO_2/C-st80-8h [23]. The latter hypothesis is supported by good performance despite the lower carbon content and the smaller micropore and external surface

area normalized to carbon content. Increased electronic conductivity is know to improve the kinetics of the alloying and dealloying reactions, and thereby Coulombic efficiency during cycling and performance at high current density [23].

Another common trend for the SiO_2/C anodes is an increase in capacity over the first 100 cycles. This capacity increase is thought to arise from the growth of the silicon phase. The capacity gain by inclusion of new Si atoms outweighs the capacity loss due to consumption of SiO_2 to form the irreversible Li_2O and Li_4SiO_4 inert matrix. This is supported by the heightening and narrowing of the deallying peak in the cyclic voltammogram in Figure 4.14, which suggests that more lithium is available to dealloy in subsequent cycles [45]. An alternative explanation has been offered by Tu *et al.*; the capacity increases as a result of an activation and stabilization mechanism during cycling [49]. It is important to note that although the capacity increases over time, the increase can not be exploited in a full cell, as the amount of cyclable lithium is limited by the lithium available from the cathode. However, it is indicative of good long-term cycling performance for the SiO_2/C anodes, as the capacity is less likely to decrease over time.

However, all the SiO_2/C anodes showed a significant decrease in reversible capacity between the second and tenth cycle; progressively less lithium could be accomodated by the anode, before the capacity stabilized and started to increase, possibly due to growth of the Si phase. The observed capacity loss can have several contributions. First, the stabilizing matrix of Li_2O and Li_4SiO_4 may not be fully formed after the first cycle, which means that some of the lithium will be irreversibly bound in the following cycles. However, by examining the cyclic voltammogram, this doesn't appear to be the case, as the strong reducive peak below 0.25V vs. Li/Li^+ remains unchanged after the initial cycle. Second, the volume change during the initial lithiation and following delithiation may cause some of the particles to lose contact with the conductive carbon black additivie or the current collector, and are thus unavailable to transfer electrons, and consequently lithium ions in the following cycles. Third, the volume change may also lead to crack formation during the initial alloying, which propagate under the tensile stress following delithiation, exposing new, unpassivated surface area, resulting in electrolyte decomposition and continuous formation of new SEI.

The SiO_2/C-su80 and SiO_2/C-st80-8h active materials were also investigated for rate capability, as summarized in Table 4.5. Due to the relatively low capacity of SiO_2/C-st80, compared to SiO_2/C-su80 and SiO_2/C-st80-8h it was decided not to investigate the rate capability of this material.

Evident from Figure 4.11a and Figure 4.11b was the excellent rate performance of both SiO_2/C-su80 and SiO_2/C-st80-8h, showing a fully reversible capacity retention of 66.3 and 69.3% for a tenfold increase in current density. The SiO_2/C-st80-8h also showed an almost indiscernible drop in capacity when moving from a current density of $50 mA\,g^{-1}$ to $100 mA\,g^{-1}$. Both anodes also maintained high Coulombic efficiency throughout the measurement. The good rate capability of

the anodes can be attributed to the improved electronic conductivity resulting from a high amount of carbon in the case of SiO_2/C-su80 and a dense carbon coating with high conductivity for SiO_2/C-st80-8h. Due to the higher conductivity, the current is evenly distributed around the amorphous silica outer shell of the diatom precursor, effectively shortening lithium diffusion pathways and enhancing the kinetics of electron transfer [39]. The high surface area and porosity of the diatom precursor provides efficient ionic transportation paths, facilitating the diffusion of Li^+ between the electrolyte and the SiO_2 active material, as well as room for the Si phase to expand during lithiation.

When examining the first-cycle discharge and charge capacities in Table 4.5 for the SiO_2/C-su80 and SiO_2/C-st80-8h anodes, it was noted that both the discharge and charge capacity of the SiO_2/C-su80 anode decreased significantly compared to the charge-discharge measurement at 100mA g^{-1}, while the discharge capacity increased for SiO_2/C-st80-8h and charge capacity remained the same. This large variability in reversible capacity was taken to be a consequence of inhomogeneous carbon distribution in the SiO_2/C-su80 composite, as the slurry obtained when mixing sucrose, water and the organics-free diatom precursor was very viscous, and may not have fully covered all the pores before solidifying prior to the heat-treatment. In contrast, the cornstarch, ethanol and organics-free diatom slurry dried slowly to yield a uniform white powder, showing good batch-to-batch and cell-to-cell reproducibility.

5.2.2 Cathode half cells

The galvanostatic charge-discharge curves of the commercial cathode materials are all similar to those reported in literature [17].

Of all the tested cathodes, LMO showed the closest proximity to the theoretical specific capacity in the galvanostatic charge-discharge test. The initial charge capacity actually exceeded the theoretical capacity of 148mA h g^{-1}, most likely due to irreversible side reactions with the electrolyte at high voltages and reorganization of the spinel structure [75]. The first-cycle Coulombic efficiency of the LMO half cell was 78.3%, giving an irreversible capacity loss of 21.7% and a reversible capacity of 116mA h g^{-1}. As expected, the characteristic capacity fade of LMO was observed, and the cathode retained 86.9% of the second-cycle capacity after 100 cycles. As discussed in Chapter 2.3.1.2, one of the primary mechanisms for this capacity loss is the dissolution of manganese ions in the presence of trace amounts of protons:

$$2Mn^{3+}(solid) \longrightarrow Mn^{4+}(solid) + Mn^{2+}(solution) \tag{5.1}$$

which is commonly mitigated by coating the surface with Al_2O_3, MgO, zirconica or other stable oxides to create a barrier between the spinel and the organic electrolyte [76]. Hence the small particle size (<0.5µm) and high specific surface area (14.9m^2 g^{-1}) of the recieved commercial LMO active material is likely to

lead to significant manganese dissolution. Further, the increased surface area will also lead to more extensive electrolyte decomposition, giving a larger initial irreversible capacity loss, as well as degrading the cycle life of the cathode, as was observed in Figure 4.9a [77].

The first cycle charge and discharge capacity for the NMC cathode at a current density of $50\text{mA}\,\text{g}^{-1}$ was 122 and $95\text{mA}\,\text{h}\,\text{g}^{-1}$, respectively. These values where lower than for LMO, and equate to 75% and 60% of the theoretical capacity for NMC. However, compared to LMO, Coulombic efficiency during cycling was improved, with an average value of 99.6% after the second cycle, as well as the capacity retention of more than 98% over 100 cycles of galvanostatic charge-discharge between 4.2 and 2.7V at $50\text{mA}\,\text{g}^{-1}$.

The initial and reversible capacities of the LFP/C cathodes were lower still compared to LMO and NMC. LFP/C-st25 showed the highest charge and discharge capacity of 95 and $61\text{mA}\,\text{h}\,\text{g}^{-1}$, resulting in a low initial Coulombic efficiency of 63.7%. The cycling performance of the LFP/C cathodes, as shown in Figure 4.10, showed a different behaviour than the LMO spinel and NMC transition metal oxide. Both charge and discharge capacities were found to undergo small increases and decreases from cycle to cycle, showing a lower Coulombic than LMO and NMC, but good capacity retention in the case of LFP/C-st25.

By comparing Figures 4.10a and 4.10b it is observed that LFP/C-st25 not only had a higher capacity, but also increased average Coulombic efficiency during cycling and better capacity retention. This is attributed to the increased amount of carbon coating, which improved the electronic conductivity of the active material and led to better utilization of the LFP particles.

However, the amount of carbon may not have been high enough to take full advantage of the theoretical capacity of LFP, which requires high electronic conductivity of the coating to offset the slow intrinsic lithium diffusion in both end-phases of LFP. The amount of carbon may also be too low be distributed homogeneously throughout the powder, and to give good contact between the active material, carbon black additive and the current collecter, which will give uneven utilization of the active material, and therefore large cell-to-cell variability. Further, the size of the commercial LFP particles ($<5\mu\text{m}$) is much larger than values reported in literature, which will increase lithium diffusion path length and further contribute to the poor reversible capacity. The presence of impurity phases is also detrimental to the performance of LFP cathodes, and although the impurity phases identified in the commercial LFP powder, lithiophosphate (Li_3PO_4), lithium phosphate ($Li_4P_2O_7$) and lithium iron pyrophosphate ($Li_{1.875}Fe(P_2O_7)$) are all known to be lithium permeable, but not able to store lithium [74]. This means that their presence will lower the specific capacity of the material.

Apart from LMO, the commercial cathodes exhibited significantly lower specific capacities compared to values reported in literature, *cf.* Table 2.3. However, a full optimization of the cathode materials was deemed beyond the scope of this work, and the cathode materials where employed as-recieved.

The rate performance of the commercial cathodes is summarized in Table 4.6.

The rate capability of LMO, shown in Figure 4.12a, was the worst of the commercial cathodes tested, retaining just 2.2% of the reversible capacity at a current density of 500mA g^{-1}. This was a surprising result given that LMO should possess intrinsically high electronic conductivity and therefore good rate capability due to the three-dimensional network of interconnected channels for lithium transport, and is frequently used as a cathode in high-power applications [4]. One possible explanation for the poor performance is the higher C-rate for LMO at a current density of 500mA g^{-1} compared to NMC, 5C vs. 3C, for LMO and NMC respectively, as the theoretical specific capacity is lower for LMO. This implies that a greater amount of the structure's availble lithium is removed in the same amount of time, which might have a greater impact on the rate performance than the absolute value of the current density used. When subjected to a current density of 200mA g^{-1}, corresponding to a rate of 2C, a capacity retention of 35.8% is seen, which is still worse than the other cathodes tested.

Of the cathodes, NMC showed the best rate performance as shown in Figure 4.12b, which was expected from the high intrinsic conductivity of the material, and two-dimensional lithium ion intercalation mechanism. An almost fully recoverable capacity retention of 63.3% at 500mA g^{-1} was observed, and high Coulombic efficiency was maintained throughout the 50 cycles.

The LFP/C cathodes also showed a good response to increased current density. Although the capacity retention at 500mA g^{-1} was not as good as for NMC, at 44.6 and 47% for LFP/C-st10 and LFP/C-st25, respectively, the capacity retention after 50 cycles was actually better in the case of LFP/C-st25. Again, the amount of carbon proved to be a distinguishing factor between LFP/C-st10 and LFP/C-st25, as LFP/C-st10 exhibited a smaller reversible capacity at the second cycle, at a current density of 500mA g^{-1}, and after the 50 cycles were completed.

5.2.3 Summary of half cell performance

Overall, the SiO_2/C anodes showed excellent galvanostatic cycling performance and rate capability, with moderately high capacities, good initial Coulombic efficiency and an increase in capacity during cycling. The growth in capacity can be attributed to growth of the Si-phase, and the high initial Coulombic efficiency is a result of formation of a stabilizing Li_2O, rather than Li_4SiO_4, inert matrix due to the shorter lithium diffusion pathways offered by the porous outer shell of the diatom precursor. The carbon coating succesfully increased the electronic conductivity of the anode, thereby enhancing alloying and dealloying kinetics, resulting in good cyclability and rate performance, as well as favouring the formation of Li_2O compared to Li_4SiO_4 which minimizes the first-cycle irreversible capacity loss. The carbon coating also has the added benefit of containing the volume changes during cycling, as well as protecting the SiO_2 of the diatoms from direct contact with the organic electrolyte, which leads to improved cycling

performance [39].

The commercial cathodes tested in this work all showed relatively low reversible capacities both during galvanostatic charge-discharge cycling at $50\text{mA}\,\text{g}^{-1}$, and during the rate capability measurement. Only the LMO and NMC cathodes had capacities within the range of practical values, *cf.* Table 2.3. The LFP/C-st10 and LFP/P-st25 showed the worst capacity, possibly due to the low amount of carbon present, large particle size and presence of impurity phases, but good cycling stability and capacity retention. The reversible capacity of the LMO cathode was close to the theoretical value, but the characteristic capacity fade partly due to manganese dissolution, led to poor long-term performance. Rate performance for the commercial cathodes was fair for NMC, LFP/C-st10 and LFP/C-st25, but the LMO showed negligible capacity retention at a high current density of $500\text{mA}\,\text{g}^{-1}$. The most well-rounded performance was exibited by NMC, with good reversible capacity and the best rate performance of the cathodes tested.

5.3 Full cell assemblies

5.3.1 Galvanostatic charge-discharge

To the best of the author's knowledge, no works have been published on the use of SiO_2 anodes in a full cell configuration. Therefore, cell voltage cut-off potentials used for full cells with silicon anodes were taken as a starting point for the electrochemical measurements, as both Si and SiO_2 are classified as alloy anodes, and share a similar chemistry during charge and discharge.

The intial cell voltage cut-off limits for the different cathodes are summarized in Table 3.5, which were later changed to the values in Table 3.6. Table 3.3 shows representative active material loadings.

After testing a full cell containing a fresh SiO_2/C-st80-8h anode in conjunction with a LFP/C-st10 cathode and observing an initial Coulombic efficiency of less than 15%, it was decided to investigate strategies to improve the reversible capacity of the battery.

5.3.1.1 Effect of formation cycling

The first attempt at improving the initial Coulombic efficiency was to use a slow first charge-discharge cycle at $10\text{mA}\,\text{g}^{-1}$. The initial charge capacity increased for LMO and NMC, due to the lower current density, but little change was observed for the LFP/C cathodes.

After the initial charge, only the NMC vs. SiO_2/C-st80-8h full cell showed any significant reversible capacity, as most of the lithium ions are intercalated at potentials above 3.5V vs. Li/Li^+.

5.3.1.2 Effect of prelithiation

Prelithiated SiO_2/C-st80-8h anodes were succesfully created by discharging and charging coin cells with a fresh SiO_2/C-st80-8h anode and a lithium counter electrode, and disassembling the cycled coin cells in an argon-filled glove box. The disassembly process was not detrimental to the performance of the prelithiated anode, as the full reversible capacity could be reobtained when cycled with a fresh lithium counter electrode. This result demonstrates that both the inert, stabilizing matrix and SEI can be formed and preserved prior to full cell assembly, effectively maximizing the initial Coulombic efficiency of the anode.

The prelithiated anode had a much smaller effect on full cell performance than anticipated, as the initial Coulombic efficiency remained very low for all the full cells tested. The only improvement was observed for the NMC vs. SiO_2/C-st80-8h cell where the first specific discharge capacity increased from 35 to 55mA h g^{-1} as a direct consequence of prelithiating the anode.

5.3.1.3 Effect of prelithiation and formation cycling

The combined approach of prelithiating the anode and using a slow formation cycle had little impact on the cycling performance of the LMO vs. SiO_2/C-st80-8h full cell. Both initial specific charge capacity, specific discharge capacity, Coulombic efficiency and capacity retention remained virtually unchanged compared to the prelithiation-only approach.

On the other hand, the NMC vs. SiO_2/C-st80-8h full cell showed a significantly improved capacity retention after being subjected to a slow initial cycle. Compared to the prelithiation-only approach, the capacity retention improved from 65% with respect to the second-cycle discharge capacity, to 85.4% after an initial formation cycle. Almost all of the irreversible capacity loss occurred in the first 10 cycles; the capacity retention with respect to the tenth cycle was 94.6%. Coulombic efficiency of the full cell was also very good, on average above 99.2% over 200 cycles.

By comparing Figures 4.16a and 4.16b it is observed that both the LMO- and NMC-containing full cells lose a large amount the cyclable lithium in the first 10 cycles. This behaviour is not observed in the half-cell assemblies for LMO or NMC, but the same response is noticed for all of the SiO_2/C anodes, as discussed in Chapter 5.2.1. This result indicates that the irreversible loss of the full cell is due to irreversible processes occuring at the anode, thereby lowering the anode specific capacity, and thus the actual capacity ratio between the anode and the cathode. It is quite possible that the NMC vs. SiO_2/C-st80-8h full cell became anode limited after the first ten cycles, as a close inspection of Figure 4.16b reveals a very slight increase in reversible capacity from the 80th cycle and outwards. An overweight in cathode capacity is undesirable due to the risk of the anode potential dropping below 0V vs. Li/Li^+ when the cell is charged, causing lithium plating on the anode.

The LFP/C cathodes also performed better after a slow initial formation cycle. Note that this is the first instance where the LFP/C-st10 cathode showed a higher initial charge and discharge capacity than LFP/C-st25, demonstrating significant cell-to-cell variability. But, as for the half cell galvanostatic charge-discharge measurement, improved capacity retention was noted for the LFP/C-st25 cathode. Coulombic efficiency during cycling was also higher for LFP/C-st25 at 99.5% vs. 98.6% for LFP/C-st10.

When the long-term cycling performance of the LFP/C vs. SiO_2/C-st80-8h full cells is compared with LMO or NMC vs. SiO_2/C-st80-8h full cells it is noted that the irreversible capacity loss during the first 10 cycles is significantly diminished. The most obvious difference between the two sets of full cells apart from the battery chemistry, is the higher anode capacity overweights, *cf.* Table 3.3. This in turn implies that the SiO_2/C-st80-8h active material is lithiated and delithiated to a lesser degree in the LFP/C-containing full cells compared to LMO and NMC-containing full cells. A smaller working potential range minimizes the risk of irreversible phenomena originating from volume change of the particles, but leads to poor utilization of both the active materials.

5.3.1.4 Effect of decreasing lower cell voltage cut-off potential

After examining the charge-discharge curves for the full cell with prelithiated anodes, Figures 4.15a, 4.15b, 4.17a and 4.17b, it was decided to reinvestigate the cell voltage cut-off limits, as the discharge potential dropped quickly, stopping the discharge reaction at very low capacities. This indicated that the capacity of the active materials was underutilized.

Figures 5.1 and 5.2 show the superimposed charge-discharge curves for the commercial cathodes and the SiO_2/C-st80-8h, corrected for the difference in anode-to-cathode capacity ratio. The charge curve for the full cell is obtained by subtracting the discharge curve for the SiO_2/C-st80-8h from the cathode charge curve. Correspondingly, the discharge curve can be found by subtracting the anode charge curve from the discharge curve of the cathode. The upper cell voltage limit remained the same, but the discharge voltage cut-off potential was adjusted to give maximal utilization of the cathode. The lower cell voltage cutoff was set to 1.2V for LMO, 1V for NMC and 0.5V for LFP. Further, it was decided to increase the current density from 50 to 100mA g^{-1} to expedite the testing and further highlight any cycling stabiliy issues.

By comparing the superimposed charge-discharge curves in Figures 5.1 and 5.2 to the obtained charge-discharge curves for the full cells in Figures 4.18, 4.19a and 4.19b, good agreement is observed. Charging commences at cell voltages between 1.5-2V, and the overall sloping shape of the full cell charge curve is the result of the difference between the flat cathode charge curve and the sloping anode discharge curve. The shape of the discharge curves for the full cell is obtained in the same fashion, and the observed change in slope for the LMO and NMC-containing full cells corresponds well with the change in slope for the SiO_2/C-st80-8h half cell.

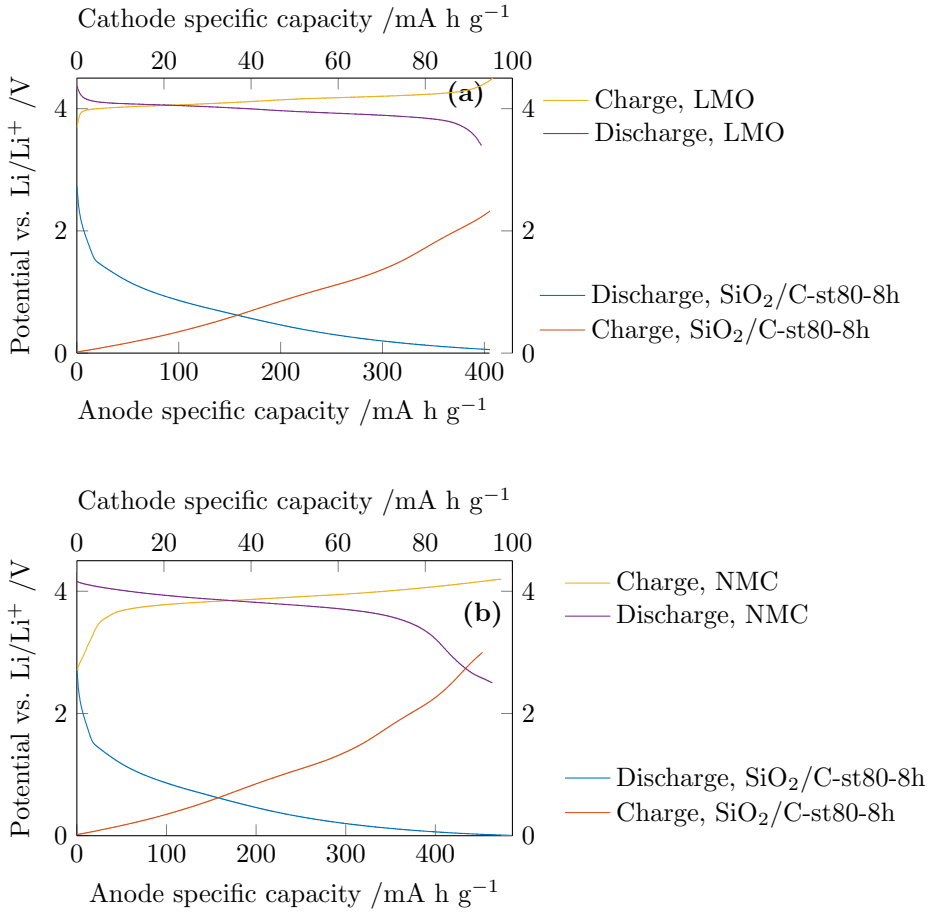

Figure 5.1: Superimposed half-cell charge-discharge curves for **(a)** LMO (20% anode excess capacity), **(b)** NMC (capacity balanced) cathode against the half-cell charge-discharge curve for the SiO_2/C-st80-8h anode.

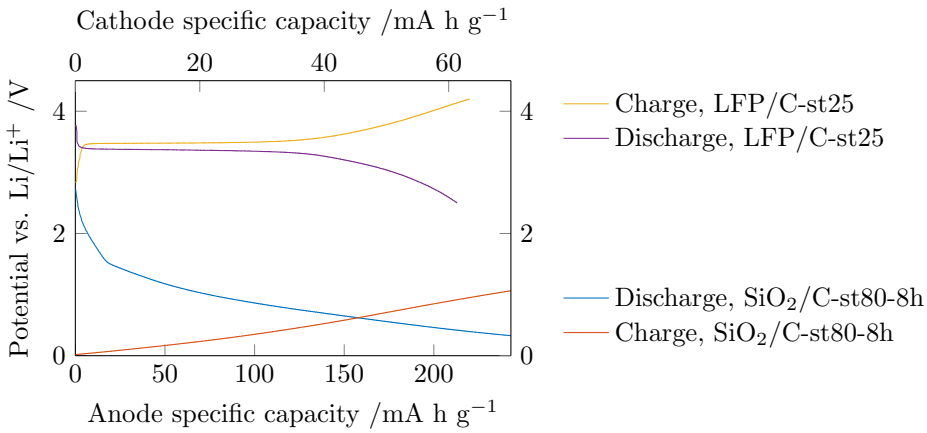

Figure 5.2: Superimposed half-cell charge-discharge curves for LFP-st25 (100% anode excess capacity) cathode against the half-cell charge-discharge curve for the SiO_2/C-st80-8h anode.

In the LFP/C vs. SiO_2/C-st80-8h full cells, the change in slope is attributed to the discharge curve of the LFP/C cathode.

As expected, the initial discharge capacity, and therefore initial Coulombic efficiency, improved greatly for all the full cells, as summarized in Table 4.8. In fact, the initial Coulombic efficiencies were higher for the full cells with a prelithiated anode, than the values obtained with a lithium metal counter electrode in the half cell measurements. Although the values are not directly comparable as a lower current density was used for the full cells, succesful improvement of the first-cycle Coulombic efficiency was demonstrated. The reversible capacity at the tenth cycle was also higher compared to the previous measurements.

Again, the LMO vs. SiO_2/C-st80-8h full cell showed the highest reversible capacity, as well as the highest maximal and average cell voltage. However, capacity fading was even more pronounced at 100mA g^{-1}, and only 48% of the second-cycle capacity was retained after 200 cycles.

Compared to LMO, the maximal and average discharge voltage, as well as reversible capacity, of the NMC vs. SiO_2/C-st80-8h full cell was somewhat lower. However, capacity retention was improved, at almost 60% after 200 cycles.

Further, the LFP/C cathodes showed the best capacity retention of the cathodes, but the smallest reversible capacity and lowest operating potential. The LFP/C-st25 vs. SiO_2/C-st80-8h showed the highest reversible capacity of the LFP/C-containing cells, as well as the best capacity retention, despite the low Coulombic efficiency.

Although the reversible capacity full cells increased significantly after decreas-

ing the lower cell voltage cut-off limit, as a result of fuller utilization of the active materials, the same development in reversible capacity was observed as for the cells cycled with the original voltage limits. A large portion of the irreversible capacity loss occured during the first 10-20 cycles for the LMO and NMC vs. SiO_2/C-st80-8h full cells, and the trend was more pronounced as an effect of the higher current density and deeper discharge compared to the previous measurement. Again, this development was not observed for the LFP/C vs. SiO_2/C-st80-8h full cells, which showed a slow, gradual decrease in reversible capacity over the 200 cycles.

Again, the LMO and NMC-containing full cells had smaller anode excess capacity compared to the LFP/C-containing full cells. By comparing Figures 5.1b, 5.1a and 5.2 it is observed that during discharge of the full cell, the charge potential for the anode increases to higher values for the LMO and NMC vs.SiO_2/C-st80-8h full cell as a consequence of the lower anode-to-cathode capacity ratio. This means that the anode is working in a wider potential range in the LMO and NMC vs.SiO_2/C-st80-8h full cells, and the SiO_2/C-st80-8h active material is lithiated and delithiated to a larger extent, compared to the LFP/C vs. SiO_2/C-st80-8h full cells, where the discharge potential of the anode is limited to 1.5-2V at the end of discharge, compared to 2.5-3V for LMO and NMC vs. SiO_2/C-st80-8h. Consequently, the stress placed on the anode active material due to the volume change of the Si phase will be larger for the LMO and NMC vs. SiO_2/C-st80-8h full cells as a result of the lower anode loading. As the stress placed on the anode is comparatively higher, degradation due to active particle pulverization, morphology changes and continuous SEI formation will be more pronounced, leading to the observed capacity fading.

5.3.2 Rate capability

The rate performance of the full cells at the reduced lower cell voltage cut-off was also evaluated, and the results summarized in Table 4.10.

A dramatic improvement in the rate capability was observed for the LMO vs. SiO_2/C-st80-8h full cell. Whereas the LMO vs. Li half cell showed negligible capacity at a current density of $500\text{mA}\,\text{g}^{-1}$, the full cell showed an impressive capacity retention of 54.5% at the same current density, while maintaining high Coulombic efficiency throughout the measurement. After 50 cycles, the capacity retention compared to the second cycle was 66.9%.

Comparatively, the NMC vs. SiO_2/C-st80-8h full cell showed slightly better rate performance, retainging over 61% of the second-cycle capacity at $500\text{mA}\,\text{g}^{-1}$, and 73.4% at the end of 50 cycles. Slightly better Coulombic effiency was also observed.

The smallest reversible capacity at $500\text{mA}\,\text{g}^{-1}$, but best capacity retention after 50 cycles, was shown by the LFP/C-st25 vs. SiO_2/C-st80-8h full cell, which also had the highest average Coulombic effiency of full cells at elevated current densities.

Both the LMO and LFP/C-st80-8h vs. SiO_2/C-st80-8h full cells showed better rate performance and higher capacity retention at 500mA g^{-1} compared to their half-cell counterparts, while a 2.2% reduction in reversible capacity at 500mA g^{-1} was observed for the NMC vs. SiO_2/C-st80-8h full cell. This result further demonstrates the good rate capability of the SiO_2/C-st80-8h anode material, as previously discussed.

However, capacity fading was still pronounced for the LMO and NMC vs. SiO_2/C-st80-8h full cells. Compared to the capacity after 50 cycles at a constant current density of 100mA g^{-1}, all the full cells subjected to the rate performance testing had retained less of their second-cycle capacity. This result indicates that capacity loss is accelerated by exposure to elevated current densities.

5.3.3 Energy density

The specific energy density of the as-fabricated full cells was calculated according to Equation 2.10, using the average discharge voltage, the average specific capacity of the commercial cathodes and the SiO_2/C-st80-8h anode, as measured in the fabricated full cell configuration. The LMO vs. SiO_2/C-st80-8h full cell showed the highest energy density due to the highest average capacity and voltage of the cathode material. Further, the full cell with a NMC cathode and SiO_2/C-st80-8h anode exhibited a slightly lower energy density, as a result of the lower capacity and average discharge voltage. Lower energy density still was observed for the LFP/C vs. SiO_2/C-st80-8h, mainly due to the poor capacity of the cathode active material and comparatively low cell voltage.

The energy density of the full cell assemblies fabricated in this work was significantly smaller than for commercial cells with graphite anodes and optimized, industry-standard cathodes, as evident from Figure 5.3. This result is a direct consequence of both the lower capacity obtained for the cathodes, but also the lower operating voltage of the full cells based on SiO_2/C-st80-8h anodes. The increase in anode capacity alone was not able to offset both of these loss contributions to achieve a similar energy density to commercial graphite-based full cells.

However, even with the poor cathode capacities obtained in the full cell assemblies with SiO_2/C-st80-8h anodes, an energy density higher than commercial cells based on LTO was achieved for the LMO vs. SiO_2/C-st80-8h, and a similar energy density was achieved for the NMC vs. SiO_2/C-st80-8h. This indicates that full cells based on SiO_2/C-st80-8h can fill an interesting middle ground between the low-energy LTO chemistries and high-energy graphite full cells, especially if cycle stability and rate performance can be improved further, and a cost reduction compared to graphite and LTO can be achieved.

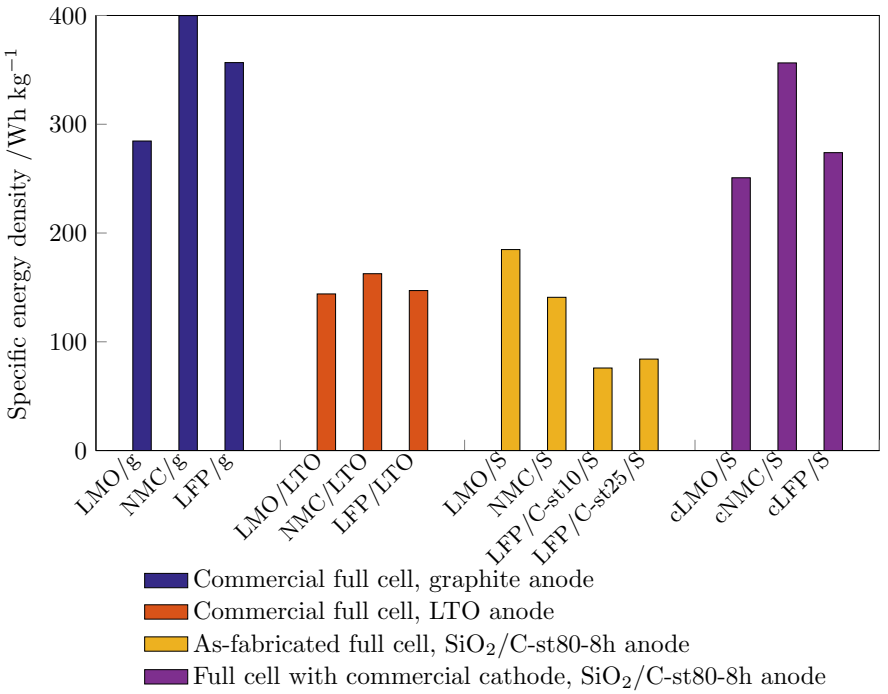

Figure 5.3: Specific energy density calculated for commercial full cells with a graphite anode, a LTO anode, the as-fabricated full cells with a SiO_2/C-st80-8h anode, and full cells with commercial cathodes and a SiO_2/C-st80-8h anode. g, S, and c denotes graphite, SiO_2/C-st80-8h and commercial, respectively.

5.3.4 Summary of full cell performance

Full cells consisting of SiO_2/C-st80-8h anodes and the commercial cathodes were succesfully constructed, indicating that SiO_2/C can be used as a viable anode material in full-cell lithium ion batteries.

The poor initial Coulombic efficiency for full cells with fresh SiO_2/C-st80-8h anodes could be succesfully reduced by prelithiating the anodes prior to full cell assembly and discharging to low cell voltages. The prelitiation process was found to have no detrimental effect on anode performance, thereby maximizing the initial Coulombic efficiency of the anode, while the deep discharge provided full utilization of the cathode material's capacity. The highest reversible capacity was obtained for the LMO vs. SiO_2/C-st80-8h full cell, closely followed by NMC vs. SiO_2/C-st80-8h. However, it was found that due to the small anode excess capacity in the LMO and NMC-containing full cells, the anode was working in a very wide potential range, leading to degradation of the SiO_2/C-st80-8h material and rapid capacity fade of the full cell. Comparatively, the LFP/C vs. SiO_2/C-st80-8h full cells showed better cycling stability due to a higher anode-to-cathode capacity ratio, but as expected from the half-cell measurments, smaller reversible capacity.

The rate performance of the full cells was found to be better or similar than for the corresponding half cells, further highlighting the good rate capability of the SiO_2/C-st80-8h anode. However, the capacity fade for LMO and NMC vs. SiO_2/C-st80-8h was even more pronounced at elevated current density.

Despite the poor performance of the cathode materials used, an energy density higher than for full cells containing LTO anodes was achieved for the LMO vs. SiO_2/C-st80-8h full cell. This result indicates that SiO_2/C-st80-8h-based battery chemistries can fill an intersting niche between low-energy LTO and high-energy graphite full cells.

5.4 SiO_2/C-based lithium ion batteries for energy storage

This section will evaluate the feasibility of using SiO_2/C-based lithium ion batteries as a possible energy storage system for the WIN WIN concept. First, the requirements of both use cases will be re-examined, before a discussion on possible system designs and a brief assessment of the cost will be provided.

5.4.1 Requirements, revisited

The requirements for two different use cases were briefly mentioned in Chapter 2.1.3 and summarized in Table 2.2, which is reproduced below for clarity.

Immediately, it is apparent that the two use cases will require different types of cells. For the first use case, a power cell geometry with thin electrodes, small

Table 5.1: Requirements for a potential energy storage system for the WIN WIN system. Case 1 - synchronous generator replaced by batteries. Case 2 - a larger energy storage system.

Condition	Case 1	Case 2
Operational lifetime	20 years	20 years
Production stops per annum	180	180
Average duration of stops	-	8 hours
Cycle life	3600 cycles	3600 cycles
Nominal power	20MW	20MW
Nominal capacity	0.5MWh	20MWh

cell and module size will be necessary, in order to dissipate the heat generated at very high current densities. External cooling may even be required, as high temperature is known to be detrimental to the cycle life of lithium ion batteries [78]. However, this will lower the energy density of the resulting system, thereby increasing the space and weight requirement. For the second use case, a cell optimized for energy density will be investigated.

It is also clear that the long cycle life of 3600 cycles will require that both the anode and the cathode show negligible capacity fading from cycle to cycle, as lithium ion batteries are generally considered dead after the reversible capacity drops below 80% of the initial reversible capacity. A full cell chemistry known to exhibit this cycle lifes and provide high power with excellent capacity retention is nanosized LFP particles vs. LTO. The cycling stability of this system is attributed to the lack of SEI formation and zero-strain intercalation in LTO, and minimal change in lattice parameters and accompanying volume change during the phase transition between $LiFePO_4$ and $FePO_4$, and improved lithium diffusion and heat dissipation as an effect of the small particle size [78]. Further, of the 172 lithium ion battery energy storage projects listed in the US Department of Energy's database, 42 are based on the LFP chemistry, reflecting the sector's confidence in the cycling stability and safety of this material [79]. However, the LTO vs. LFP system has a very low energy density as evident from Figure 5.3. By substituting LTO anode for a high-capacity anode with stable cycling characteristics and high stability, such as SiO_2/C-st80-8h, a higher energy density can be achieved, which is important for a system such as WIN WIN where space and load-carrying ability is limited.

For these reasons, the LFP vs. SiO_2/C-st80-8h chemistry will be considered as a potential candidate in the following discussion. In order to give a more accurate representation of the performance of a commercial SiO_2-based full cell, the specific capacity of the LFP cathode will be set to $160\,\mathrm{mA\,h\,g^{-1}}$, and good cycling stability of the cathode will be assumed. However, whether the cycle stability of the SiO_2/C-st80-8h is comparable to that of LTO has yet to be verified, but for the purposes of the following discussion, this assumption will be made.

5.4.2 Possible system design

Table 5.2 summarizes the most important metrics of the commercial LFP cathode vs. SiO_2/C-st80-8h energy storage system. It is important to emphasize that the following numbers are only preliminary estimates, and not optimized values from a performance or cost perspective.

The theoretical energy density of the commercial LFP vs. SiO_2/C-st80-8h cells was calculated based on the specific capacities obtained for the SiO_2/C-st80-8h anode at a current density of $50\text{mA}\,\text{g}^{-1}$, while the calculation for theoretical power density was based on a current density of $200\text{mA}\,\text{g}^{-1}$, and correspondingly diminished capacity, as determined in the rate capability measurement for the full cells. Both the theoretical energy density and theoretical power density was scaled with a full cell reduction factor of 0.48 to account for inactive cell materials, such as separators, current collectors and packaging [80][60]. This reduction factor is based on the use of 18650 battery cells (18mm in diameter, 65mm in length), which are widely available from a range of manufacturers, and used by Tesla in their Model S [81]. Advantages of the 18650 geometry is high packaging efficiency, structural integrity, easy thermal management due the small cell size, increased safety due to the high amount of individual cells and a large number of available manufacturers, which keeps investment costs down.

In order to estimate the obtainable volumetric energy density of the SiO_2/C-st80-8h vs. LFP full cells, the theoretical gravimetric energy density of commercial LFP vs. graphite cells, and commercial LFP vs. SiO_2/C-st80-8h in Figure 5.3 was compared. It was observed that the graphite chemistry had a 30% higher gravimetric energy density. The volumetric energy density of the LFP vs. SiO_2/C-st80-8h system was assumed to scale in a similar fashion, resulting in a reduction factor of 77%. Current commercial volumetric energy densities are $331\text{W}\,\text{h}\,\text{L}^{-1}$ for energy cells and $203\text{W}\,\text{h}\,\text{L}^{-1}$ for power cells [82].

The most important criterion for dimensioning the system was the required nominal power. Hence, in Case 1 where the synchronous generator was replaced with power cells, the required system size in terms of volume, weight and number of cells was drastically smaller compared to Case 2, where high-energy cells with lower power density was used to achieve the same nominal power. The system size for Case 1 was estimated to 47 850kg and 28m^3, which would fit in a standard 20-foot shipping container (39m^3) with room to spare for liquid cooling and battery management systems. Comparatively, in Case 2, a significantly higher amount of cells would be required in order to meet the power demand of the WIN WIN concept. Consequently, both the size, weight and number of cells in the resulting energy storage system will be too large to store on the 17 x 17m^2 platform. A solution where the storage system replaces some of the ballast in the floating structure can be envisaged, if the performance and safety of the battery bank over it's entire lifetime can be guaranteed, and the installation would not complicate the overall assembly of the full WIN WIN system.

The required nominal capacity of both systems was secondary to the power

requirement, and the actual nominal capacity was determined by the cells' power to energy ratio. For Case 1, the nominal capacity was found to be 4MW h, which can easily cover the energy demand of all critical systems (*cf.* Table 2.1), as well as powering the injection pumps at the target rate of 44000bbl d^{-1} (2.4MW) for 1.5 hours. Overall, this would result in an increase in average daily injection volume of approximately 900bbl d^{-1}, assuming 180 production stops due to wind variability per annum. For Case 2, the nominal capacity of 40MW h is enough to operate the injection pumps at the target injection rate for more than 16 hours. Assuming that the number of zero production hours could be reduced to 25% of the current value, an increase in daily injection volume of 5300bbl d^{-1} can be achieved.

Table 5.2: The specific capacities of the active materials, full cell reduction factor, gravimetric energy and power density of the full cell, volumetric capacity and smallest possible weight and volume of a battery system based on SiO_2/C-st80-8h vs. commercial LFP.

	Case 1	Case 2
Specific capacity, anode [$mA\,h\,g^{-1}$]	330	470
Specific capacity, cathode [$mA\,h\,g^{-1}$]	112	160
Full cell reduction factor, 18650 cells	0.48	0.48
Gravimetric energy density, system [$W\,h\,kg^{-1}$]	84	131
Gravimetric power density, system [$W\,kg^{-1}$]	418 (at 200$mA\,g^{-1}$)	65 (at 50$mA\,g^{-1}$)
Volumetric energy density [$W\,h\,L^{-1}$]	142	156
Smallest possible weight [kg]	47 850	15 2670
Smallest possible volume [m^3]	28	258
Nominal power [MW]	20	20
Nominal capacity [MW h]	4	40
Power-to-energy ratio	5	0.5
Number of 18650 cells [$m_{cell} = 40g$]	1.2 million	7.7 million

5.4.3 Cost assessment

The calculations so far have been based on the succesful use of the commercially available 18650 cell design, the cost of which several studies have investigated [8][80]. The cost of a single 18650 cell can be broken down according to the values provided in Table 5.3 [80].

There are several elements to consider when estimating the cost of a finished cell. Material costs will constitute the largest part of the total cost of the battery, the cathode material especially is an important driver. Since the analysis so far has considered commercial LFP cathodes, no reduction in cathode material cost will be assumed. Further, the cost of commercial battery-grade graphite material is estimated at 22.39EUR kg^{-1} at an industrial scale [8]. No pricing information was provided by Planktonic AS, so for the purposes of the following discussion, it is assumed that a 20% price reduction can be achieved by substituting graphite for aqueously fabricated SiO_2/C-st80-8h. This value is a cautious estimate, as Wood *et al.* has proposed that the prosessing cost of lithium ion batteries can be reduced by 90% by using aqueous processing of the electrodes, and thereby eliminating the use of expensive and toxic NMP and PVDF [8].

Based on these values, an estimate of the price of SiO_2/C-st80-8h vs. commercial LFP 18650 full cells was calculated, summarized in Table 5.3. Reduced processing cost was included as a reduction of anode cost, overhead and labour. Under these assumptions, a total reduction in cell costs of 10% from 1.83EUR per cell to 1.65EUR per cell can be achieved. Further cost compression is possible by using aqueous fabrication of the cathode as well, and doubling the loading of active material, which will halve the separator and packaging cost.

The final cost per kW h for a SiO_2/C-st80-8h vs. commercial LFP full cell will be lower compared to LTO vs. LFP systems due to the higher energy density, and lower cost of SiO_2/C-st80-8h compared to LTO [78]. However, as the energy density is lower for a SiO_2/C-st80-8h vs. commercial LFP full cell compared to a graphite vs. LFP full cell, the cost per kW h will be somewhat higher. But, this cost can be offset by the potentially longer cycle life, to give a lower cost per cycle compared to a graphite based full cell.

Table 5.3: Cost breakdown for a single 18650 cell in EUR, for a commercial graphite vs. LFP cell, and a SiO_2/C-st80-8h vs. commercial LFP cell [8][80].

Component	Cost, graphite vs. LFP [EUR]	Cost reduction factor	Cost, SiO_2/C-st80-8h vs. commercial LFP
Anode material	0.27	0.8	0.21
Cathode material	0.70	1	0.70
Separator	0.16	1	0.16
Electrolyte	0.34	1	0.34
Overhead	0.17	0.8	0.14
Labour	0.20	0.5	0.1
Total	1.83	0.9	1.65

5.4.4 Summary

Overall, the energy and power density achievable for a full cell consisting of a SiO_2/C-st80-8h anode and a commercial LFP cathode can satisfy the capacity and power requirements of the WIN WIN concept in both use cases. By using power cells to replace the synchronous generator and flywheel, a compact system can be constructed, that also has enough nominal capacity to power the injection pumps at the target rate for 1.5 hours, increasing the average injection rate with 900bbl d^{-1}. Expanding the capacity of the battery bank further will require cells optimized for energy density, which results in increased overall size and weight of the battery bank, which can be challenging to integrate with the WIN WIN system. However, the larger nominal capacity could potentially result in an increased daily injection volume of 5300bbl d^{-1}.

The cost of the SiO_2/C-st80-8h vs. commercial LFP based full cells based on the 18650 cell geometry can potentially be decreased with 10% compared to commercial graphite vs. LFP cells. Lower cost per kW h can be achieved compared to LTO-based chemistries. Due to the lower energy density of the SiO_2/C-st80-8h vs. LFP chemistry compared to graphite vs. LFP, the cost per kW h for SiO_2/C-st80-8h-based systems may be higher than for graphite, but the potential for long cycle life will result in a lower cost per cycle.

In total, these results indicate that the SiO_2/C-st80-8h vs. commercial LFP is viable battery chemistry for the WIN WIN concept, possibly outperforming LTO-based cells in terms of energy density and cost, and graphite-based in terms of cycle life and cost per cycle.

6 Further work

Clearly, this work has barely scratched the surface when it comes to fabricating successful lithium ion batteries based on silica anodes.

First and foremost, very large performance gains can be made by simply optimizing the commercial cathode electrodes. LMO was the only cathode material that achieved values close to its theoretical maximum.

Second, achieving a high, stable reversible capacity for the full cells was found highly dependent on the voltage limits employed during cycling, and consequently the capacity balancing between the anode and cathode; the reversible capacity could be significantly increased by discharging to lower cell voltages. Although this led to better utilization of the cathode material, the SiO_2/C-st80-8h anode material was found to work in a too wide potential range if the anode-to-cathode capacity ratio was low. This led to poor capacity retention, possibly due to degradation of the anode material thought to originate from volume change of the Si phase created in the initial cycles. In order to overcome this, a high anode-to-cathode capacity could be investigated to limit the working potential of the anode to 1-1.5V vs. Li/Li^+. This will circumvent the issue of anode degradation from excessive volume change and thus improve cyclability of the full cell, as well as increasing the cell voltage of the assembled battery. However, this approach will neseccarily decrease the specific capacity of the SiO_2/C-st80-8h active material, as less lithium is stored per mass of active material, which might negate any gain in operating voltage. In any case, a three-electrode set-up containing the cathode under study, a prelithiated SiO_2/C-st80-8h anode and a lithium reference electrode should be used to determine the exact voltage limits for the particular anode-to-cathode capacity ratio. The advantage of this approach is that the potential of the electrodes vs. Li/Li^+ can be monitored individually, to ensure that both the anode and the cathode are working within their respective voltage ranges. The full cells with of optimized anode-to-cathode loading and cell voltage cut-off limits should be examined both for cycling stability at constant current density, as well as for rate performance at elevated current densities. Long term testing will be especially important to confirm the feasibility of using SiO_2/C-st80-8h in practical applications.

Third, this work only examined prelithiation of the anode material by galvanostatic charge-discharge of a SiO_2/C-st80-8h vs. Li half cell. As this method has a poor scalability potential due to requiring a large number of testing stations for prelithiation, strategies such as heat-treatment of the diatom precursor with lithium metal powder to pre-form the inert matrix should be explored [61]. Another method is to perform a partial lithiation by spontaneous discharge of the anode

in the presence of electrolyte and lithium metal, which has proven to be effective for silicon anodes, and possibly implementable on a roll-to-roll scale [63][60].

Finally, the thermal properties of silica anodes and sodium alginate binders is also a largely unexplored area. The impact of temperature on reversible capacity, rate capability, capacity retention and degradation should be assessed by cycling both full and half cells at different temperatures. Thermal properties are an especially important aspect to consider when choosing a battery chemistry for large-scale energy storage, where thermal management becomes increasingly challenging as a result of the increased size of the battery cells, modules and packs.

7 Conclusion

Although this work is far from complete, it can be regarded as a proof-of-concept that carbon-coated SiO_2 is a feasible anode material for lithium ion battery full cells, capable of improving the specific capacity of the anode from 370mA h g^{-1} for graphite, to 469mA h g^{-1} for the SiO_2/C-st80-8h active material, thereby improving the total capacity of the battery. The excellent performance of the SiO_2/C-st80-8h anode was attributed to the combined effect of improved electronic conductivity as a result of coating with carbon, and the high surface area and porous nature of the diatom precursor.

Further, the SiO_2/C-st80-8h was shown to be compatible with the three major types of commercially available cathode materials. High reversible capacity of the full cell could be achieved by prelithiating the SiO_2/C-st80-8h anode and using a reduced lower cell voltage cut-off limit. Although the deep discharge improved the reversible capacity of the full cells, it was found that if the anode-to-cathode capacity ratio was too low, significant capacity fading resulted, possibly due to anode material degradation originating from the volume changes of the Si phase formed during the first discharge of the anode. Careful control of active material loadings and voltage limits will therefore be paramount for achieving good cycle life.

Based on the reversible capacity of the SiO_2/C-st80-8h anode material in the full cell measurements and an optimized commercial LFP cathode, a possible energy storage system was suggested for a wind-powered water injection concept. It was found that the commercial LFP vs. SiO_2/C-st80-8h system could provide the necessary nominal power and energy, and possibly outperforming LTO-based system in terms of both energy density and cost per kW h.

Bibliography

[1] Jean-Marie Tarascon and Michel Armand. 'Issues and challenges facing rechargeable lithium batteries'. In: 414.November (2001), pp. 359–367.

[2] Matthieu Metayer, Christian Breyer and Hans-Josef Fell. 'The projections for the future and quality in the past of the World Energy Outlook for solar PV and other renewable energy technologies'. In: ().

[3] Bruce Dunn, Haresh Kamath and Jean-Marie Tarascon. 'Electrical Energy Storage for the Grid: A Battery of Choices'. In: *Science* 334.6058 (2011), pp. 928–935.

[4] Dominic Bresser, Elie Paillard and Stefano Passerini. *Advances in Batteries for Medium and Large-Scale Energy Storage*. Elsevier, 2015, pp. 125–211.

[5] Michel Armand and Jean-Marie Tarascon. 'Building better batteries.' en. In: *Nature* 451.7179 (Feb. 2008), pp. 652–7.

[6] Vanchiappan Aravindan, Yun-Sung Lee and Srinivasan Madhavi. 'Research Progress on Negative Electrodes for Practical Li-Ion Batteries: Beyond Carbonaceous Anodes'. In: *Advanced Energy Materials* APRIL (2015).

[7] Anna Lisowska-Oleksiak, Andrzej P. Nowak and Beata Wicikowska. 'Aquatic biomass containing porous silica as an anode for lithium ion batteries'. In: *RSC Adv.* 4.X (2014), pp. 40439–40443.

[8] David L. Wood, Jianlin Li and Claus Daniel. 'Prospects for reducing the processing cost of lithium ion batteries'. In: *Journal of Power Sources* 275 (2015), pp. 234–242.

[9] Mingqi Li, Yan Yu, Jing Li, Baoling Chen, Xianwen Wu and P Chen. 'Nanosilica / carbon composite spheres as anodes in Li-ion batteries with excellent cycle stability †'. In: *Journal of Materials Chemistry A: Materials for energy and sustainability* 00 (2014), pp. 1–7.

[10] Are Kaspersen. 'WIN WIN Technical report'. In: *DNV GL* 1 (2016).

[11] Janina Molenda and Marcin Molenda. 'Composite Cathode Material for Li-Ion Batteries Based on LiFePO4 System'. en. In: (July 2011). Ed. by John Cuppoletti.

[12] Jeffrey W. Fergus. 'Recent developments in cathode materials for lithium ion batteries'. In: *Journal of Power Sources* 195.4 (2010), pp. 939–954.

[13] Yang Shao-Horn, Laurence Croguennec, Claude Delmas, Chris E. Nelson and Michael A. O'Keefe. 'Atomic resolution of lithium ions in LiCoO2.' In: *Nature materials* 2.7 (July 2003), pp. 464–7.

[14] Stanley M. Whittingham. 'Lithium batteries and cathode materials'. In: *Chemical Reviews* 104.10 (2004), pp. 4271–4301.

[15] Kazunori Ozawa. 'Lithium-ion rechargeable batteries with LiCoO2 and carbon electrodes: the LiCoO2/C system'. In: *Solid State Ionics* 69.3-4 (Aug. 1994), pp. 212–221.

[16] Hong Li, Zhaoxiang Wang, Liquan Chen and Xuejie Huang. 'Research on advanced materials for Li-ion batteries'. In: *Advanced Materials* 21.45 (2009), pp. 4593–4607.

[17] Marca M. Doeff. *Battery Cathodes*. 2013. arXiv: `UCD-ITS-RR-09-08`.

[18] Qiang Sun, Xin Hai Li, Zhi Xing Wang and Yong Ji. 'Synthesis and electrochemical performance of 5V spinel LiNi0.5Mn1.5O4 prepared by solid-state reaction'. In: *Transactions of Nonferrous Metals Society of China (English Edition)* 19.1 (2009), pp. 176–181.

[19] Akshaya K. Padhi, K.S. Nanjundaswamy and John B. Goodenough. 'Phospho-olivines as Positive-Electrode Materials for Rechargeable Lithium Batteries'. In: *J. Electrochem. Soc* 144.4 (1997).

[20] Li-Xia Yuan, Zhao-Hui Wang, Wu-Xing Zhang, Xian-Luo Hu, Ji-Tao Chen, Yun-Hui Huang and John B. Goodenough. 'Development and challenges of LiFePO ₄ cathode material for lithium-ion batteries'. In: *Energy Environ. Sci.* 4.2 (2011), pp. 269–284.

[21] K Xu. 'Electrolytes : Overview'. In: (), pp. 51–70.

[22] Pallavi Verma, Pascal Maire and Petr Novák. 'A review of the features and analyses of the solid electrolyte interphase in Li-ion batteries'. In: *Electrochimica Acta* 55.22 (Sept. 2010), pp. 6332–6341.

[23] Huiqiao Li and Haoshen Zhou. 'Enhancing the performances of Li-ion batteries by carbon-coating: present and future'. In: *Chemical Communications* 48.9 (2012), p. 1201.

[24] Christian Julien, Alain Mauger, Ashok Vijh and Karim Zaghib. *Lithium Batteries: Science and Technology*. Springer, 2015, p. 619.

[25] Masaki Yoshio, Satoshi Kugino and Nikolay Dimov. 'Electrochemical behaviors of silicon based anode material'. In: *Journal of Power Sources* 153.2 (Feb. 2006), pp. 375–379.

[26] Peter G Bruce, Bruno Scrosati and Jean-Marie Tarascon. 'Nanomaterials for rechargeable lithium batteries.' In: *Angewandte Chemie (International ed. in English)* 47.16 (2008), pp. 2930–2946.

[27] Vinodkumar Etacheri, Rotem Marom, Ran Elazari, Gregory Salitra and Doron Aurbach. 'Challenges in the development of advanced Li-ion batteries: a review'. In: *Energy & Environmental Science* 4.9 (2011), p. 3243.

[28] Uday Kasavajjula, Chunsheng Wang and John A. Appleby. 'Nano- and bulk-silicon-based insertion anodes for lithium-ion secondary cells'. In: *Journal of Power Sources* 163.2 (2007), pp. 1003–1039. ISSN: 03787753.

[29] Hui Wu and Yi Cui. 'Designing nanostructured Si anodes for high energy lithium ion batteries'. In: *Nano Today* 7.5 (2012), pp. 414–429.

[30] Nian Liu, Hui Wu, Matthew T. McDowell, Yan Yao, Chongmin Wang and Yi Cui. 'A yolk-shell design for stabilized and scalable Li-ion battery alloy anodes'. In: *Nano Letters* 12.6 (2012), pp. 3315–3321.

[31] Wei J. Zhang. 'A review of the electrochemical performance of alloy anodes for lithium-ion batteries'. In: *Journal of Power Sources* 196.1 (2011), pp. 13–24.

[32] Igor Kovalenko, Bogdan Zdyrko, Alexandre Magasinski, Benjamin Hertzberg, Zoran Milicev, Ruslan Burtovvy, Igor Luzinov and Gleb Yushin. 'A Major Constituent of Brown Algae for'. In: *Science* 334.October (2011), pp. 75–79.

[33] Shu-Lei Chou, Yuede Pan, Jia-Zhao Wang, Hua-Kun Liu and Shi-Xue Dou. 'Small things make a big difference: binder effects on the performance of Li and Na batteries.' en. In: *Physical chemistry chemical physics : PCCP* 16.38 (Oct. 2014), pp. 20347–59.

[34] Bo Gao, Saion Sinha, Les Fleming and Otto Zhou. 'Alloy formation in nanostructured silicon'. In: *Advanced Materials* 13.11 (2001), pp. 816–819.

[35] Lars-Henrik Nysteen. 'Nanostructured Silica as an Anode for Li-ion Batteries'. In: *NTNU* 1 (2015).

[36] Mahmut Dirican, Ozkan Yildiz, Yao Lu, Xiaomeng Fang, Han Jiang, Huseyin Kizil and Xiangwu Zhang. 'Flexible binder-free silicon/silica/carbon nanofiber composites as anode for lithium–ion batteries'. In: *Electrochimica Acta* 169 (2015), pp. 52–60.

[37] Xianhua Hou, Miao Zhang, Jiyun Wang, Shejun Hu, Xiang Liu and Zongping Shao. 'High yield and low-cost ball milling synthesis of nano-flake Si@SiO2 with small crystalline grains and abundant grain boundaries as a superior anode for Li-ion batteries'. In: *Journal of Alloys and Compounds* 639 (2015), pp. 27–35.

[38] Joong-yeon Kim, Dan Thien, Joon-sup Kang and Seung-wan Song. 'Facile synthesis and stable cycling ability of hollow submicron silicon oxide – carbon composite anode material for Li-ion battery'. In: *Journal of Alloys and Compounds* 633 (2015), pp. 92–96. ISSN: 0925-8388.

[39] Huan-Huan Li, Xing-Long Wu, Hai-Zhu Sun, Kang Wang, Chao-Ying Fan, Lin-Lin Zhang, Feng-Mei Yang and Jing-Ping Zhang. 'Dual-Porosity SiO\n 2\n /C Nanocomposite with Enhanced Lithium Storage Performance'. In: *The Journal of Physical Chemistry C* (2015), p. 150206121013000.

[40] Mingqi Li, Yan Yu, Jing Li, Baoling Chen, Aishuak Konarov and P Chen. 'Fabrication of graphene nanoplatelets-supported SiO x -disordered carbon composite and its application in lithium-ion batteries'. In: *Journal of Power Sources* 293 (2015), pp. 976–982.

[41] Jingke Meng, Yuan Cao, Yang Suo, Yushan Liu, Jianmin Zhang and Xiucheng Zheng. 'Facile Fabrication of 3D SiO2@Graphene Aerogel Composites as Anode Material for Lithium Ion Batteries'. In: *Electrochimica Acta* 176 (2015), pp. 1001–1009. ISSN: 00134686.

[42] Hui Wang, Ping Wu, Huimin Shi, Wangzhong Tang, Yawen Tang, Yiming Zhou, Peiliang She and Tianhong Lu. 'Hollow porous silicon oxide nanobelts for high-performance lithium storage'. In: *Journal of Power Sources* 274 (2015), pp. 951–956.

[43] Wenjun Wu, Jing Shi, Yunhui Liang, Fang Liu, Yi Peng and Huabin Yang. 'A low-cost and advanced SiO _x –C composite with hierarchical structure as an anode material for lithium-ion batteries'. In: *Phys. Chem. Chem. Phys.* 17.20 (2015), pp. 13451–13456.

[44] Xuan Wu, Zhi-qiang Shi, Cheng-yang Wang and Juan Jin. 'Nanostructured SiO2/C composites prepared via electrospinning and their electrochemical properties for lithium ion batteries'. In: *Journal of Electroanalytical Chemistry* 746 (2015), pp. 62–67.

[45] Zachary Favors, Wei Wang, Hamed Hosseini Bay, Aaron George, Mihrimah Ozkan and Cengiz S. Ozkan. 'Stable Cycling of SiO2 Nanotubes as High-Performance Anodes for Lithium-Ion Batteries'. In: *Scientific Reports* 4 (2014), pp. 1–7.

[46] Qianjun He, Chaohe Xu, Jianqiang Luo, Wei Wu and Jianlin Shi. 'A novel mesoporous carbon@silicon-silica nanostructure for high-performance Li-ion battery anodes.' In: *Chemical communications (Cambridge, England)* 50.90 (2014), pp. 13944–7.

[47] Anara Molkenova and Izumi Taniguchi. 'Preparation and characterization of SiO2/C nanocomposites by a combination of mechanochemical-assisted sol–gel and dry ball milling processes'. In: *Advanced Powder Technology* 26.2 (2014), pp. 1–8.

[48] Yurong Ren, Hengma Wei, Xiaobing Huang and Jianning Ding. 'A Facile Synthesis of SiO2@C@graphene Composites as Anode Material For Lithium Ion Batteries'. In: *International Journal of Electrochemical Science* 9 (2014), pp. 7784–7794.

[49] Jiguo Tu, Yan Yuan, Pan Zhan, Handong Jiao, Xindong Wang, Hongmin Zhu and Shuqiang Jiao. 'Straightforward Approach toward SiO 2 Nanospheres and Their Superior Lithium Storage Performance'. In: *The Journal of Physical Chemistry C* 118 (2014), pp. 7357–7362.

[50] Mingqi Li, Jing Li, Kai Li, Yan Zhao, Yongguang Zhang, Denise Gosselink and P. Chen. 'SiO2/Cu/polyacrylonitrile-C composite as anode material in lithium ion batteries'. In: *Journal of Power Sources* 240.3 (2013), pp. 659–666.

[51] Pengpeng Lv, Hailei Zhao, Jing Wang, Xin Liu, Tianhou Zhang and Qing Xia. 'Facile preparation and electrochemical properties of amorphous SiO2/C composite as anode material for lithium ion batteries'. In: *Journal of Power Sources* 237 (2013), pp. 291–294.

[52] Nan Yan, Fang Wang, Hao Zhong, Yan Li, Yu Wang, Lin Hu and Qianwang Chen. 'Hollow Porous SiO2 Nanocubes Towards High-performance Anodes for Lithium-ion Batteries'. In: *Scientific Reports* 3 (2013), pp. 1–6.

[53] Won-Seok Chang, Cheol-Min Park, Jae-Hun Kim, Young-Ugk Kim, Goojin Jeong and Hun-Joon Sohn. 'Quartz (SiO2): a new energy storage anode material for Li-ion batteries'. In: *Energy & Environmental Science* 5.5 (2012), p. 6895.

[54] Hua-Chao Tao, Mian Huang, Li-Zhen Fan and Xuanhui Qu. 'Interweaved Si@SiOx/C nanoporous spheres as anode materials for Li-ion batteries'. In: *Solid State Ionics* 220 (2012), pp. 1–6.

[55] Manickam Sasidharan, Dian Liu, Nanda Gunawardhana, Masaki Yoshio and Kenichi Nakashima. 'Synthesis, characterization and application for lithium-ion rechargeable batteries of hollow silica nanospheres'. In: *Journal of Materials Chemistry* 21 (2011), p. 13881.

[56] Yu Yao, Jingjing Zhang, Leigang Xue, Tao Huang and Aishui Yu. 'Carbon-coated SiO2 nanoparticles as anode material for lithium ion batteries'. In: *Journal of Power Sources* 196.23 (2011), pp. 10240–10243.

[57] Bingkun Guo, Jie Shu, Zhaoxiang Wang, Hong Yang, Lihong Shi, Yinong Liu and Liquan Chen. 'Electrochemical reduction of nano-SiO2 in hard carbon as anode material for lithium ion batteries'. In: *Electrochemistry Communications* 10.12 (2008), pp. 1876–1878. ISSN: 13882481.

[58] Qian Sun, Bing Zhang and Zheng Wen Fu. 'Lithium electrochemistry of SiO2 thin film electrode for lithium-ion batteries'. In: *Applied Surface Science* 254.13 (2008), pp. 3774–3779. ISSN: 01694332.

[59] Minseong Ko, Pilgun Oh, Sujong Chae, Woongrae Cho and Jaephil Cho. 'Considering Critical Factors of Li-rich Cathode and Si Anode Materials for Practical Li-ion Cell Applications'. In: *Small* 11.33 (2015), pp. 4058–4073.

[60] Hye Jin Kim, Sunghun Choi, Seung Jong Lee, Myung Won Seo, Jae Goo Lee, Erhan Deniz, Yong Ju Lee, Eun Kyung Kim and Jang Wook Choi. 'Controlled Prelithiation of Silicon Monoxide for High Performance Lithium-Ion Rechargeable Full Cells'. In: *Nano Letters* (2015), acs.nanolett.5b03776.

[61] Jee Ho Yom, Sun Woo Hwang, Sung Man Cho and Woo Young Yoon. 'Improvement of irreversible behavior of SiO anodes for lithium ion batteries by a solid state reaction at high temperature'. In: *Journal of Power Sources* 311 (2016), pp. 159–166.

[62] Pier Paolo Prosini, Cinzia Cento, Alessandro Rufoloni, Flaminia Rondino and Antonino Santoni. 'A lithium-ion battery based on LiFePO4 and silicon nanowires'. In: *Solid State Ionics* 269 (2015), pp. 93–97.

[63] Changju Chae, Hyung Joo Noh, Jung Kyoo Lee, Bruno Scrosati and Yang Kook Sun. 'A high-energy li-ion battery using a silicon-based anode and a nano-structured layered composite cathode'. In: *Advanced Functional Materials* 24.20 (2014), pp. 3036–3042.

[64] Krzysztof Kierzek and Jacek Machnikowski. 'Factors influencing cycle-life of full Li-ion cell built from Si/C composite as anode and conventional cathodic material'. In: *Electrochimica Acta* 192 (2016), pp. 475–481.

[65] Kwangsup Eom, Tapesh Joshi, Arnaud Bordes, Inhwan Do and Thomas F. Fuller. 'The design of a Li-ion full cell battery using a nano silicon and nano multi-layer graphene composite anode'. In: *Journal of Power Sources* 249 (2014), pp. 118–124.

[66] Isidor Buchman. *BU-502: Discharging at High and Low Temperatures – Battery University*. 2016.

[67] Hohsen Corporation. 'A Partial Cross Section of 2016 Coin cell'. In: ().

[68] Muhammad Hasanuzzaman and Fride Vullum-Bruer. 'Diatoms (SiO2) as an Environmentally Friendly Nano-Structured High-Performance Anodes for Lithium-ion Batteries'. In: *Norwegian University of Science and Technology* (2016).

[69] Nils Wagner, Ann-Mari Svensson and Fride Vullum-Bruer. 'Effect of carbon content and annealing atmosphere on phase purity and morphology of Li2MnSiO4 synthesized by a PVA assisted sol–gel method'. In: *Solid State Ionics* 276 (Aug. 2015), pp. 26–32.

[70] Nils Wagner, Ann Mari Svensson and Fride Vullum-Bruer. 'Flame-made Lithium Transition Metal Orthosilicates'. In: *Electrochimica Acta* 203 (2016), pp. 246–256.

[71] Christian M. Julien, Karim Zaghib, Alain Mauger, Michel Massot, Atmane Ait-Salah, Mohamed Selmane and Francois Gendron. 'Characterization of the carbon coating onto LiFePO4 particles used in lithium batteries'. In: *Journal of Applied Physics* 100.6 (2006).

[72] Jian Gao, Jianjun Li, Xiangming He, Changyin Jiang and Chunrong Wan. 'Synthesis and electrochemical characteristics of LiFePO4/C cathode materials from different precursors'. In: *International Journal of Electrochemical Science* 6.7 (2011), pp. 2818–2825.

[73] Haitao Zhou, Mari-Ann Einarsrud and Fride Vullum-Bruer. 'High capacity nanostructured $Li_2Fe_xSiO_4/C$ with Fe hyperstoichiometry for Li-ion batteries'. In: *Journal of Power Sources* (2012).

[74] Byoungwoo Kang and Gerbrand Ceder. 'Battery materials for ultrafast charging and discharging'. In: *Nature* 458.7235 (Mar. 2009), pp. 190–193.

[75] Jusef Hassoun, Ki-Soo Lee, Yang-Kook Sun and Bruno Scrosati. 'An advanced lithium ion battery based on high performance electrode materials.' In: *Journal of the American Chemical Society* 133.9 (Mar. 2011), pp. 3139–43.

[76] Christian M Julien, Alain Mauger, Karim Zaghib and Henri Groult. 'Comparative Issues of Cathode Materials for Li-Ion Batteries'. In: *Inorganics* 2 (2014), pp. 132–154.

[77] Jianlin Li, Claus Daniel and David Wood. 'Materials processing for lithium-ion batteries'. In: *Journal of Power Sources* 196.5 (2011), pp. 2452–2460. ISSN: 03787753.

[78] Terrence Xu, Wei Wang, Mikhail L. Gordin, Donghai Wang and Daiwon Choi. *Lithium-ion batteries for stationary energy storage*. 2010.

[79] Sandia National Laboratory. *DOE Global Energy Storage Database*. 2016.

[80] Linda Gaines and Roy Cuenca. 'Costs of Lithium-Ion Batteries for Vehicles'. In: *Energy* 48.3 (2000), p. 73.

[81] Thomas Fisher. *What Goes Into A Tesla Model S Battery–And What It May Cost*. 2013.

[82] Tyva Lithium. *18650 Li-ion Cells*. 2016.